Wetting Behaviour of Droplets and Capillary Liquid Bridges Involving Liquid Infused Surfaces

SARAH JANE GOODBAND

University of Durham

Wetting Behaviour of Droplets and Capillary Liquid Bridges Involving Liquid Infused Surfaces

Author:

Ms. Sarah Jane Goodband

Supervisors:

Prof. Kislon Voïtchovsky

Prof. Halim Kusumaatmaja

A thesis presented for the degree of

Doctor of Philosophy

Durham Centre for Soft Matter Physics

Department of Physics

Stockton Road

Durham

DH1 3LE

30th April 2022

Abstract

Liquid-infused surfaces (LIS), formed of a nano- or micro-structured porous material that is impregnated with a lubricating fluid, are biomimics of the pitcher plant. Their slippery surface makes them ideal candidates for a wide range of applications, from anti-corrosive, anti-fouling and anti-icing coatings to self-healing surfaces and controlled wetting. Here, LIS are studied to determine the fundamental interactions of the lubricant layer with the porous medium, and with droplets and capillary liquid bridges under different environmental conditions. When LIS are exposed to realistic environmental conditions, they rapidly lose their desirable slippery properties and age, which may compromise their original application. This may occur through a process of oil loss, smoothing of the porous layer and porous-substrate degradation. Oil loss is attributed to the formation of micro-emulsion in the lubricant layer which displaces oil away from the surface.

LIS interactions with stretching capillary liquid bridges (CLB) are also considered. Measuring capillary forces on LIS is challenging as they present a surface with little friction or pinning. A novel set-up is created to study the comparatively small forces exhibited by LIS, and extract the bridge geometry. CLBs on non-infused surfaces are strongly affected by contact line pinning, and hysteretic behaviours are commonly observed for the measured contact radii, contact angles, and capillary forces. In contrast, CLBs on LIS experience no pinning and hysteretic behaviours are largely absent. Furthermore, cloaking and the formation of oil ridges change the effective CLB surface tension and contact angle, and gravity has a more dominant effect due to small changes in capillary forces on LIS. In all cases, including for asymmetric bridges (with one LIS and one other surface), it is shown that the measured capillary forces can be well-described by a simple theoretical model that uses the CLB contact radius, contact angle and curvature as input parameters.

Declaration

The work presented in this thesis has been developed under the supervision of Prof. Kislon Voïtchovsky and Prof. Halim Kusumaatmaja of the Department of Physics at Durham University. All text and figures are the work of the author, unless otherwise stated. No part of this thesis has been presented for any other degree or qualification.

Statement of Copyright

Acknowledgements

Firstly, I would like to thank my supervisors, Kislon Voïtchovsky and Halim Kusumaatmaja who have been excellent mentors and teachers. I have really learned so much on this PhD journey thanks to their help and guidance. Secondly, sincere thanks to my twin sister Rachel: my fellow PhD, housemate and best friend. Thank you for your love and support over these years as we completed our PhDs together. I would also like to thanks all the wonderful friends I made in Durham, my labsmates in physics and chemistry, simulation buddies and the many other people I met through the physics social committee and eco-group. Finally, I would like to thank my parents who supported me to follow my dreams and achieve my full potential.

Contents

Chapter 1

Introduction

1.1 A Bit of History

Since the earliest times, different wetting phenomena have puzzled civilisations. Many of the questions related to seemingly inexplicable events that were observed in everyday situations. This might be something as simple as seeing oil spread on water and calming the ripples and waves or noticing the leaves of lotus repelling mud and water to remain perfectly clean. Today, wetting phenomena remain an active field of research with our relationship and history with the subject at the heart of many scientific reviews [1–3].

Early investigations by Franklin [4] in the 1700s described the spreading of oil over water on Clampham pond noting that *'when [oil is] put on water it spreads instantly many feet round, becoming so thin as to produce the prismatic colours, for a considerable space and beyond them so much thinner as to be invisible, except in its effect of smoothing waves at a much greater distance'*. This is probably one of the first thin film experiments recorded! The 1700s also saw experiments investigating capillary rise (where a liquid can seemingly rise in opposition to forces such as gravity to rise up into a tube or cloth) by scientists including Hauksbee and Jurin [2,5,6] who were able to quantify the final rise height in relation to the tube diameter. These early observations and experiments laid the foundation for further

work and experimentation to explain the unique relationships of liquids with other liquids and solids.

When Franklin described the oil spreading on Clapham pond or Hauksbee and Jurin thought about capillary rise sitting on surfaces, they stopped short of looking at both situations in terms of interfaces. The oil-water interface described by Franklin is a liquid-liquid interface (the meeting-point of two immiscible liquids)[7] while the capillary tube-water is a solid-liquid interface (the meeting-point of a solid and liquid)[8]. These two interfaces are found in everyday situations, from the tea we drink in the morning to the document we print at work. Understanding these two interfaces is key to understanding the many wetting phenomena they underpin.

The 1750s saw the introduction of the term 'surface tension' by Segner[3] to explain the membrane-like behaviour of the surface of liquid drops. This led Young[9] and Laplace, in the 1800s[10], to (almost simultaneously) develop equations that relate surface tension to the pressure across an interface (now the Young-Laplace Equation). This was used to answer questions relating to capillary rise in tubes and the shape of droplets or capillary liquid bridges. The Young equation[9] was also introduced to describe the balance of forces on a droplet at the triple point. With these mathematical descriptions of the forces and pressures acting on liquids, the field was able to expand, but still with many questions remaining.

One particularly understudied area was the pinning behaviours and the interactions of liquids with rough surfaces. Rayleigh and Pockels[11,12] are understood to be the first to report hysteresis in contact angles. Pockels reported the advancing and receding angles of different liquids on solids and noted that this should be explored further. Sulman[13] coined the phrase 'contact angle hysteresis (CAH)' which represented the difference between the advancing and receding contact angles. This definition is still in use today. Building on the work of Young and Laplace (1800s), Wenzel[14] (1930s) and later Cassie and Baxter[15](1940s-50s) began to look at roughened and non-homogeneous surfaces. Wenzle realised that with a roughened surface (more surface area exposed) the apparent contact angle of a droplet changes. For hydrophbic surfaces as the roughness increases, the contact

angle increases, whereas for hydrophilic surfaces, as the roughness increases, the contact angle decreases. Cassie and Baxter looked at the fractions of the droplet exposed to different surfaces (e.g. in structured surface this could be the pillars and air). This allowed for predictions about contact angles to be made about newly emerging superhydrophobic surfaces that were constructed of pillars and arrays by groups such as Dettre and Johnson in the 1960s. Many studies have followed up this work with more novel and unusual surface patterns.

These new superhydrophobic surfaces were part of a family of anti-fouling coatings and include superhydrophilic and liquid infused surfaces (LIS) [16]. These surfaces were designed to reduce the environmental impact of anti-fouling coatings by creating surfaces that prevent the adhering of detritus or organism fouling. These surfaces were designed in many different ways, with unique patterning and materials [17–21].

LIS, inspired by the nephthesis pitcher plant, exhibit low contact angle hysteresis and low roll off angles. These surfaces present two interfaces to study. The interactions between the solid substrate and the infusing liquid, and the infusing liquid and other test liquids. When experimenting with these systems, there are different configurations in which the infusing liquid can interact with the solid substrate and the test liquid, including cloaking the test liquid or creating oil ridges. This means that there are lots of opportunities to investigate new interfacial phenomena that have yet to get the attention they deserve, such as ageing of LIS or investigating capillary liquid bridges on LIS.

1.2 Goals of this Thesis

This thesis will investigate the behaviour of droplets and capillary liquid bridges on LIS. In particular it will address questions around: How do LIS age? What is the best way to measure capillary forces of liquid bridges on LIS? Can capillary forces on LIS be characterised using existing models? How is the pinning and CAH on LIS different to other surfaces of different wettability? By understanding how surfaces

age, they can be designed based on their intended application and be modified to mitigate for their potential limitations. This work builds on understanding pinning behaviours and contact angle hysteresis of rough surfaces and on the design of superhydrophobic surfaces.

Capillary forces on CLBs, which shall be discussed in detail later, are related to the surface tension, contact angles, the radius of the CLB and its curvature. These parameters and their measurement have been the subject of research since the 1700s. On LIS, where the surfaces are designed to be slippery, with low friction and contact angle hysteresis, the capillary forces measured are very small. This leads to difficulties in being able to measure them. Being able to measure forces would allow for the forces experienced by these surfaces to be compared between different designs, and also to determine the effect of a lubricant layer interacting with the capillary liquid bridge.

Comparing LIS with surfaces of different wettability allows for a comparison between a surface which is hydrophobic and non-pinning, to other surfaces that are hydrophilic, or hydrophobic and do pin. This allows us to compare the different behaviours and compare them to existing models. These models capture pinning, gravity and explain the changes in forces as liquid bridges are stretched between the surfaces of different wettability. This is important for understanding the forces experienced on LIS if they are one day be used as surface coatings.

1.3 Structure of this Thesis

Overall, this thesis investigates the behaviour of droplets and CLBs on LIS. It is structured into 7 main chapters. Chapter 1 introduces the key concepts in the field of wetting, the key equations required to model the experimental observations as well as the motivation for the work explored here. Chapter 2 looks at the fabrication of the test surfaces, including LIS and an overview of the techniques and equipment used.

The results are then separated into 4 main chapters. Chapter 3 determines the best fabrication method for the LIS, comparatively testing different fabrication strategies and characterising the resulting LIS in each case. The final method produces a uniform, stable LIS which is then used throughout this thesis.

Chapter 4 examines the robustness and reliability of LIS by exposing it to different types of ageing and wear. The aim is to explore how LIS age in realistic environmental conditions, and determine the ageing mechanisms by which the surface is damaged or loses oil.

Chapter 5 introduces a novel set-up designed to investigate capillary liquid bridges between LIS. The setup is designed to be inexpensive and to permit very low force measurements. This makes it flexible enough to measure forces on LIS which fills a gap in the literature where no other similar set-up is available with such a design.

Chapter 6 makes use of the setup designed in Chapter 5 to investigate the stretching of liquid bridges between LIS surfaces and compare them to standard hydrophobic and hydrophilic surfaces. It aims to deepen our knowledge on capillary liquid bridges and investigate the role of cloaking and gravity.

Chapter 7 brings all the results together in the context of current research in the field. It also proposes further work based on the conclusions of this thesis that will continue to advance our knowledge of LIS and capillary liquid bridges on LIS.

1.4 Wetting theory

1.4.1 Young Contact Angle

When a droplet of water is placed on a flat homogeneous surface it forms a particular angle with the substrate it is placed on. This contact angle depends on the surface tension between the droplet and the solid, the droplet and the surrounding gas and on the surface tension between the solid and the gas. This can be seen in Fig. 1.1. Mathematically the Young equation expresses these considerations for a

droplet on a flat, homogeneous surface[9]:

$$\sigma_{SG} = \sigma_{SL} + \sigma_{LG} \cos\theta_Y, \tag{1.1}$$

where σ_{SG}, σ_{SL} and σ_{LG} are the solid-gas, solid-liquid and liquid-gas interfacial energies and θ_Y is the contact angle (or Young contact angle). It should be noted that measuring the contact angle of static droplets is only one method of characterising droplet-surface interactions but further information can be gained from studying droplets sliding across surfaces as will be discussed in Chapter 1.4.2.

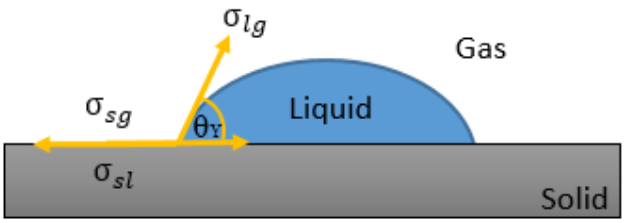

Figure 1.1: The contact angle of a liquid droplet on a solid, surrounded by the neighbouring gas phase, is shown with the associated interfacial energies (σ). σ_{SG}, σ_{SL} and σ_{LG} are the solid-gas, solid-liquid and liquid-gas interfacial energies and θ_Y is the contact angle.

1.4.2 Contact Angle Hysteresis

A droplet placed on a surface was considered by Young to have a single contact angle, however in reality this contact angle can vary (taking a range of values) depending on the 'stickiness'[22] of the surface. When a droplet moves across the surface one can measure the angle of the leading and trailing edge with respect to the substrate. These angles are known as the advancing θ_A and receding θ_R contact angles and the difference between them, θ_A - θ_R, is the contact angle hysteresis (CAH). Fig.1.2 shows the measurement of the advancing and receding contact angles on an inclined surface and using a sessile drop. In the case of the inclined plane, the front of the droplet is the advancing angle and the back of the droplet presents the receding angle. When using a sessile droplet, as liquid is pumped into

the droplet the angles presented are the advancing angles, while as liquid is removed, the receding angles are obtained. The origin of this hysteresis is attributed to 3 main sources: surface roughness, chemical contaminants/inhomogeneities on the surface and solutes in the liquid [23,24]. The contact angle hysteresis therefore gives important information about the surface geometry (roughness and particle shape) and the surface chemistry (heterogeneity) and information about any particles in the solution. It can also be important when considering solution impurities absorbing on the surface (changing surface chemistry) [25] or swelling [26].

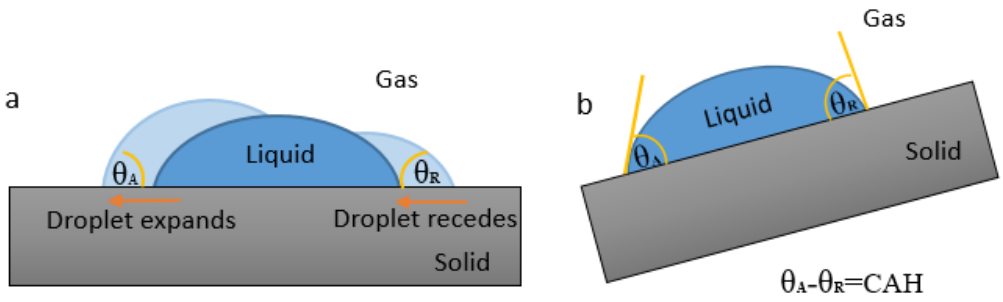

Figure 1.2: The advancing θ_A and receding θ_R contact angles and the equation for contact angle hysteresis (CAH).

CAH can been seen to impact many processes in industry or nature. For example, in nature, it is why raindrops can stick in irregular shapes to window panes. In many industry processes, CAH and alongside other processes (eg. marangoni flows) can be considered a limiting physical factor, in particular for processes that rely on a homogeneous distribution of solutes in deposited droplets [27] or in microfluidic devices [28]. Controlling/avoiding this effect has been the subject of many papers and reviews [22,29,30].

1.4.3 Wetting States on Rough Surfaces

Droplets on flat, homogeneous surfaces usually follow the Young equation. However, in reality most surfaces deviate from the perfection implied by Young's equation, leading to CAH. When considering roughened surfaces, droplets commonly take any combination of two ideal states: the Cassie-Baxter [15] or Wenzel state [14].

In the Wenzel state (Fig.1.3a), the droplet penetrates the surface, wetting the surface corrugations. In the Cassie-Baxter state Fig.1.3b, the droplet does not penetrate the structure but remains suspended on the tops of the surface pillars. This phenomenon is also known as the lotus effect, and can be commonly seen when observing water lilies.

Wenzel suggested that the surface geometry may have a greater effect on contact angle than the surface chemistry and modified the Young equation to correct for surface roughness. He determined that

$$\cos\theta_W = R\cos\theta_Y, \tag{1.2}$$

where the θ_W (Wenzel contact angle) is the apparent contact angle on a rough surface, θ_Y is the Young contact angle (smooth surface) and R is the surface roughness. The result of this equation is that for wetting surfaces the Wenzel contact angle will decrease with surface roughness, whereas for non-wetting surfaces the Wenzel contact angle will increase. The relation is important because it highlights the contrary effect that roughness of a surface can have on the contact angle.

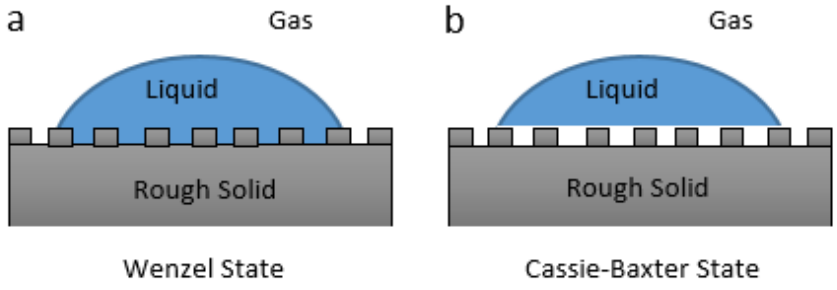

Figure 1.3: Different wetting states on rough surfaces: (a) a droplet on a nanostructured surface in the Wenzel state, (b) a droplet suspended on the pillar tops in the Cassie-Baxter state.

Cassie and Baxter derived an equation which related the apparent contact angle θ_C (Cassie contact angle) of a droplet to the relative fractions of the surface it was

in contact with:

$$\cos\theta_C = f_1 \cos\theta_1 - f_2 \cos\theta_2, \tag{1.3}$$

where f_1 is the fraction of the droplet surface with a contact angle of θ_1 and f_2 is the fraction of the droplet surface with a contact angle of θ_2. This could be considered as the fraction of droplet in contact with posts, with a certain contact angle and the fraction of the droplet in contact with the air in between posts (Fig.1.3a). In the case of a porous surface, or a rough hydrophobic surface where a droplet sits in the Cassie-Baxter state, the above equation reduces to:

$$\cos\theta_C = f_1 \cos\theta_1 - f_2, \tag{1.4}$$

since if f_2 is taken as the fraction of air space, $\cos\theta_2$ reduces to -1 (θ is 180 degrees for non-wetting situations)[31]. The area fractions are related by:

$$f_1 + f_2 = 1, \tag{1.5}$$

For highly ordered structures (such as arrays of pillars) the Cassie-Baxter equation can give a good prediction for the apparent contact angle, but for surfaces with randomly arranged structures, it can be challenging to know the exact fractions of the droplet exposed to surface structures or to the air. This is, for example, the case in this thesis where nano-roughness is obtained through the deposition of nano-particles sprayed onto a solid.

It has also been shown that the contact angle is determined entirely by the interactions of the liquid and the solid at the three phase contact line, and that the rest of the area covered by the drop has no impact on it[32–34]. This conclusion relates to a number of experiments, but in particular, those in which surfaces were prepared with chemically patterned islands. Droplets which contained these islands had the same contact angles as droplets with no islands[34]. This shows that even if the area fraction for different surfaces is different, the result remains the same. Care

should therefore be taken when looking at fractions of surface covered by a drop, and only focusing on the area at the contact line.

1.5 Applications of Controlled Wetting Surfaces

Surfaces with tuned wettability have a plethora of uses, including making microfluidic devices[35], micropatterning cells[36], for anti-fouling coatings,[17,37–39] and water purification[40]. Many of these current applications exploit superhydrophobic and superoleophobic surfaces, but there is a new potential solution based on a liquid infused surface which shall be discussed in detail in chapter 1.6. In this section, the advantages and disadvantages of these different surfaces shall be discussed along with the current limitations.

1.5.1 Superhydrophobic Surfaces

Superhydrophobic surfaces are defined as having a contact larger than 150 degrees and a sliding angle of less than 5 degrees[41]. These surfaces are of interest for anti-fouling coatings[42], self-cleaning[43], anti-fogging applications[44] and anti-corrosive[45]. When constructing a hydrophobic surface, the surface roughness and the surface chemistry must both be considered, since these two factors both contribute to the surfaces hydrophobic properties. By increasing the surface roughness of an already hydrophobic material, the hydrophobicity can be increased[46]. One possibility to increase the contact angle is to control the surface roughness through the addition of surface structure, which was predicted by Wenzel and Cassie-Baxter (see Eqs. 1.2 and 1.4). Modifying the surface chemistry to create a low surface energy can be achieved with the correct choice of materials (eg fluorinated materials), but surface chemistry alone can only increase the contact angle practically to around 120 degrees[47]. Modifying the surface roughness and chemistry must therefore be used in combination to achieve superhydrophobicity. The lotus leaf is a good example that uses a combination of a micro-nano structured surface and the low surface energy of wax crystals that form the hydrophobic lotus leaf surface[21].

The high contact angles and low roll off angles create a surface that easily sheds droplets of water, and leads to a self cleaning surface as the droplets collect any dust settling on the surface and carry it away.

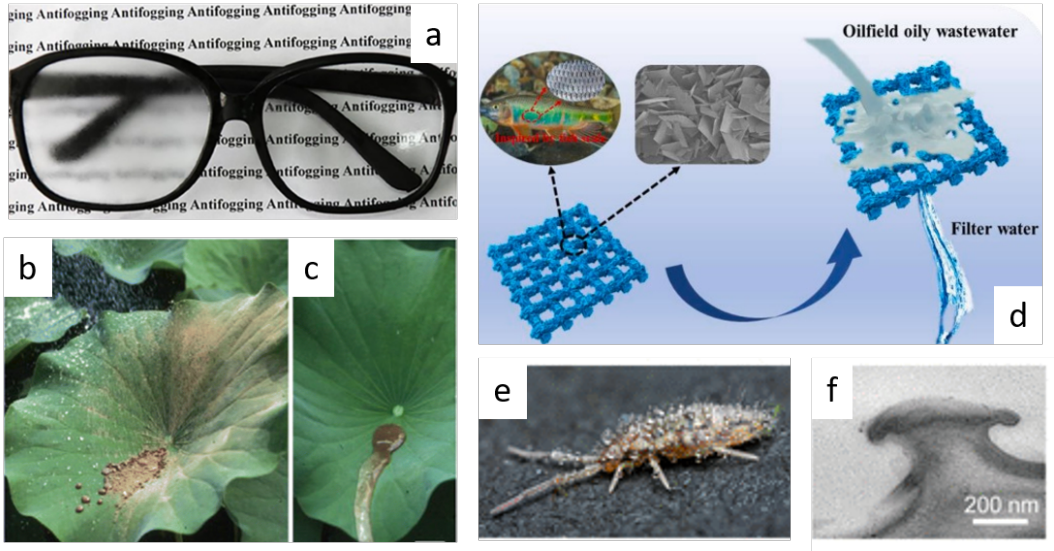

Figure 1.4: Applications and examples of controlled wetting surfaces:(a) Superhydrophobic coatings can be used to create anti-fogging coatings[44]. *Reproduced from X. Yu et al., Highly durable anti-fogging coatings resistant to long-term airborne pollution and intensive UV irradiation. Materials and Design, 194, 108956, 2020. (Copyright 2020 with permission from Elsevier.)* (b and c) A lotus leaf exhibits self cleaning properties due to its unique surface structure and material properties[48]. *Reproduced from K. Koch et al., Multifunctional surface structures of plants: An inspiration for biomimetics, Prog. Mater. Sci., 54, 137–178. (Copyright 2009 with permission from Elsevier.)* (d) Fish scales are the inspiration behind an oil water separation device[49]. *Reprinted with permission from H. He et al., Superhydrophilic fish scale like cuC204 nanosheets wrapped copper mesh with underwater super oil-repellent properties for effective separation of oil in water emulsions. Colloids and Surfaces A: Phsicochemical and Engineering Aspects, 627, 127133, 2021.(Copyright 2021 with permission from Elsevier.)* (e and f) A springtail has a re-entrant surface structure as seen in the zoomed in SE image, giving it a superoleophobic surface[50]. *Reprinted with permission from J. Choi et al., Flexible and Robust Superomniphobic Surfaces Created by Localized Photofluidization of Azopolymer Pillars, ACS Nano, 11, 7821-7828, 2017. Copyright 2017 American Chemical Society.*

1.5.2 Superoleophobic Surfaces

Superoleophobic surfaces are defined as having a contact angle with hydrophobic liquids (such as oil) of greater than 150 degrees[16]. These coatings have attracted significant interest as being capable of being self-cleaning, used for oil-water separation[49], and underwater anti-fouling applications[51]. Again surface structure and chemistry play a key role in their design. When designing superoleophobic surfaces in air, surfaces are created using a re-entrant texture. This makes fabrication more challenging because of the need to have an overhanging structure. When superoleophobic surfaces are designed for use in water, hydrophilic surfaces may be used, since they exhibit underwater oleophobicity. Instead of trapping air (as in the superhydrophobic surface) they trap a water layer. The water preferentially stays in contact with the surface, displacing any oil or fouling that falls on it. A commonly used example are fish scales. They combine a structured surface with a thick mucus which allows the scales to trap water, making them appear superoleophobic when immersed in water[21].

1.5.3 Challenges with Current Wetting Controls

Current wetting controls often suffer from certain limitations which are the subject of many reviews[52–54] (and references within). These include the cost of fabrication of surfaces to obtain superhydrophicity or superoleophobicity which can be expensive and often suffer from poor structural stability and durability. Difficulties in obtaining uniform coatings and preventing damage to coatings can lead to small areas of non-uniform wetting which then leads to surface impingement. In many cases, the materials used may present health and environmental issues or may themselves be toxic. The surfaces usually have selective working conditions, which might be seasonally outside of normal environmental conditions. Slippery surfaces which were mentioned briefly before may solve many of the problems outlined here and are described in detail in Section 1.6.

1.6 Liquid Infused Surfaces

Many of the problems of superoleophobic surfaces can be overcome by liquid infused surfaces (LIS) effectively replacing the solid-liquid interface with a liquid-liquid interface. In practice, LIS offer a complex and rich behaviour because two interfaces are involved in the simplest case.

1.6.1 Liquid Infused Surface Properties

Inspired by the slippery surface of the pitcher plant (Fig.1.5), liquid infused surfaces (LIS) are a family of highly slippery, liquid repelling surfaces [55–57]. They are formed of a nano or micro-structured porous material that is impregnated with a lubricating fluid (usually an oil). The formation of a LIS surface can be seen pictorially in Fig. 1.6.

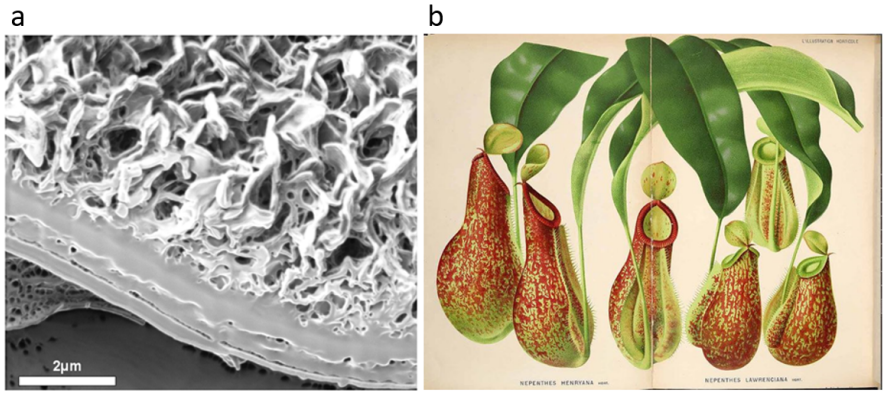

Figure 1.5: (a) A scanning electron microscope (SEM) image of a Nepenthes pitcher plant [58] showing the porous layer sitting above a thicker base layer. The porous layer is imbibed with a thick layer of epicuticular wax. (b) A botanical painting of the Nepenthes pitcher plant [59].

Trapping the lubricant within the porous structure prevents contaminants coming into contact with the fine structured surface and creates a well adhering layer that is highly repellent to any contaminants. This strategy is very flexible and can be applied to a wide range of materials including metals [60], plastics [61] and transparent optics [55]. LIS surfaces have been developed to have excellent liq-

uid repelling properties, making them easy to clean. They can also be designed to have different exploitable qualities such as being anti-icing[62], anti-fogging[63], anti-biofouling[17,37–39] and antibacterial[64]. In addition, they can be designed to transport droplets across surfaces[65] and can have excellent self-healing properties[55].

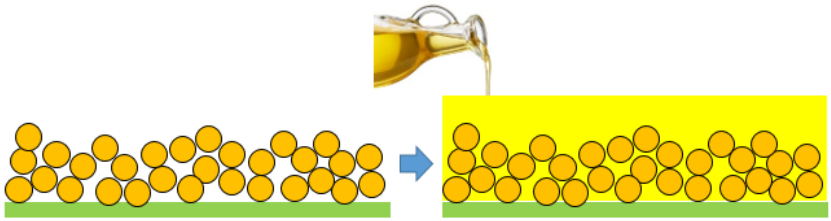

Figure 1.6: A LIS is formed of a porous solid (shown here is an array of randomly arranged silica beads) which is then infused with a lubricating liquid. This leads to a highly slippery surface that sheds droplets even at low tilt angles.

1.6.2 Basic Principles of Liquid Infused Surfaces

LIS surfaces may be formed of many different materials[17–21] but all are fabricated to meet the three main criteria associated with a LIS[66]:

1. The lubricating fluid and the ambient fluid must be largely immiscible,
2. the solid should preferably be roughened so as to increase the surface area for the adhesion of the lubricating fluid and its immobilization,
3. the chemical affinity between the lubricating fluid and the solid should be higher than that between the ambient fluid and the solid.

The final criteria can be represented mathematically by calculating the change in interfacial energies of the lubricating fluid with a droplet of immiscible fluid on its surface $\triangle E_1$ and the change in interfacial energy without a droplet on its surface $\triangle E_2$.

$$\triangle E_1 = R(\gamma_o \cos\theta_o - \gamma_l \cos\theta_l) - \gamma_{lo} > 0, \tag{1.6}$$

and

$$\triangle E_2 = R(\gamma_o \cos\theta_o - \gamma_l \cos\theta_l) + \gamma_l - \gamma_o > 0, \tag{1.7}$$

where R is the roughness factor (the ratio between the actual and projected surface areas of the textured solid first suggested by Wenzel[14]), γ_l and γ_o are the surface tensions for the immiscible fluid droplet and the lubricant, γ_{lo} is the interfacial tension as the interface between the lubricant and the droplet and θ_l and θ_o are the equilibrium contact angles made by the immiscible liquid droplet and the lubricant.

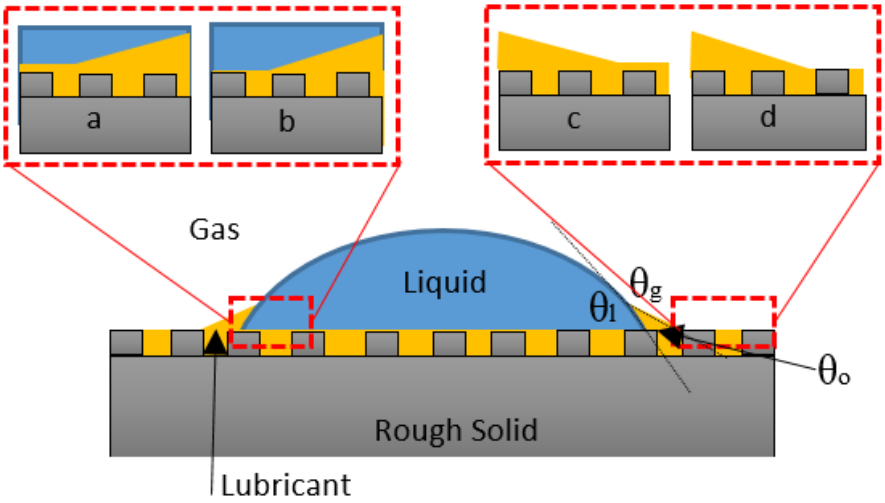

Figure 1.7: A droplet resting on a LIS can be characterised by Neumann angles, θ_g, θ_o and θ_l, representing the gas, lubricant and liquid phase and wetting angles. Four potential wetting states are shown for the droplet; (a) the liquid may be separated from the posts by a thin lubricant layer or (b) touch the posts. For the lubricant - gas interface a similar configuration may occur in that (c) the post may covered by a thin layer of lubricant or (d) be exposed to the air.

When considering LIS as opposed to any other structured surface, the lubricant layer adds in another level of complexity and there are two extra factors to consider: the interaction of the lubricating fluid with the deposited droplet and the inter-

actions of the lubricating fluid with the porous surface. Fig. 1.7 illustrates these two considerations. Not only can there be different geometries for nano-structure-lubricant coverage but there is also the presence of a lubricant ridge, which in some cases can cloak the droplet.

As shown in Fig. 1.7, the lubricant may cover (Fig. 1.7a,c) the structure or expose it (Fig. 1.7b,d) and must be considered in the presence of a droplet and without. The presence of a thin covering film such as found in Fig. 1.7c,d has been proposed [31] to explain the smooth displacement of contact lines (no pinning), as opposed to stick-slip behaviour. In the case of this surface (Fig. 1.7), if the posts were uncovered, upon adding more liquid to the droplet, it would expand on the surface, moving from post to post as the contact angle reaches a certain value (stick-slip). In the presence of a lubricant layer, and with the posts covered, the droplets would expand at a constant rate with no change in contact angle (sliding). Altogether, this means that the presence of posts could change the contact angle measured, the roll off angle and the contact angle hysteresis. It also may depend on the thickness of the lubricant layer and the method of applying the droplet to the surface.

The cloaking of a droplet is shown in Fig. 1.8. When considering the interaction between the lubricating fluid and the droplet, capillary action will cause the lubricant to form a ridge at the droplet base or even completely cloak the droplet. It is important to understand the state which the droplet reduces to, since complete cloaking will change the surface tension of the droplet, and therefore the adhesive properties of the droplet to the surface. The criteria for droplet cloaking can be given by the spreading coefficient S_{OL} [67].

$$S_{OL} = \gamma_{LG} - \gamma_{LO} - \gamma_{OG}, \tag{1.8}$$

where γ_{LG}, γ_{LO}, γ_{OG} are the inter-facial tensions of the liquid-gas, liquid-lubricant and lubricant-gas. If $S_{OL} > 0$ it implies that the lubricant will cloak the droplet while $S_{OL} < 0$ suggests otherwise [67]. As shown in Fig. 1.8, a lubricant ridge is

formed if the lubricant has a moderate surface energy. If the lubricant has a low surface energy, cloaking of the droplet also occurs. It is an important consideration since cloaking would cause a change in surface tension and may lead to progressive loss of lubricant from the surface, leading to a depletion of the lubricant layer.

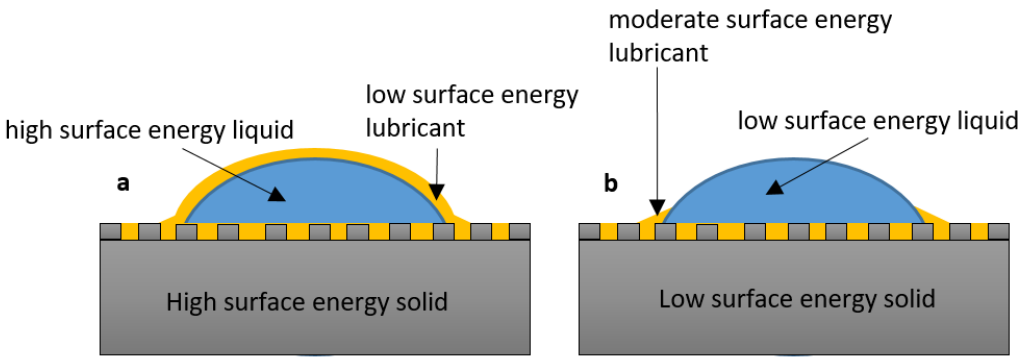

Figure 1.8: (a), A low surface energy lubricant cloaks a droplet on a LIS. (b) A lubricant ridge is formed due to capillary action of the lubricant but does not cloak the droplet [67].

The addition of a lubricant layer also makes calculating the contact angle of the droplet on a LIS more difficult, since different studies often do not make clear where they are measuring their contact angle [55,67]. For this reason, it can prove difficult to compare between studies to determine the surface with the least droplet adhesion. In this study, the definition found in Semprebon et al [31] which defines the apparent contact angle as the angle measured at the point where the three fluid interfaces meet (the triple point) will be used. The main reason for this choice is that it is identifiable from the kink in the droplet profile and thus can be measured both experimentally and using simulations. It is preferable to use this point, since it can be measured directly, without the use of interpolated curve fitting algorithms. The equation for the apparent contact angle, θ_{app} is given by [31];

$$\theta_{app} = \cos^{-1}\left(\cos\theta_l^{CB}\frac{\gamma_{ol}}{\gamma_{lg}} + \cos\theta_o^{CB}\frac{\gamma_{og}}{\gamma_{lg}}\right), \tag{1.9}$$

where θ_l^{CB} and θ_o^{CB} are the Cassie-Baxter angles for the water-lubricant and lubricant-gas phases. γ_{ol}, γ_{lg} and γ_{og} are the surface tensions for the lubricant-water, water-gas and lubricant-gas phases.

After considering the surface properties and behviours of surfaces on LIS, the next section considers different fabrication methods of LIS.

1.6.3 Liquid Infused Surface Fabrication Techniques

As mentioned previously (Chapter 1.4.2), the surface geometry (roughness and particle shape) and the surface chemistry (heterogeneity) are key factors that determine surface wetability. This gives two main methods to create a LIS: modify rough surfaces with a suitable coating or to roughen a surface with low surface energy [68]. While it is not necessary to have a textured/roughened surface to make a LIS, they posses greater lubricant retention than planar devices [69] and so shall be focused on here.

Textured surfaces can be fabricated using a number of methods. Etching using physical (eg lithography techniques [70]) or chemical (eg HF etching [71]) methods or a combination of the two are commonly used to create structured surfaces. These etching methods however can be expensive and complex to create [72]. Other methods of creating the substrate could be electrospinning (spun fibres) [73], spraying [74], electrochemical deposition [75] and polymer wrinkling [76]. Many of the listed surface fabrication procedures can be carried out on the lab bench and can use a number of different materials that can be additionally chemically modified. A lubricant can be applied to the textured surface by a number of methods including dip coating, spin coating and spraying. In this work, nano-particle spraying is used to create a textured surface for the infusion of oil with no further chemical modification of the surface. A lubricant is spin coated onto the surface. The fabrication process is futher discussed in Chapter 2.

Having considered the unique behaviours of LIS and the numerous surface fabrication methods, the next section aims to consider the challenges still facing LIS development.

1.6.4 Challenges and Questions in Liquid Infused Surface Development

LIS surfaces are still a very active research area with many groups looking to construct devices and coatings to solve industrial problems. However, the field is still relatively young and the surfaces themselves are often poorly understood. Many surfaces are simply used, without fully understanding why certain combinations of structures or materials work, and how they could be improved upon.

Within the literature there are many different examples of LIS systems, fabricated using different materials and techniques[17–21,77,78]. This can make comparisons between different studies hard, especially when considering that there are more than 50 choices of lubricant reported for use in LIS[18]. These different fabrications methods range in complexity, fabrication time and cost and hence may not be suitable for commercial application or facile testing in the lab which usually requires an easy, quick and low cost solution.

The ageing and wear of LIS is also often overlooked despite it being considered one of the biggest problems facing self-cleaning surfaces[79]. When available, studies typically examine LIS ageing during static storage in air or in solution at room temperature[80], or under steady external perturbations on freshly made LIS[66,81–83]. Durability is assessed in terms of substrate recovery after damage incidents (such as incision or impact in the infused layer)[17,37,84], lubricant loss, and the ageing of surfaces under soaking conditions. Generally, LIS retain their slippery properties[21,62,85] provided the lubricant layer is not depleted, and periodic re-immersion in lubricant has been shown to allow most LIS to regain their self-healing properties and high droplet mobility[86].

Lubricant loss from the LIS surface is also known to be a problem, since lubricant depletion from LIS causes them to progressively lose their anti-fouling properties and bio-material is able to attach[85]. Several mechanisms may be responsible for the lubricant loss, including exposure to shear flows[81–83], failure under gravity[81], and aqueous droplet cloaking by the lubricant resulting in LIS material being car-

ried away[87]. Further investigation into these lubricant loss mechanisms is needed to understand how they can be controlled or mitigated for.

1.7 Capillary Liquid Bridges as Tools to Study Liquid Infused Surfaces

Capillary liquid bridges (CLBs) are commonly found in nature and in many industrial processes and are created when a droplet of liquid forms a bridge between two surfaces. They are present in many industrial applications such as lithography[88], oil recovery[89], cement drying[90] and with implications for novel methods of drug delivery in medicine[91,92]. In nature they are present in soil and granular mixes such as sand (sandcastles!)[93], in the adhesive pads of numerous insects and small animals[94,95], and help wading birds to feed[96].

Many studies look at CLBs between simple hydrophilic or hydrophobic substrates[97–100]. Evaporation studies[97,99] on CLBs, determine that the evaporation dynamics are dependent on surface wetability and plate separation. Using asymmetric CLBs, and by changing the plate geometry by creating wedges[101] or stretching and compressing the droplet,[102] droplet motion can be controlled. Stretching droplets between surfaces and measuring the CAH has also been looked at,[98,103] with contact angle playing a large role in the hysteresis in the force-separation curve. CLBs may be formed between asymmetrical plates for study[104], or none parallel surfaces such as spheres[105,106]. Theoretical studies have complemented this work[107,108].

However CLBs with 2 liquid components such as those formed on LIS are understudied yet remarkably interesting. Two liquids interacting gives a greater range of morphologies that can be present as the lubricant ridge interacts with the lubricant layer on the surface. In the limit of vanishing meniscus, they present a surface with frictionless properties which does not pin. These frictionless surfaces are advantageous and they have many desirable properties as mentioned previously. There are a number of literature studies that look at droplets on LIS[31,109], or study CLBs between LIS theoretically[110]. To our knowledge, stretching CLBs on LIS has not

yet been considered.

1.7.1 Basic Characteristics of Capillary Liquid Bridges

Before going on to describe specific CLB phenomenona, it is first helpful to characterise the basics. The main geometrical parameters used to describe CLBs are (1) the angles θ_1 and θ_2 formed by the liquid and the contacting surfaces, (2) the height h of the CLB, (3) the radii of contact R_t and R_b at the top and bottom surfaces, and (4) the radii of curvature R_1 and R_2 of the surface of the CLB (Fig. 1.9). R_1 and R_2 are shown in Figure 1.9 at the point of contact between the CLB and the top contacting surface.

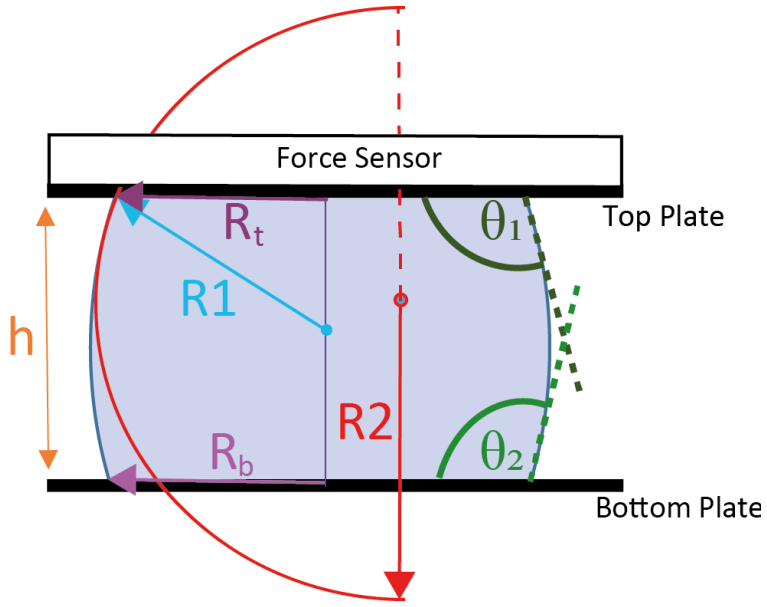

Figure 1.9: Cartoon representation of a typical CLB between parallel surfaces. The CLB can be quantitatively described and modelled using the contact angles θ_1 and θ_2 formed by the liquid with each surface, the height h of the CLB (here the distance between the surfaces), the radius of contact R_t and R_b of the CLB with the top and bottom surfaces, and the curvature of the CLB surface obtained by two radii of curvature R_1 and R_2 taken orthogonally from each. Here the radii R_1 and R_2 are taken at the point of contact with the top plate but they can, in principle, be taken anywhere on the CLB at equilibrium.

The CLB exerts a capillary force on the contacting surfaces. The magnitude and direction of this force depends on the specific geometry of the system. Gravity is

also present and its effect may have to be taken into consideration, depending on the size and volume of the CLB. In larger CLB, the gravity-induced differential hydrostatic pressure between the top and the bottom of the CLB results in an asymmetric shape.

The geometrical parameters of the CLB can be related to its capillary force F. In the case where gravity can be ignored, the capillary force for a symmetric CLB between two identical parallel surfaces is given by[111,112]:

$$F = -2\pi\gamma R\sin(\theta) + \pi R^2\gamma\left(\frac{1}{R_1} + \frac{1}{R_2}\right), \tag{1.10}$$

where γ is the surface tension of the liquid, and it is assumed that $\theta_1 = \theta_2 = \theta$ and $R_t = R_b = R$ by symmetry. This equation assumes equilibrium and a CLB size well below the capillary number. When gravity becomes important, the CLB is no longer symmetric. In this case, the capillary force at the top plate can be expressed as:

$$F_t = -2\pi\gamma R_t\sin(\theta_1) + \pi R_t^2\gamma\left(\frac{1}{R_1} + \frac{1}{R_2}\right), \tag{1.11}$$

Here, the radii of curvature R_1 and R_2 are measured at the top plate. For the bottom plate, the magnitude of the capillary force includes an additional term due to gravity[111] , and is given by:

$$F_b = -2\pi\gamma R_t\sin(\theta_1) + \pi R_t^2\gamma\left(\frac{1}{R_1} + \frac{1}{R_2}\right) + \rho g V, \tag{1.12}$$

where ρ is the density of the droplet solution, V is the CLB volume, and g is the acceleration of gravity. Alternatively, the capillary force for the bottom plate can be written in a form akin to Equations 1.10 and 1.11:

$$F_b = -2\pi\gamma R_b\sin(\theta_2) + \pi R_b^2\gamma\left(\frac{1}{R_1} + \frac{1}{R_2}\right), \tag{1.13}$$

with the radii R_b, R_1 and R_2 and contact angle θ_2 are all now measured at the bottom plate. Equations 1.10 - 1.13 can also describe CLBs on LIS when stationary and at equilibrium.

1.7.2 Practical Experimental Considerations and Common Issues

In a typical experimental measurement, the geometry of a CLB is tracked by a camera, while a given parameter (here the distance h between the surfaces) changes continuously. The associated capillary force F experienced by one of the contacting surfaces is also measured. The CLB geometry is usually extracted from 2-dimensional (2D) video images of the bridge that have to be synchronised with the force measurements.

Most experimental measurements are faced by several challenges. One key problem stems from assuming symmetry and uniformity over the entire CLB. This is implicit as a 2D image is used to extract all the geometrical parameters (θ_1, θ_2, h, R_t, R_b, R_1 and R_2) assumed to represent the bridge at equilibrium. For large CLBs, or CLBs experiencing pinning on the surface, this assumption may not be valid because the optical image may miss pinned points. Yet the measured force is sensitive to such pinning points, resulting in a disagreement between the measured force and that calculated from the geometrical parameters. Liquid evaporation may lead to time-dependent changes in the force over longer measurements due to changes in the CLBs volume. Using larger CLBs can reduce the relative importance of evaporation effects, but at the cost of needing to take gravity into account. Alternatively, CLBs can be made of liquids less susceptible to evaporation (e.g. water-glycerol mixture instead of pure water[36,113]) and make use of a controlled environment (e.g. humidity, temperature[114,115]).

1.7.3 Working with Capilliary Liquid Bridges on Liquid Infused Surfaces

Measuring CLBs on LIS is more challenging than with non-LIS for several reasons. Firstly, the changes in capillary forces as the CLBs are stretched are typically an order of magnitude lower than for CLB of the same size but involving non-LIS surfaces. Secondly, while LIS are of interest precisely for the absence of contact line pinning[116,117] and the ability of droplets to roll off easily[18], these proper-

ties render CLB measurements more challenging due to increased CLB mobility. Additionally, the liquid layer of the LIS (typically oil) can create a visible ridge around the CLB-LIS contact regions or may cloak the whole CLB rendering precise determination of θ more difficult (Fig.1.6). The contact angle must then be approximated either by fitting the CLB edge and extrapolating the obscured region (Fig. 2b) or by approximating the contact angle using geometrical arguments [31]. When focusing on cases with small lubricant ridges, these two approximations converge to the same value. However, for larger lubricant ridges, their values can differ significantly and it is important to employ consistent radii and contact angle definitions in Eq. 1.10 and Eq. 1.11. For practical reasons, it is often convenient to define them at the droplet-lubricant-gas contact line.

The impact of the lubricant ridge on the measurements depends on the thickness of the LIS liquid layer, thus rendering the issue system dependent. The ridge may also impact the measurement of the curvature, depending on which approximations are used, and its size can grow during the measurements, something that needs to be taken into account when studying changes in the contact angles. To overcome this issue, a solution with a dye dissolved in the droplet so the LIS liquid [118] can be used so as to highlight the contact line or contact angles. There is, however, some concern that dye molecules could affect the surface tension of the fluids and hence the contact angles measured.

In this thesis, liquid bridges are used to investigate capillary forces on LIS by forming a CLB between two substrates. The bridges are modelled using Eq.1.10-1.13 and different experimental limitations are overcome. Working with lubricant infused surfaces can make the system more challenging to work with due to cloaking related phenomena, but also allows for a frictionless surface to be explored alongside other conventional substrates.

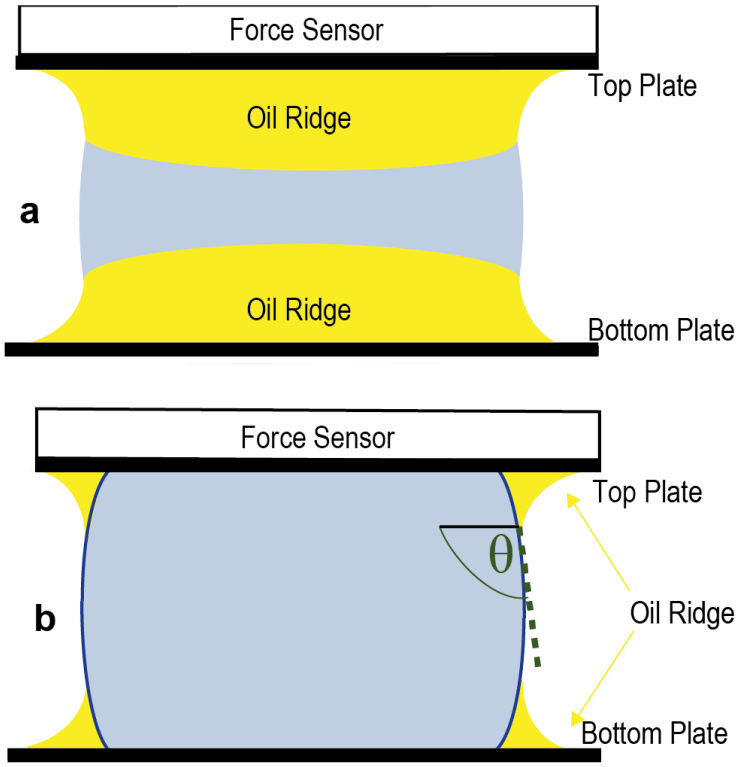

Figure 1.10: Cartoon of a CLB between two LIS with an apparent lubricant ridge. (a) Lubricant ridges as seen in a camera image of the CLB. The lubricant ridges develop when thicker lubricant layers are used on the LIS, obscuring the contact angle of the CLB with the surface. (b) A section through the middle of the CLB illustrates the situation from the perspective of the CLB geometrical characterization. The contact angle is approximated by taking the apparent contact angle measured at the three-phase contact line between the droplet, lubricant and surrounding gas.[31]

Chapter 2

Materials and Methods

2.1 Chapter Outline

This chapter will introduce the key methods and protocols used in this thesis. First, the fabrication of the liquid infused surfaces (LIS) and control surfaces (DMS) is presented. Different characterisation techniques are then used to review the surfaces including contact angle (CA) and contact angle hysteresis (CAH) measurements, atomic force microscopy (AFM), dynamic light scattering (DLS) and simulation methods.

2.2 Liquid Infused Surface Fabrication

The LIS used in this thesis are composed of a silicone nano-particle porous network, infused with silicone oil (20 cst at 25 degrees). The silicone nano-particles are commercially available as a spray (Glaco^{TM} [119]), whose surfaces are modified with attached perfluoroalkyltrichlorosilane groups which help the beads to adhere to the fabrication surface (and each other). The nano-particles are around 40 nm in diameter including the attached perfluoroalkyltrichlorosilane groups. The use of commercially available Glaco^{TM} spray and silicone oil permits a relatively cheap

LIS to be constructed. The surfaces are easy to make, and provide reproducible results, making them suitable for research purposes.

The surfaces were made as following a literature protocol[120]. First, glass substrates were cleaned using Decon 90 (Sigma-Aldrich-Merck, Gillingham, UK), followed by alternating steps of rinsing and sonication (30 min bursts) in ultrapure water (18.2 mW, Merck-Millipore, Hertfordshire, UK). The slides were then left to dry in air. Subsequent rinsing of the slides was carried out consecutively in acetone (purity 99% (Emplura), Sigma-Aldrich-Merck, Gillingham, UK), and isopropanol (purity 99.8 %, Fisher Scientific, Loughborough, UK) and dried under a stream of nitrogen. After 30 mins in air, a layer of hydrophobised nanoparticles was sprayed evenly across the slide surface (GLACO^{TM} spray, SOFT 99 Corp., Japan) and left to dry for 60 mins. Additional layers were applied every hour until a total of five coats was achieved unless otherwise specified (see Chapter 3, Section 3.2 for a study on the optimal number of layers). A drop (0.5 mL) of silicone oil (20 cSt @ 25 °C, Sigma-Aldrich-Merck, Gillingham, UK) was then placed at the centre of the slides and immediately spin coated (1000 rpm 1 min, then 500 rpm 1 min). Slides were used fresh, and any storage was done with the slides placed in petri-dishes with closed lids at ambient temperatures. Hereafter when discussed, these surfaces are referred to as LIS.

2.3 Silanisation of Control Glass Surfaces

Glass slides can be functionalised by silanisation with a suitable molecule in order to provide a good comparison with LIS: when silanising with dichlorodimethylsilane (DMS) the surface of glass exhibits a similar static contact angle but experiences phenomenon such as pinning and contact angle hysteresis. It is very flat and has no porous layer. This means it can be used as a control to investigate the oil retention properties of LIS, which has a greater oil retention due to the rough, porous structure. Careful preparation of the glass prior to silanization is key to getting reproducible, evenly silanised slides with no imperfections.

The surfaces were prepared as following a literature protocol [121]. First, glass slides were placed in a teflon rack in a sonic bath (30 degrees for 30 mins) in acetone (purity 99% (Emplura), Sigma-Aldrich-Merck, Gillingham, UK). (Sigma-Aldrich-Merck, Gillingham, UK). The solution was changed to Isopropanol (purity 99.8 %, Fisher Scientific, Loughborough, UK) and sonicated for a further 30 mins (30 degrees). Slides were dried under a stream of nitrogen then plasma cleaned for 10 minutes at a power of >30 mW. The slides were then oven dried at 100 degrees for 60 minutes. In a fume hood, the slides were placed in a desicator with 1ml of dichlorodimethylsilane in an open dish. They were placed under vacuum for 2 hours, then left overnight. The slides were then rinsed with acetone (purity 99% (Emplura) and dried under a stream of nitrogen. They were dried at 40 degrees overnight and then stored in a closed container for up to 3 months. Hereafter these surfaces are referred to as DMS surfaces.

2.4 Characterization of the Infused Oil Layer Thickness

Getting a well characterised oil layer is important to prevent any variation in oil layer thickness from changing measurement conditions, or influencing the cloaking behaviour (or thickness). In this thesis the oil layer was characterised by weighing and also checked using equations for expected thin film thickness after spin coating.

2.4.1 Characterisation by Weighing

The nanoparticle-coated slides were weighed before and after spin coating with silicone oil. Knowing the oil density and the area of the slide, a thickness for the oil film could be derived. This approach is convenient to track oil losses and rapidly estimate changes in the infused layer thickness. However, it rests on the assumption of a uniform, homogeneous oil film and neglects any of the oil contained within the rough porous nanoparticle layer. These assumptions are broadly justified

considering the order magnitude in thickness difference between the oil and porous layers, at least for fresh samples. Values obtained are in the range of 6 – 8 μm when a slide is spin coated for 1 min (1000 rpm). This can be shown physically in Figure 2.1 where the oil layer thickness is shown as a function of spin coating time. The majority of oil is shed within the first 10 minutes before the oil layer reaches a point of stability where no more oil is shed.

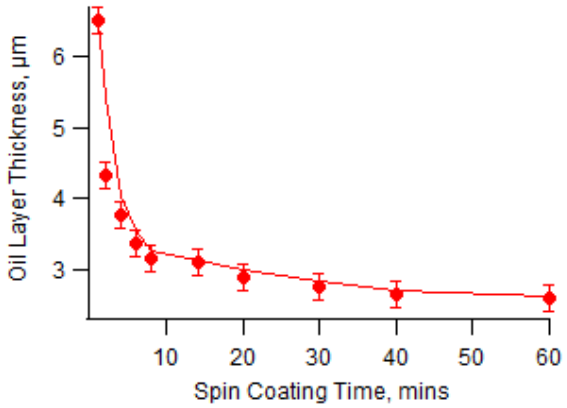

Figure 2.1: The oil layer thickness over a typical nanoparticle-coated glass slide, as found by weighing the slide after spin coating. The oil is mostly shed within the first 10 minutes. After this initial heavy loss, the oil loss steadily becomes slower until it reaches a plateau and the oil layer is stable. The error bars shown are the standard error of 3 measurements.

2.4.2 Characterisation of the Oil Thickness Using Theoretical Considerations

Another method used to estimate the oil film thickness is also shown here for completeness, spin coating model developed by Emslie et al [122]. The model assumes a Newtonian fluid – a good approximation for silicone oil – and that the fluid flow is unidirectional in the radial direction. Using this model [122], the film thickness h, can be expressed as follows:

$$h = h_0 \sqrt{\frac{1}{2Kh_0^2 t + 1}}, \tag{2.1}$$

where h_0 is the initial height of the oil film, t is the rotation time, ρ is fluid density,

ω is the angular velocity of the spin coating platform, μ is the fluid viscosity, and K is given by:

$$K = \frac{2\rho\omega^2}{\mu}, \tag{2.2}$$

This equation can be further simplified if one assumes that:

$$Kh_0^2 \ll 1. \tag{2.3}$$

leading to

$$h \approx \sqrt{\frac{\mu}{\omega^2 t}}. \tag{2.4}$$

In this work, for thin oil layers, ω is 104 rad/s, μ is 2 x $10^{-}5$ m^2/s and t is 60 s. Thus, Eq. 6 gives a value of around 5 μm. This is in agreement with the weight measurements, which place the oil layer thickness between 6-8 μm.

2.5 Controlling Evaporation

Controlling the volume of the droplets or CLBs is essential in this work, since the image parameters are often calibrated assuming a constant droplet volume. For short timescale experiments, such as in characterising or ageing experiments (Chapter 3 and 4), ultra pure water is often used. However for longer experiments, such as stretching CLBs (Chapter 5 or 6), droplets which are more resilient against evaporation are required. Figure 2.2 shows the evaporation of either water (blue) or 80% glycerol droplets (red) on a DMS and LIS surface. An 80% glycerol solution is used as a compromise to pure glycerol, since it has a low enough viscosity to pipette, yet a low enough water content to have very slow evaporation. The 80% glycerol droplets (either 10μl or 2μl) show almost no evaporation over 2 hours, while the pure water droplet evaporate significantly within the same timescale.

The droplets on the LIS surfaces show a slower evaporation than the droplets on the DMS surface, suggesting that the droplets may be cloaked by a thin oil layer on the LIS. Evaporation may also be affected by temperature and humidity, which are further discussed in sections 2.7.3 and 2.7.4.

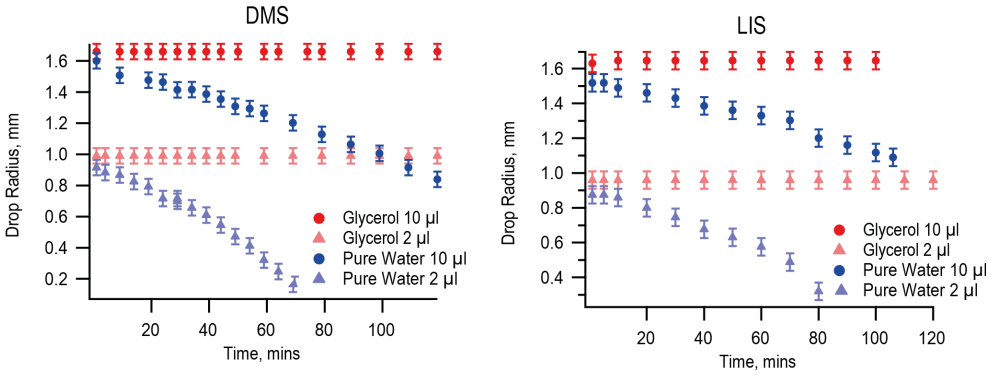

Figure 2.2: Droplet evaporation using pure water (blue) and 80% glycerol solutions (red) is shown on two different substrates under similar environmental conditions. Pure water droplets show significant evaporation on short timescales, this is particularly true for smaller 2 μl droplets which evaporate completely within 70-80 mins (light blue trace, both plots). The glycerol droplets show very slow evaporation on these timescales. The droplets on the LIS show slower evaporation than on the DMS, suggesting cloaking by a thin layer of oil.

2.6 Surface Tension Characterisation

For many liquids, their surface tension is well characterised with air but not for other combinations of liquids. This means that rather than simply using literature values, experiments or approximations must be made in-house to find these values. Table 2.3 shows the available data from the literature, alongside measured values taken using Opendrop [123,124], which is described below. These values, when used in combination with the cloaking film tension approximation can be used to estimate the surface tension of the cloaked droplet.

Interacting Media	**Literature Surface Tension mN/m at 25 degrees (if available)**	**Measured Surface Tension mN/m (Opendrop)**
Pure water - air	72.02	71.33 ± 2
Pure water - Silicon Oil (20cst)	N/A	29.5 ± 2
Glycerol (80%) - air	(78% glycerol) 67.4	60.12 ± 2
Glycerol (80%) - Silicon Oil (20cst)	N/A	27.6 ± 2

Table 2.1: List of the different surface tensions available or measured for different media used in this thesis.

2.6.1 Pendant Drop

Pendant drop experiments in conjunction with Opendrop [123,124] software were used to calculate the surface tension of the different media as shown in Figure 2.3. A camera images a hanging droplet formed using a needle. The hanging droplet is illuminated with a bright light source, to make the droplet shape easily visible to the camera. The shape of the droplet is controlled by two key forces, surface tension and gravity. The surface tension wishes the droplet to be spherical, i.e. minimising the surface area while gravity acts on the droplet pulling it to form a pendant shape droplet. The shape of the droplet can be explained by the Young-Laplace equation which describes the pressure difference between the outside and inside of the droplet. The Young-Laplace equation is given by [9]:

$$\Delta P = \sigma + \left(\frac{1}{R_1} + \frac{1}{R_2} \right), \tag{2.5}$$

where ΔP is the pressure difference, σ is the surface tension and R_1 and R_2 are the principal radii of curvature as shown in Figure 2.3. This change in pressure can also be expressed as the following in the presence of gravity [125]:

$$\Delta P = \Delta P_o + \rho g z, \tag{2.6}$$

These equations taken together give:

$$\left(\frac{1}{R_1} + \frac{1}{R_2}\right) = \frac{2}{R_1} + \frac{\rho g z}{\sigma}, \tag{2.7}$$

where σ can be isolated and calculated.

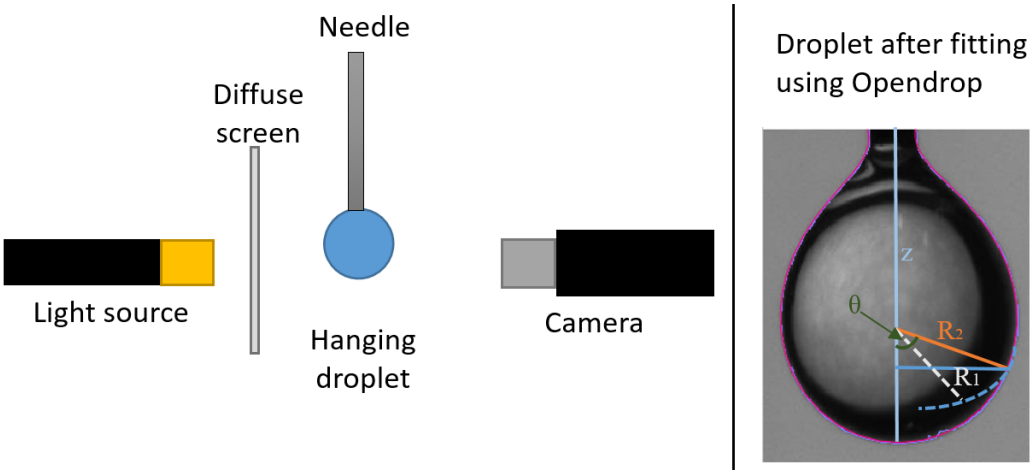

Figure 2.3: A camera images a hanging droplet formed using a needle. Water is continuously added to the droplet till it grows large enough to be affected by gravity. The shape of the droplet as it is affected by surface tension and gravity can be used to determine the surface tension by fitting the droplet profile. The droplet is backlit with a bright light source, to make the droplet shape easily visible to the camera. Opendrop is then used to fit the droplet profile (red line in droplet image) and calculate the surface tension.

2.6.2 Cloaking Film Tension Approximation

Deriving an effective surface tension for a droplet or liquid bridge which is cloaked is not straightforward because the apparent surface tension of a cloaked liquid is

known to change with the thickness of the cloaking thin film [55]. It is not possible in this work to measure the thickness of the cloaking film which may not be uniform and evolve over the course of an experiment, including possible lubricant transport between the two surfaces through the CLB. The effective surface tension is therefore approximated using the following equation [126]:

$$\sigma_c = \sigma_{dl} + \sigma_{la}, \tag{2.8}$$

where σ_c is the cloaked surface tension, σ_{dl} is the droplet-lubricant surface tension and σ_{la} is the lubricant-air surface tension. This gives a value of 48.2 mN/m (Opendrop [123,124]) using in-house measurements and 52.9 mN/m using literature values [126]. To reflect this uncertainty an effective surface tension value of 50 ± 2 mN/m is used throughout, averaging between these two values.

2.7 Contact Angle Characterisation

The CAs formed by droplets and CLBs with the contacting surface (glass, DMS or LIS) are studied throughout this work. CA characterisation is particularly used to study surface formation in Chapter 3, sample ageing in Chapter 4 and characterise CLB changes during stretching in Chapter 5. In this section, the methods for characterising these angles will be discussed. This section begins by looking at static droplets, before looking at the measurement of droplet advancing and receding angles. For droplets, the analysis is done with a FIJI freeware. The measurement of CAs in CLB assemblies will then be briefly presented , with a further discussion on this available in Chapter 5. This section will also cover how changes in laboratory environment such as the temperature and humidity affect the measurement of contact angles.

2.7.1 Droplet Contact Angles

The equipment for measuring droplet contact angles was set up as shown in Figure 2.4. A droplet is placed on the substrate under analysis and illuminated from behind. The light source is placed behind a screen to make the light more diffuse and to also provide a plain background for imaging against. A micropipette is used to deposit droplets on the substrate surface. For a static contact measurement, the droplet would then be imaged directly. For CAH measurements, a 10 μl droplet was first deposited on the surface. A second droplet (around 10 μl) was then slowly added to measure the advancing angle and subsequently removed to obtain the receding angle while video-recording the experiment. Stills of the videos were then analysed to derive the advancing and receding angles in the same way as static images.

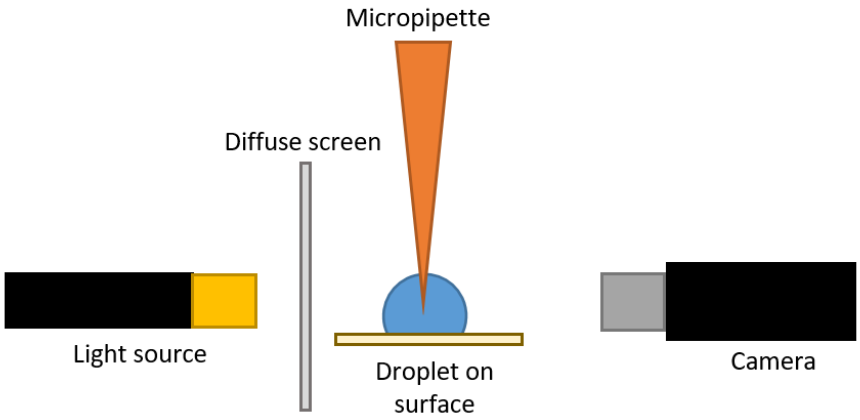

Figure 2.4: A droplet is placed on the sample surface and illuminated by a lamp. A screen makes the light more diffuse and gives a clean background for imaging against. The droplet is applied to the surface using a micropipette. For measurements of advancing and receding contact angles, the micropipette is held in a clamp stand and liquid gently added or removed from the droplet.

All droplet contact angle (CA) images were captured using a portable digital microscope (Dino-lite Edge) and analyzed using FIJI freeware, in particular FIJI plugins Dropsnake[127,128] or Contact-Angle[129]. Contact-Angle, written by Marco Brugnara, uses a baseline drawn by the user and three points on the droplets surface, to estimate the droplet to either a circle or an ellipse. The program works well

for smaller droplets (10-20 μl drops) with CAs below 120 degrees, but for larger droplets it is less accurate. Dropsnake, developed by the biomedical imaging group at EPFL Switzerland, was used for larger droplets. Because Dropsnake does not assume the droplet is axisymmetric, it can account for differences in the left and right angles due to pinning. The baseline may also be altered to account for small deviations from a perfectly horizontal surface. Fig.2.5 shows a comparison between the two programs for a surface which has a large contact angle and pinning.

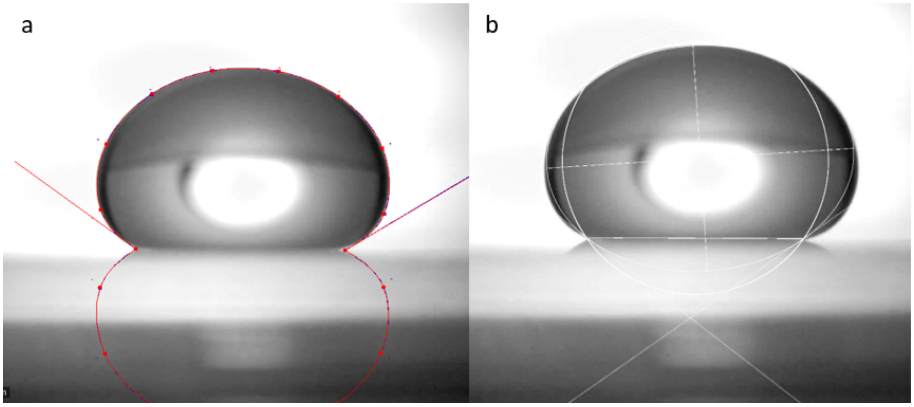

Figure 2.5: Dropsnake and Contact-Angle were both tested for use with large droplets resting on a glaco surface which is not infused by oil. (a) Dropsnake is able to perform a good fit on the droplet, (b) while Contact-Angle is not able to detect the surface correctly.

The angles may also be measured by hand in ImageJ, using the angle measuring tool, but this is highly dependent on the user since they decide at which point the angle should be taken. It can be useful however, to give a quick measurement to obtain a ballpark figure.

2.7.2 Contact Angles in Capillary Liquid Bridges

While there are a number of extremely good programs that can be used to measure droplet CAs, there is, to our knowledge, no freely or commercially available software for CLBs. Chapter 5 directly addresses this lack of software for measuring CLBs. A setup that can perform the physical measurements and a software that can analyse CLBs parameters from videos is developed. This software is built in python and extracts not just contact angles but other CLB parameters such as the CLB contact

radius, radius of curvature and height.

2.7.3 Effect of Temperature on Contact Angle Measurements

Temperature changes must be taken into consideration since they can affect the measured droplet and CLB parameters. For each measurement set, the temperature and humidity were taken during the experimental procedure. It is particularly important to also consider fluctuations when calculating measurement errors. In many measurements, a perspex box was used to ensure constant temperature and humidity for the duration of experiments. To account for the variation in CA as a result of temperature fluctuations, the Young equation [9] is considered:

$$\sigma_{sg} = \sigma_{sl} + \sigma_{lg}\cos(\theta), \tag{2.9}$$

where σ_{sg} is the surface tension of the solid-gas interface, $\sigma_{sl}$is the surface tension between the solid and the liquid drop, σ_{lg} is the surface tension between the liquid droplet and the gas, and θ is the Young's contact angle. When considering a LIS system, with the droplet interacting with the oil layer, Eq. 2.10 can be changed to:

$$\sigma_{og} = \sigma_{ol} + \sigma_{lg}\cos(\theta), \tag{2.10}$$

where σ_{og} is the surface tension of the oil-gas interface, $\sigma_{ol}$is the surface tension between the oil and the liquid drop, σ_{lg} is the surface tension between the liquid droplet and the gas, and θ is the Young's contact angle.

An example of a calculation of the contact angle variation due to temperature flucuations using Eq. (2.10) for a pure water droplet on a LIS is shown here. A number of assumptions were made to simplify the calculation. Firstly, the values of σ_{og} (20.6 mN/m at 25 degrees Celsius) and σ_{ol} (33.1 mN/m) are assumed to be constant. For the variation of water surface tension as a function of temperature, the data provided by the Dortmund Data Bank is used [57]. Taking the temperature

range between 10-40 degrees centigrade, a variation of approximately 1% in the contact value per degree Celsius is found.

2.7.4 Effect of Humidity on Contact Angle Measurements

Humidity fluctuation should also be considered when making assumptions of the errors on measurements. Experimentally, Diaz et al[130] and Portuguez et al[131] showed how the relative humidity can affect the surface tension of pure water droplets. For this work, the humidity can be considered to vary maximally between 30 % and 90 % in the laboratory setting. For an example calculation, using a pure water droplet on a LIS, σ_{og} is taken to be 20.6 mN/m and σ_{ol} to be 33.1 mN/m. Over the range of humidity considered, this leads to a variation in the contact angle of 2 degrees, or 2% of the measured value.

2.8 Atomic Force Microscopy

Atomic force microscopy (AFM) was used for small sections of this thesis where nanoscale information was needed for a given sample. This is seen in Chapter 3 when characterising the surface roughness of nanoparticle-coated glass and when imaging nano-droplets formed in an emulsion in a LIS (Chapter 4). Being able to visualise the surface at the nanoscale allows us to open a window to another previously unseen aspect of LIS.

2.8.1 An introduction to Atomic Force Microscopy

Atomic force microscopy (AFM) was first introduced in the 1980s by Binning and colleagues[132]. This non-optical technique can be very powerful for visualising nanoscale features on surfaces and can give information about surfaces' topographical, electrical, magnetic, chemical, optical and mechanical properties[133–135]. This technique is particularity useful here since imaging can take place in different mediums such as air or liquid, or indeed in no medium (a vacuum). This wide range

of measurable parameters and flexibility in the measurement medium make AFM able to image almost any surface.

In practise, AFM uses a very sharp tip which is attached to a thin, flexible cantilever. A laser is reflected from the back of this cantilever which hits a position sensitive photodiode (PSPD). Interactions of the tip with the surface cause the cantilever to bend and reflect the laser onto a different area of the PSPD. In its simplest mode of operation, a feedback loop keeps the interaction force with the surface constant by controlling the cantilever extension as it moves along the surface. The laser deflection gives indications about the surface topography and the interaction force between the tip and the sample. These interactions can be a combination of long/short range and attractive/repulsive forces that are superposed together. Typical interactions include Van der Waals, electrostatics and Coloumb interactions, but also from forces arising from larger force effects such as the capillary forces which result from water molecules forming CLBs between the tip and the surface.

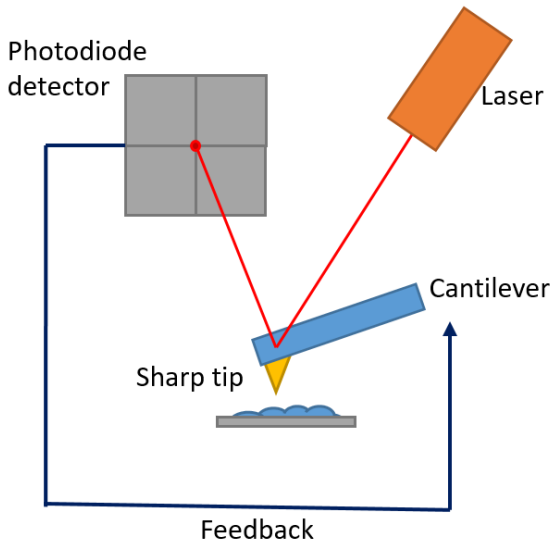

Figure 2.6: A schematic of a typical AFM experiment is shown. A Sharp tip attached to a cantilever probes the surface. The deflection of the laser onto a photodiode tracks the interaction of the tip with the surface and gives information about the surface topology, chemical and mechanical properties. A feedback loop keeps the interaction of the tip with the surface constant.

2.8.2 Imaging Modes in Atomic Force Microscopy

In order to achieve images of a surface, the AFM tip is raster-scanned across the sample, while maintaining constant a specific parameter or group of parameters affected by tip-sample interactions. Typically, these parameters can include the static deflection of the cantilever (static modes) or its vibration amplitude, phase or frequency of an externally oscillated cantilever (dynamic mode). The most common and popular static and dynamic modes of operation are called 'contact' and 'tapping'. Both modes provide valuable but different information about the sample.

In contact mode, the tip maintains contact with the surface, and the interaction force is kept constant by keeping constant the deflection of the cantilever. This is achieved using an electronic feedback loop. The deflection can be directly related to the force using Hookes Law ($F = kx$).

There are three main imaging concerns when taking data in contact mode, namely damage to sample, compressing sample and short range attractive forces, such as the capillary forces induced by CLBs between the tip and the surface in ambient conditions. The constant surface contact also creates high-shearing forces between the sample and the tip which can damage delicate samples and the tip itself. For these reasons, this method of imaging is frequently replaced with tapping mode.

In tapping mode, the cantilever is externally oscillated at near its resonance using an acoustic wave or a pulsed laser. When the tip interacts with the surface, the oscillation amplitude, phase and frequency are all affected, and their variations can be quantified by the reflected laser. In tapping mode, the amplitude is kept constant while raster scanning, with the other parameters free to vary. Operating in tapping mode reduces the high shear forces between the tip and the surface and reduces imaging damage. The measurement of the tip-surfaces interactions also changes from being a direct measure of the cantilever deflection, to the amplitude variation as a result of tip-surface interactions. As the tip-surface separation changes in response to the feedback, so does the damping of the oscillations. This gives the

user information about not only the height measured, but also about the nature of the interactions experienced by the tip (e.g. viscous or elastic). When interpreted in the context of a known sample, this information can often be interpreted in terms of sample mechanical or chemical properties.

2.8.3 Phase Theory in Atomic Force Microscopy

In tapping mode, as well as topographical information about the substrate, information about the stiffness of the substrate can also be obtained by looking at the phase information. When the tip, which is oscillating, comes into close contact with the surface, changes are observed in both amplitude and phase. As hinted in the previous section, while the amplitude is used to derive topographical information, the phase shift can help distinguish regions with different mechanical properties. This principle is illustrated in Figure 2.7: the red and the blue surfaces have different surface properties, where the red is softer than the blue. This results in a phase lag appearing between the driving oscillation and the measured oscillation. A good example can be seen when imaging bare (un-infused) LIS (Figure 2.7). The LIS are constructed from a nano-particle spray, with the nano-particles coated in a perfluoroalkyltrichlorosilane film. This means when imaging, the harder silica core can be differentiated from the softer perfluoroalkyltrichlorosilane corona as shown in insets Figure 2.7.

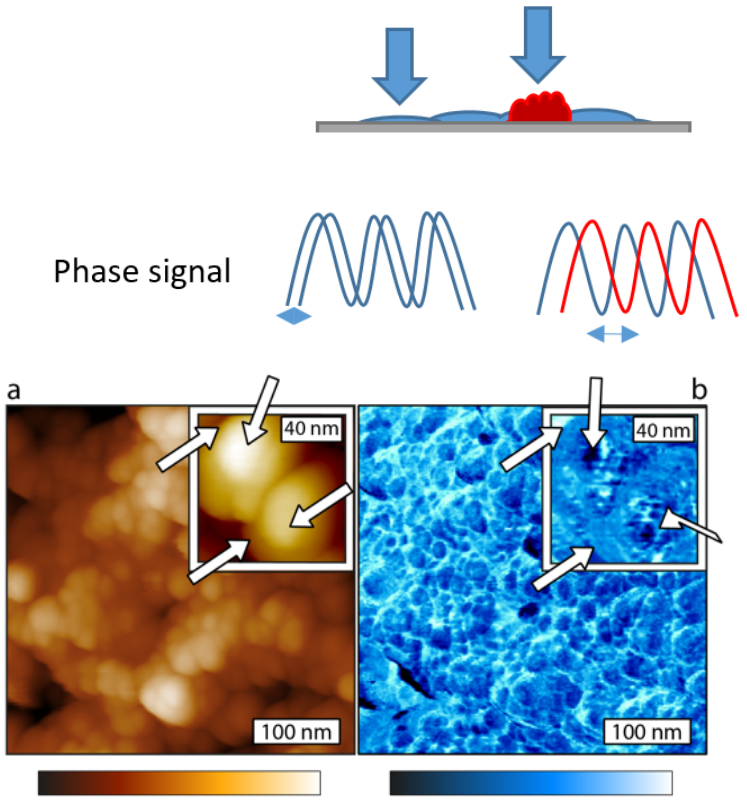

Figure 2.7: Different tip-sample interactions over the hard core and softer shell leads to clear phase variations not visible in topography. The harder silica core can be seen surrounded by the softer perfluoroalkyltrichlorosilane coating (insets) with the centre and edge indicated by arrows.

2.9 Dynamic Light Scattering Characterisation

Dynamic Light Scattering (DLS) is used in this thesis to characterise the formation of small oil droplets in water when LIS are exposed to harsh ageing conditions, (Chapter 4) and aids in the discussion of ageing of LIS and their associated oil layers.

Dynamic light scattering (DLS) can be used to track the Brownian motion of particles in solution and relate this back to the size of particles, assuming an unbiased diffusion. The idea is to exploit the relationship between particle size and mobility: small particles move more quickly under Brownian motion than larger ones. The

Stoke-Einstein equation gives the diffusion coefficient which is used by the DLS to characterise size.

$$D = \frac{\kappa T}{3\pi\eta d_h}, \tag{2.11}$$

where κ is the Boltzman constant, T is the temperature, η is the viscosity of the liquid and d_h is the hydrodynamic diameter.

Practically, as part of the DLS setup, particles in solution are illuminated by laser (monochromic light source) and the light scattering or speckle pattern produced is recorded. By calculating the auto-correlation between successive patterns, a diffusion timescale can be extracted and subsequently used to extract the size of the moving particles using Eq. 2.11. In principle several populations of particles can be identified simultaneously although this increases the associated error considerably.

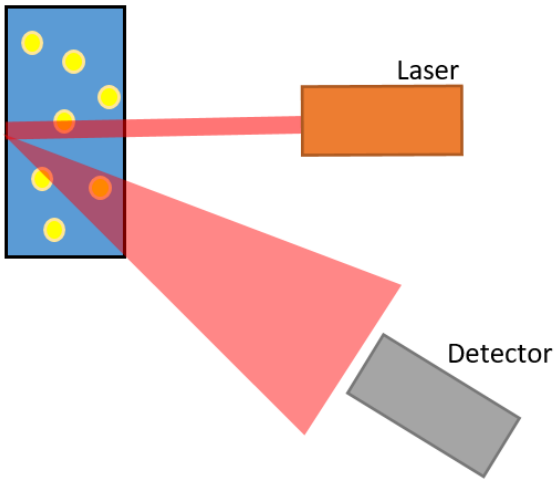

Figure 2.8: A schematic of the internal design of a standard light scattering system. A laser illuminates the suspended particles, which scatter light onto a detector. The speckle pattern of the light changes as the particles move as a result of constructive and destructive interference. As the particles move under Brownian motion, the changes in the light pattern can be back calculated to the particles size.

Since the DLS relies on the Stoke-Einstein equation to calculate the particle size, it is important that the particles in solution are only moving under the effects of

Brownian motion and not as a result of other forces (e.g. sedimentation). Care must also be taken, if distributions are likely to aggregate, since larger particles would dominate over smaller particles in the scattered signals.

2.10 Conclusion

This chapter sets a protocol for creating LISs and DMS surfaces in a way that gives reproducible samples. A deeper discussion on the best fabrication for LIS forms the basis for Chapter 3. Chapter 3 also discusses how the oil layer is characterised. Getting a well characterised oil layer is important to prevent any variation in oil layer thickness from changing measurement conditions. Evaporation on LIS surfaces is also discussed, and suggests that droplets placed on LIS surfaces cloak as a result of slower evaporation times on LIS. This will be important when looking at modelling CLBs in Chapters 5 and 6.

Chapter 3

A Model Liquid Infused Surface

Liquid-infused surfaces (LIS) are considered excellent candidates for controlling wetting on surfaces and preventing fouling. Within the literature, there are many different examples of LIS systems, fabricated using different materials and methods which can make comparison between studies difficult. In this chapter, the goal is to create a simple, reproducible model LIS that can be used to investigate the behaviour and properties of LIS. A model LIS is developed based on a strategy proposed by Orme et al[120]. Using nano-particles coated in perfluoroalkyltrichlorosilane groups and infused in silicon oil, a reliable LIS is created. These LIS are then comparatively characterised against non-infused surfaces with similar wetting properties.

Published as: Effect of Ageing on the Structure and Properties of Model Liquid-Infused Surfaces **Sarah J. Goodband**, Steven Armstrong, Halim Kusumaatmaja, and Kislon Voïtchovsky, *Langmuir* 2020, 36, 13, 3461–3470

3.1 Introduction

Liquid infused surfaces represent a family of functional surfaces inspired by the nepenthes pitcher plant whose porous outer surface is imbibed with a lubricating

liquid. This effectively replaces the plant's exposed outer surface with a fluid layer that creates a slippery surface able to shed liquid droplets and trap insects [58]. LIS are of considerable economical interest because they provide a non-toxic method for preventing the fouling and corrosion of surfaces. They do this by blocking the attachment of organisms or blocking direct interaction between the solid support and the outside environment [55,66]. Potential applications range from reducing the natural fouling of buildings, windows, transport vehicles and underwater structures (e.g. rigs, turbines, water treatment systems and power plants) to preventing biofilm formation on the surface of medical devices and implants [17,37–39]. Moreover, LIS have been shown to be anti-icing [62,80,136] and self-healing [55,90], exhibit low roll off angles [118] and drag reduction [137], present a high optical transparency [55,136] and may be used for fog-harvesting applications [138].

Regardless of intended application, all designs of LIS have to meet three main criteria: (1) the chemical affinity between the lubricating fluid and the solid should be higher than that between the ambient fluid and the solid, (2) the solid should preferably be roughened so as to increase the surface area for the adhesion of the lubricating fluid and its immobilization, and (3) the lubricating fluid and the ambient fluid must be largely immiscible [55,66]. Since the initial development of LIS [55,139–141], many different geometries and materials have been proposed for the porous substructure and lubricating fluid. These include the development of flexible surfaces from self-assembling polymers [42] or using novel ferro-fluids to infuse surfaces [142]. Experimental advances have further been complemented by theoretical studies to examine ideal geometries and the interplay of the infused liquid with supported liquid droplets moving across LIS [31,143,144].

Here, a simple model LIS is made with a commercially available spray of hydrophobized silica nanoparticles (GLACO^{TM}, see Methods Section) which creates a porous nano-layer that can be readily infused with silicone oil [119]. GLACO^{TM} -based LIS have been used to create inexpensive and facile LIS model systems [117,120,145], making them an ideal research platform for this study. There is however, no set protocol to create an optimal porous layer of hydrophobized nano-particles (NPs). It was therefore necessary to start by testing a variety of NPs-functionalized support with

a varying number of NP layers for oil infusion, investigating their roughness and the CA observed and how the oil layer changes over short (measurement) timescales. These measurements create a picture of how LIS evolve during fabrication, and quantify the changes associated with variations in the NP layers.

3.2 Structure of Nano-particle and Liquid Infused Surfaces

To begin, the structure and topography of typical NP surfaces and LIS are characterised. The surfaces are constructed of a hydrophobized silica nanoparticles (GLACO^{TM}) but the spray, although commercially available, is itself poorly characterised. This first section will therefore look at the size and distribution of nanoparticles as well as the effect of changing the number of NP layers.

Atomic Force Microscopy (AFM) images of a sample taken in ultrapure water, immediately after coating with a single layer of NPs (Figure 3.1a,b) reveal a full layer composed of NPs 20-50 nm in size, with an average root-mean-square (rms) roughness of 60 $\pm$ 5 nm.

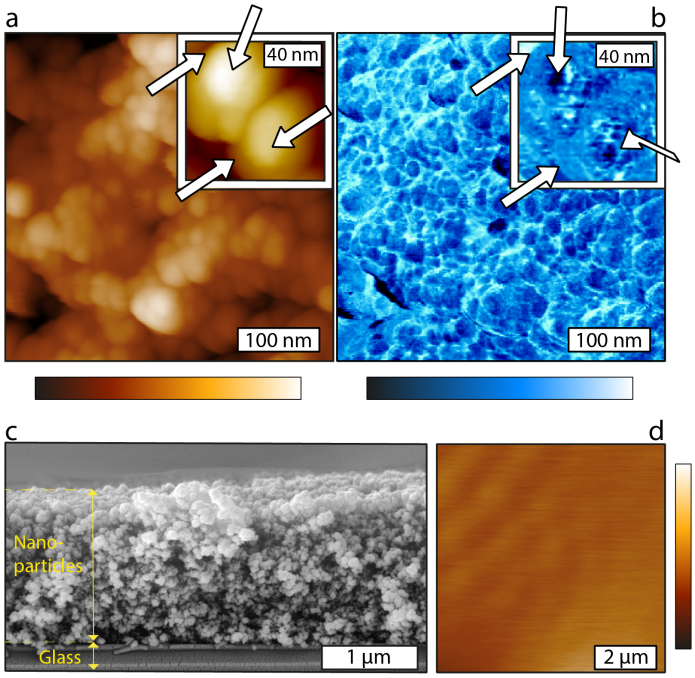

Figure 3.1: Characterization of the different surface functionalizations used to create the model LIS. AFM images of the NP-functionalized glass surface taken in ultrapure water (a,b) reveal a cohesive but rough NP layer with multiple NP clusters (a, topography). The associated phase information (b) exhibits some contrast between the harder silica core (darker) and the softer perfluoroalkyltrichlorosilane corona, which appear lighter and less well-defined (inset with arrows indicating the center and edge of two NPs). A scanning electron microscopy image of the section of the NP-functionalized glass taken after 5 NP layers were applied shows a homogeneous ~1.6 μm thick NP coating (c). After infusion with silicone oil, AFM imaging of the oil-water interface shows a smooth surface with occasional tip induced ripples (d). The colour scale bar represents a height variation of 140 nm (a), 60 nm (inset a), 500 nm (d) and phase variation of 30° (b) and 10° (inset b).

Interestingly, the associated phase image (Figure 3.1b) shows additional contrast over single NPs with the cores appearing darker than the hydrophobic shell (inset with arrows). The phase image is sensitive to the local viscoelastic properties of the surface[146–148], and able to distinguish between the stiffer silica cores and the softer perfluoroalkyltrichlorosilane shell when operated with a sufficiently large imaging amplitude[149]. Consistently, the cores appear well-defined, but the shells induce a fuzzy outer ring. The NPs are often clustered, which can lead to the solid centres appearing to overlap in some areas, with a range of particle sizes. This can also be

seen in the EM image taken on a glass substrate (Figure 3.1c). The layer is uniform and around 1.6 μm thick. The NPs layers were extensively characterized by AFM in air and water, demonstrating them to be consistent, stable, and well-attached (Figure 3.2).

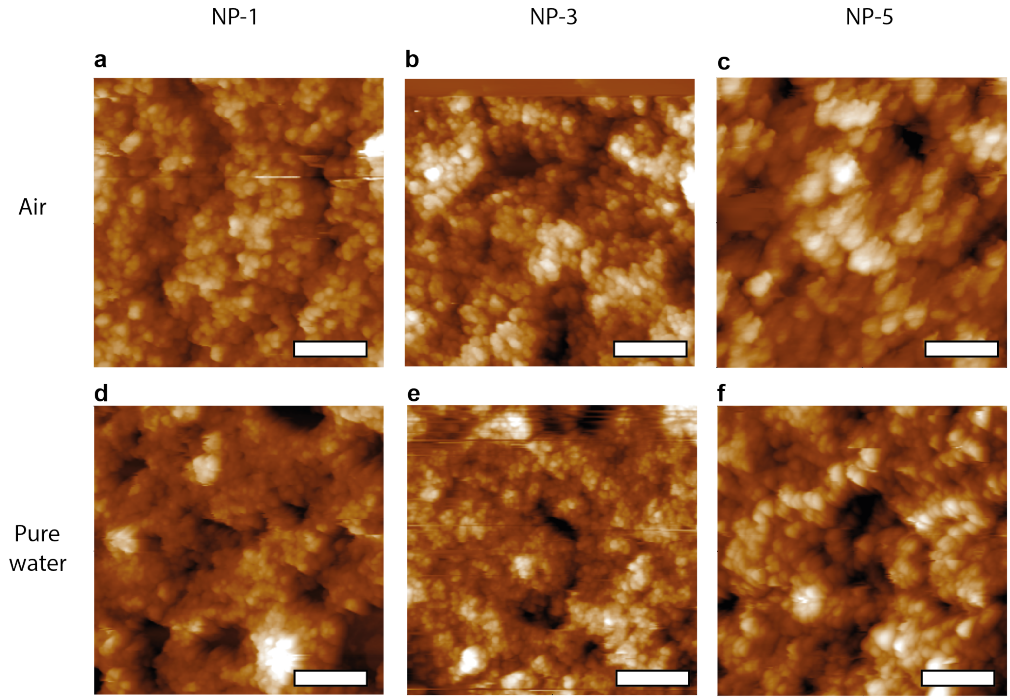

Figure 3.2: Characterization of the NP nanoporous surfaces in different imaging media. AFM images of the NP-functionalized glass surface taken in air (a-c) and ultrapure water (d-f) for different numbers of NPs layers. The images are very similar visually and exhibit decreasing roughness with added NPs layers (Figure 1). This suggests that once sprayed, the surface is fully coated; further layers only even out the surface by filling in possible gaps or troughs which in turn reduces the roughness. The scale bars represent 2 μm for all images. The colour scale bar is as in Figure 1 and represents a height variation of 530 nm (a), 340 nm (b), 281 nm (c), 570 nm (d), 389 nm (e) and 297 nm (f).

3.3 Roughness and Contact Angle Changes

Increasing the number of layers tends to decrease the surface roughness of the coating (Figure 3.3a, see also Figure 3.2). This is expected, as additional layers allow for

newly added particles to settle in more stable positions by filling up grooves in the previous coating layer. After 5 coats, the root mean squared roughness is comparable to the size of single NPs (∼40 nm), suggesting 5 layers to be close to the optimal limit for a smooth, regular coating (45 ± 5 nm). In order to create control surfaces,

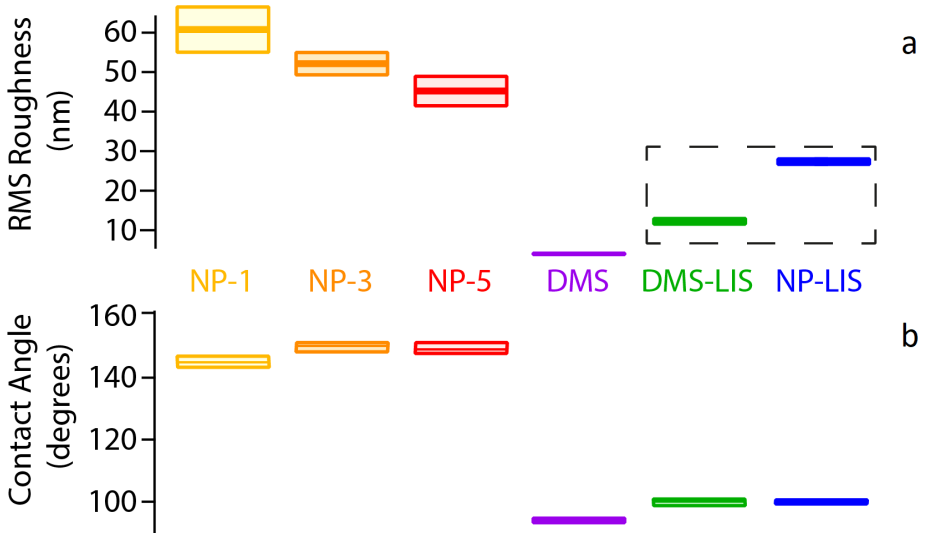

Figure 3.3: The surface roughness of the NP-functionalised glass tends to decrease with the number of NPs layers sprayed but remains significantly larger than the glass substrate directly coated with a single evaporated layer of DMS (a). The root mean squared roughness of each sample was systematically quantified by analysing 3 distinct regions of 2 μm x 2 μm in each case. All the measurements were taken in air except for the LIS. Roughness measurements conducted on the LISs are unreliable because of the probing technique inducing ripples in the oil layer. The corresponding roughness values should be considered as indicative only (dashed box). Static CA measurements conducted over all samples (b) yield a value of ∼150° for all the NP- functionalised surfaces (within experimental error), changing to 101 ± 1° after infusion with silicone oil. On DMS-functionalised surfaces, the CA changes from 95 ± 1° to 101 ± 1° upon infusion with silicone oil. The plotted CA values represent 20 or more independent measurements on a minimum of 2 samples for each set of surfaces. The error boxes (a,b) represent the standard error on the measurements. Samples were stored horizontally and measurements taken over the entire slide length.

glass slides coated with a single monolayer of DMS directly evaporated onto the surface are used, resulting in a significantly lower roughness of 9 ± 1 nm when imaged under identical conditions (Figure 3.3a). The DMS-functionalized surfaces

can be considered flat and hydrophobic, and hence serve as a reference to single out the effect of porosity on oil retention when compared to a NP-functionalized surface. To create a full LIS, the NP- and DMS-functionalized glass slides were infused with silicone oil (see the Experimental Methods section). AFM imaging of the oil-water interface atop an infused 5-layer NPs sample reveals a smooth regular surface with occasional ripples, presumably due to the AFM tip probing the oil-water interface and causing small disturbances (Figure 3.1d). Estimates of the average oil layer thickness based on the weight of the samples after infusion yields values between 6 and 8 μm. These values are typical, but can vary, depending on the oil temperature during spin coating, and the environmental conditions in the laboratory.

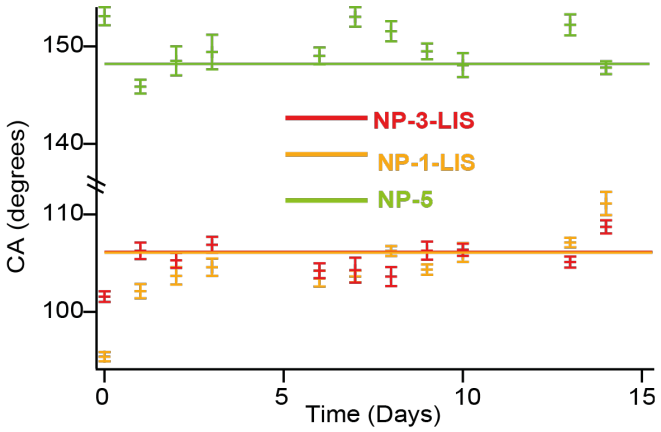

Figure 3.4: Comparison of the CA evolution over a 15 days period for NP-5, NP-1-LIS and NP-3-LIS. No degradation of the nanoparticle surface is noticeable in air over the measured timeframe (NP-5). The CA measured on the LIS with 1 or 3 functionalized NP layers remain constant over time, suggesting that even the thinnest porous layer is sufficient to maintain the oil layer thickness required to create a LIS. The plotted data represents 5 measurements per set with the error bars representing the standard error on the 5 measurements. The solid color lines serve as eye guides.

Static CA measurements, taken across the different surfaces, show the biggest difference between the infused and the non-infused surfaces for any type of functionalisation (Figure 3.3b). For NP-functionalized surfaces, infusion with silicone oil reduces the CA from $\sim$150° to $\sim$101°. Within the experimental error, no differences can be observed between NP-functionalised surfaces with different numbers of layers,

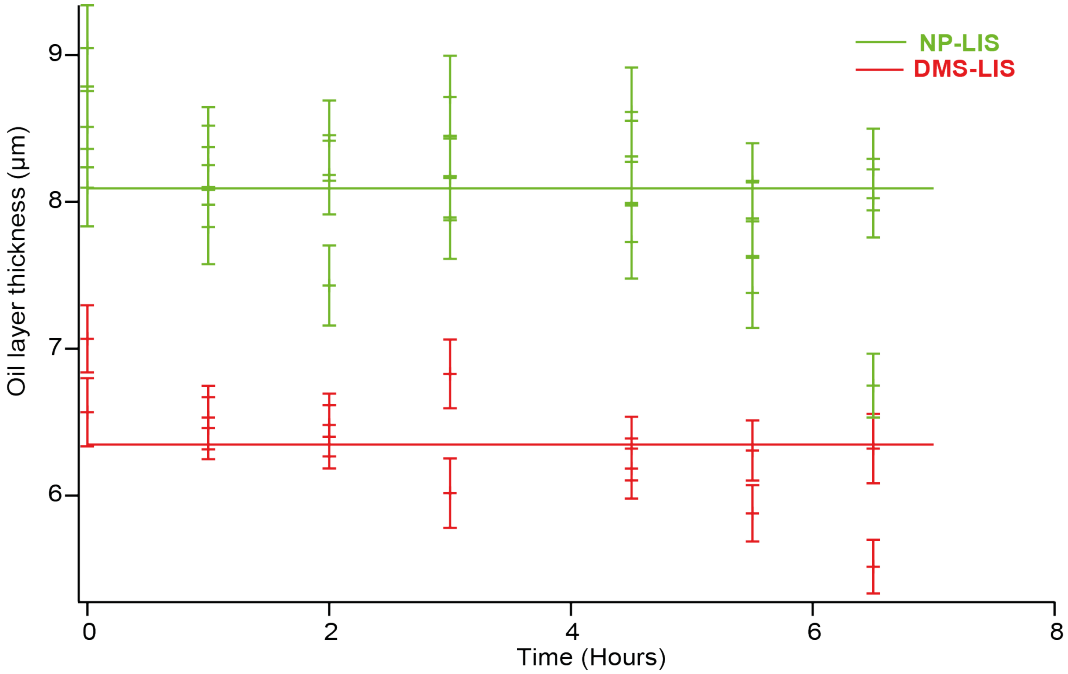

Figure 3.5: Oil layer thickness evolution for NP-LIS and DMS-LIS on short timescales. Oil loss from the LIS can be considered negligible on short timescales in the absence of external perturbations. The measurement variability likely results from temperature and humidity changes. Each data point represents the average of 3 measurements and its error is given by the standard error over the 3 measurements. The solid lines serve as eye guides.

which remain stable over days (Figure 3.4). This is not surprising, given it is expected that the oil to fully cover the surface corrugations. For DMS-functionalized surfaces, the CA changes from ∼95° to ∼101° upon silicone oil infusion, with an initial measured oil layer thickness comparable to that of the NP-functionalised surfaces (Figure 3.5). Overall, the CA values are identical for all fresh LISs within the experimental error, reflecting the fact that the CA is then entirely determined by the oil-water interfaces, with no direct effect on the functionalisation. The measured values are also in agreement with the predictions based on a liquid-equivalent of Young's CA equation[9]:

$$\theta = cos^{-1}\frac{\sigma_{og} - \sigma_{ol}}{\sigma_{lg}^{eff}} = 104 \pm 2°, \tag{3.1}$$

where σ_{og}, σ_{ol} represent the interfacial energies between oil and air, and oil and

water respectively, and σ_{lg}^{eff} the effective interfacial energy between water and air. For simplicity, it is assumed that $\sigma_{lg}^{eff} = \sigma_{og} + \sigma_{ol}$, since the water droplet is expected to be cloaked by the silicone oil. It should be noted that CA values can exhibit changes of several degrees when measured multiple times over days due to changes in the ambient laboratory relative humidity and temperature. The error associated with the above derivation takes into account such changes which will be discussed later in Chapter 4.

3.4 Discussion and Conclusion

In this chapter, the NP and LIS surfaces produced were characterised and a protocol for creating the optimal model surface was determined. The surfaces created are compared to a smooth hydrophobised control surface (DMS-functionlised). The choice of materials for fabrication and the ambient fluid for testing were selected to meet the fabrication criteria for LIS surfaces (as mentioned previously but recapped here): (1) the chemical affinity between the lubricating fluid and the solid should be higher than that between the ambient fluid and the solid, (2) the solid should preferably be roughened so as to increase the surface area for the adhesion of the lubricating fluid and its immobilization, and (3) the lubricating fluid and the ambient fluid must be largely immiscible[55,66]. The choice of silicone oil and a surface made from hydrophobised silicone beads allows the first criterion to be met when using water or glycerol droplets as the ambient fluid. The hydrophobised NP create a roughened surface when applied meeting criterion 2. Water/Glycerol solutions and silicone oil are immiscible, meeting criterion 3.

The NPs used for surface fabrication are hydrophobised silica beads with an approximate diameter of 40 nm. A surface that has 5 layers of NPs is considered optimum. This creates a porous network of approximately 1.6 μm, which can be infused with a reservoir of oil. The surface roughness of the 5 layers of NPs is around 45 $\pm$ 5 nm. When considering our NPs are around 40 nm, this suggests

that this is the optimal number of layers for a smooth and even coating. This is in comparison to the DMS-functionlised surface whose roughness is around 9 ± 1 nm. The roughness shall become important when considering oil retention in ageing experiments in Chapter 4.

The CA measured on the NP and DMS-functionlised surfaces changes upon infusion with oil. For NP-LIS this reduces the CA from ∼150° to ∼101° and the DMS-functionlised surfaces increases from ∼95° to ∼101°. Since both surfaces are exposing the ambient fluid to silicone oil of a similar thickness, it is expected that the CAs should be the same for both surfaces. The measured CAs are in agreement with predictions based on the Young equation which predict the CA to be ∼104° ± 2°. Oil loss is minimal over the timescales of these characterisation experiments for both the NP- and DMS functionlised surfaces.

3.5 Experimental Methods in Chapter 3

3.5.1 Practical AFM imaging

In order to fit into the AFM chamber, glass slides were cut into small (<10 mm) pieces and epoxy-glued to steel disks (12 mm, SPI Supplies, West Chester, USA). AFM imaging was carried out in amplitude-modulation using a commercial Cypher ES equipped with photothermal excitation of the cantilever (Asylum Research, Oxford Instruments, Santa Barbara CA, USA). Imaging was carried out in air or in the aqueous solutions using Arrow-UFHAuD-10 cantilevers (nominal stiffness of 1 N/m, Nanoworld, Neuchatel, Switzerland). Image optimization was achieved following established protocols[146].

3.5.2 Practical Contact Angle Imaging

All contact angle (CA) images were captured using a portable digital microscope (Dino-lite Edge) and analyzed using the ImageJ freeware, in particular FIJI plugins Dropsnake[127,128] (100 μ l drops) or ContactAngle41 (10-20 μl drops). Static CA measurements were conducted with 100 μl droplets.

3.5.3 Characterization of the Infused Oil Layer Thickness

The NP-coated slides were weighed before and after spin coating with silicone oil. Knowing the oil density and the area of the slide, a thickness for the oil film could be derived. This approach is convenient to track oil losses and rapidly estimate changes in the infused layer thickness. However, it rests on the assumption of a uniform, homogenous oil film and neglects any of the oil contained within the rough porous NP layer. These assumptions are justified considering the order of magnitude in thickness difference between the oil and porous layers, at least for the fresh samples. Values obtained are in the range of 6-8 μm.

Chapter 4

Ageing Liquid Infused Surfaces

Liquid-infused surfaces (LISs) exhibit unique properties that make them ideal candidates for a wide range of applications, from antifouling and anti-icing coatings to self-healing surfaces and controlled wetting. However, when exposed to realistic environmental conditions, LISs tend to age and progressively lose their desirable properties, potentially compromising their application. The associated ageing mechanisms are still poorly understood, and results reflecting real-life applications are scarce. Here, the ageing of a model LIS composed of glass surfaces functionalized with hydrophobic nanoparticles and infused with silicone oil (as described in Chapter 3) is tracked. The LISs are fully submerged in aqueous solutions and exposed to acoustic pressure waves for set time intervals. The ageing is monitored by periodic measurements of the LISs wetting properties. The changes to the LIS's nanoscale structure are also tracked. It is found that the LISs rapidly lose their slippery properties because of a combination of oil loss, smoothing of the nanoporous functional layer, and substrate degradation when directly exposed to the solution. The oil loss is consistent with water microdroplets entering the oil layer and displacing oil away from the surface. These mechanisms are general and could play a role in the ageing of most LISs.

Published as: Effect of Ageing on the Structure and Properties of Model Liquid-Infused Surfaces **Sarah J. Goodband**, Steven Armstrong, Halim Kusumaatmaja,

and Kislon Voïtchovsky, *Langmuir* 2020, 36, 13, 3461–3470

4.1 Introduction

Ageing is experienced by all things - even humans cannot escape the passage of time! LISs are no different. Yet, in the current literature while there is abundant research investigating the design of LISs, their ageing and wear is often overlooked despite it being considered one of the biggest problems facing self-cleaning surfaces [79]. When available, studies typically examine LISs ageing during static storage in air or in solution at room temperature [80], or under steady external perturbations on a freshly made LIS [66,81–83]. Durability is assessed in terms of substrate recovery after damage incidents (such as incision or impact in the infused layer) [17,37,84], oil loss, and the ageing of surfaces under soaking conditions. Generally, LISs retain their slippery properties [21,62,85] provided the oil layer is not depleted, and periodic reimmersion in oil has been shown to allow most LISs to regain their self-healing properties and high droplet mobility [86]. Indeed, in nature, the nepenthes pitcher plant exhibits a unique system of continuous liquid transport, which is used to allow the surface to retain its slippery properties [150]. Synthetic mimics have also been designed to replicate this spreading behaviour [151–153].This suggests the integrity of the infused oil layer to be the single most important factor; upon oil depletion, LISs progressively lose their anti-fouling properties and biomaterial is able to attach [85]. Several mechanisms may be responsible for the oil loss, including exposure to shear flows [81–83], failure under gravity [81], and aqueous droplet cloaking by the oil resulting in the LIS material being carried away [87].

Here, the ageing of a model LIS is investigated when exposed to an environment that aims to mimic real-life applications such as waves in the sea, rain falling, or localized impacts. This is achieved by immersing our model LIS in aqueous solutions and exposing them to ultrasonic pressure waves. The use of well-defined ultrasonic waves ensures a reproducible but accelerated LIS ageing compared to

ambient laboratory conditions. This strategy enables us to identify some of the mechanisms responsible for the oil loss and degradation of the porous layer, including the impact of dissolved salt ions in the aqueous solution that are in contact with the LIS. Significantly, the functional evolution of the ageing LIS is tracked and linked to nanoscale changes that occur within the different LIS components. This is achieved by combining macroscopic contact angle (CA) and CA hysteresis (CAH) measurements with atomic force microscopy (AFM) of the porous and liquid-infused surface. This approach allows for a systematic study into the effects of ageing across different length scales.

4.2 Static Ageing

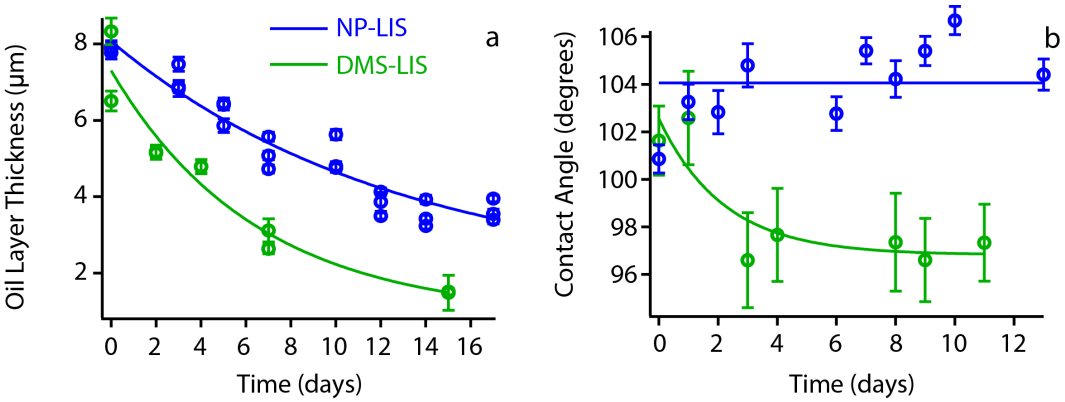

Figure 4.1: Oil retention ability and static contact angle evolution of the DMS-LIS and 5-layer NP-LIS in air under ambient laboratory conditions. The thickness of the silicone oil layer decreases in time because of the losses to the environment (a). The loss is significantly more pronounced for the DMS-functionalized LIS, which depletes to below an oil layer thickness of 2 μm within 15 days. Static CA measurements (b) show no evolution over the NP-functionalized LIS, but a progressive return to oil-free values for the DMS-functionalized LIS. This is consistent with the almost complete oil depletion measured in (a). The two data sets are independent and were taken on different samples but placed together for comparison. Each point represents an average of 3 measurements with its standard error. The solid lines in (a,b) serve as eye guides.

The first experiments determine the basic stability of our model LIS. The effect of surface porosity on oil retention was examined as the sample aged unperturbed in

air. This was done by comparing the ability of a 5-layer nano-particle coated liquid infused surface (NP-LIS) and the control Dichlorodimethylsilane coated surface(DMS-LIS) (cf. Chapter 3) to retain the infused silicone oil, evaluated by periodic weighing and CA measurements. The results are shown in Figure 4.1.

Static CA measurements on the freshly oil-infused LIS give a similar CA consistent with the results in Chapter 3. As the LIS ages, oil is lost from both the porous and nonporous surface, but the oil loss occurs more rapidly from the nonporous surface, with the initial oil layer thickness halving over ∼4 days. This rapid loss correlates to a change in CA for the DMS-LIS, a behaviour not observed for the NP-functionalized LIS, even after partial oil loss. For the NP-LIS, the CA remains constant at ∼104°. The apparent insensitivity of the CA on the oil layer thickness for the NP-based LIS has been demonstrated in previous computer simulation studies. These predict a negligible change in the CA for relatively large water droplets (>2-3 mm as used here) on thin oil films upon changes in the film thickness[31]. This is because the typical size ratio between the oil film and the droplet is very small (less than 0.01). It should be noted that this is not true for smaller aqueous droplets whose oil ridge becomes comparable to the droplet size, resulting in an apparent CA that noticeably depends on the oil layer thickness[154]. The main source of error in the experimental measurements of the CA comes from fluctuations in the laboratory's temperature T (16 °C< T <25 °C) and relative humidity RH (50% < RH < 90%), both of which are not controlled throughout the experiments. The associated variations in the CA over the same sample are ∼2% because of temperature variations and ∼2% because of RH variations (See Chapter 2, CA characterisation section). These uncertainties are in agreement with previous reports indicating CA variations of up to 15%[155]. Changes in RH would, in principle, also affect the droplet evaporation rate, but given the short experimental timescales and the relatively large droplets this can be neglected here. Oil loss over the course of hours can be considered negligible, as can be the impact of gravity due to vertical storage of the LIS (see Figures 3.5 and 4.2, respectively). Overall, the results presented in Chapter 3 and Figure 4.1 further confirm the suitability of the 5-layer NP-LIS as a model system to investigate the ageing of the LIS un-

der external perturbations. The 5-layer NP-LIS will hence be used systematically hereafter unless otherwise specified.

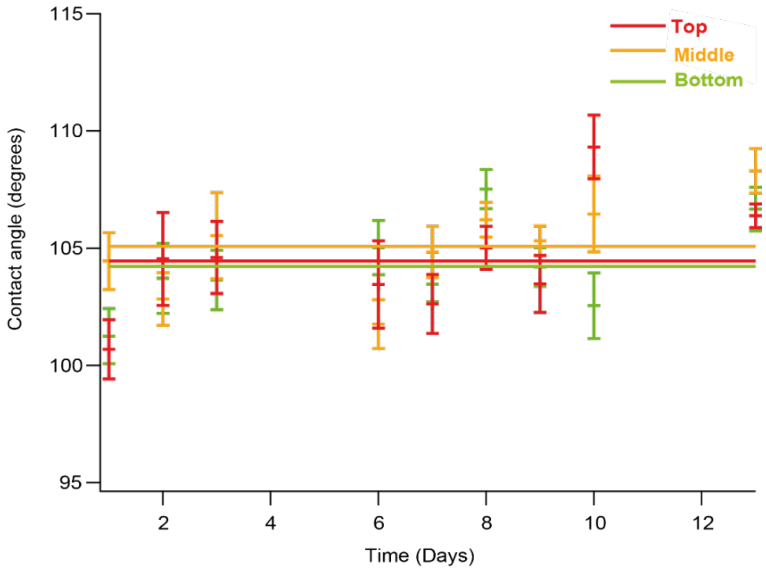

Figure 4.2: Impact of gravity on the CA evolution of NP-LIS during storage. The surfaces were stored vertically and the CA measured daily taken at the top, middle and bottom of the slide with respect to the vertical storage. Within errors the CA was not found to change over the measured time period. Changes in humidity and temperature may result in variations in CA of up to 6 %, explaining the fluctuations that can be seen between daily measurements. Overall the data suggest a sufficiently thick oil layer over the entire surface. The data represents 5 measurements on one sample per set with the errors representing the standard error on the data.

4.3 Accelerated Ageing

To assess the impact of ageing in more realistic conditions, the 5-layer NP-LIS samples were immersed in aqueous solutions containing either ultrapure water or a 600 mM NaCl (saline) solution and exposed to pressure waves by ultrasonication. The choice of the saline solution is to mimic conditions in a number of LIS applications, such as for medical devices, transport vehicles and underwater structures. The ageing process used here is harsher than most natural conditions (Table 4.1) and can be seen as accelerated ageing. Section 4.3.1 discusses how estimates were made of different natural phenomenon compared to the accelerated ageing method

(bath sonicator). Then the sample ageing and ageing mechanics are discussed in Sections 4.3.2 and 4.3.3.

Process	**Energy [Wm^{-2}]**
Ultrasonic waves (bath sonicator)	400-1200
Ocean wave	100 - 6000 [156,157]
Rain fall (vertically, per drop)	0.6-12 [158]
Rain fall (on a windscreen@100 km/h, per drop)	120-620

Table 4.1: Comparison of the mechanical energy experienced by surfaces in various natural and experimental situations. The typical power per surface area associated with natural processes such as the impact of an ocean wave or a raindrop. The values are compared with that calculated for the ultrasonic bath used for accelerated ageing of the LIS in this study. Detailed calculations for the different estimates can be found in Section 4.3.1

4.3.1 Estimation of the Energy Associated with Real-life Phenomena

The Power of Ocean Waves

Depending on local weather conditions, water depth and a number of other factors, ocean waves can generate vast sums of energy. Here the simplest case of deep water waves is considered. Their power can be expressed by:

$$P_{density} = \frac{\rho_{water} g H^2}{8\lambda}, \tag{4.1}$$

where $P_{density}$ is the wave power per m^2, ρ_{water} is the density of water, g is gravity, H is the wave height and λ is the wave period. Taking ρ_{water} = 1000 kgm^{-3} and g = 9.81 ms^{-2} , and estimating the wave height (H) varies between 1 and 7 meters

and the wave period is ∼10 s, $P_{density}$ values between 100 and 6000 Wm^{-2} are obtained.

Raindrop

Here, the power per unit area of typical rainfall is considered. For simplicity, only two types of rain are considered here (light and heavy rain), as defined by Guigon et al[158]. Taking their assumptions for a characteristic raindrop in a light rain shower (1 mm radius, velocity 2.8 m/s and available energy 2 μJ) the power per unit area of the rain is calculated to be 0.6 W/m^2. In heavy rain it is assumed that a characteristic raindrop has a radius of 5 mm, a speed of 5.7 m/s and available energy of around 1 mJ[158]. This gives a power per m^2 of the rain to be 12.7 W/m^2.

Raindrop on Vehicle Windscreen

For the calculation of the power of a raindrop when it hits a car the same assumptions as above are made; that only two types of rain exist. It is also assumed that the raindrop is falling vertically, and that the car hits the drop at 100 km/h (approximately 27.8 m/s). For light rain with the same features as mentioned above, the available energy of the droplet is calculated to be 0.3 mJ. This gives a power per unit area of 122 W/m^2. In heavy rain conditions, the rain drop would have an available energy of 0.048 J and hence a power per unit area of 613 W/m^2

Characterising the Bath Sonicator

An ultrasonic bath is used to accelerate the ageing of the LIS samples. A schematic of the setup is shown in Figure 4.3a. Three piezo-transducers are coupled to the bottom of a cuboid metallic tank filled with water. As the transducers vibrate, they emit ultrasonic waves that travel through the bottom of the tank, resulting in pressure waves propagating into the bath.

To estimate the power reaching the sample, a liquid displacement sensor (RS PRO

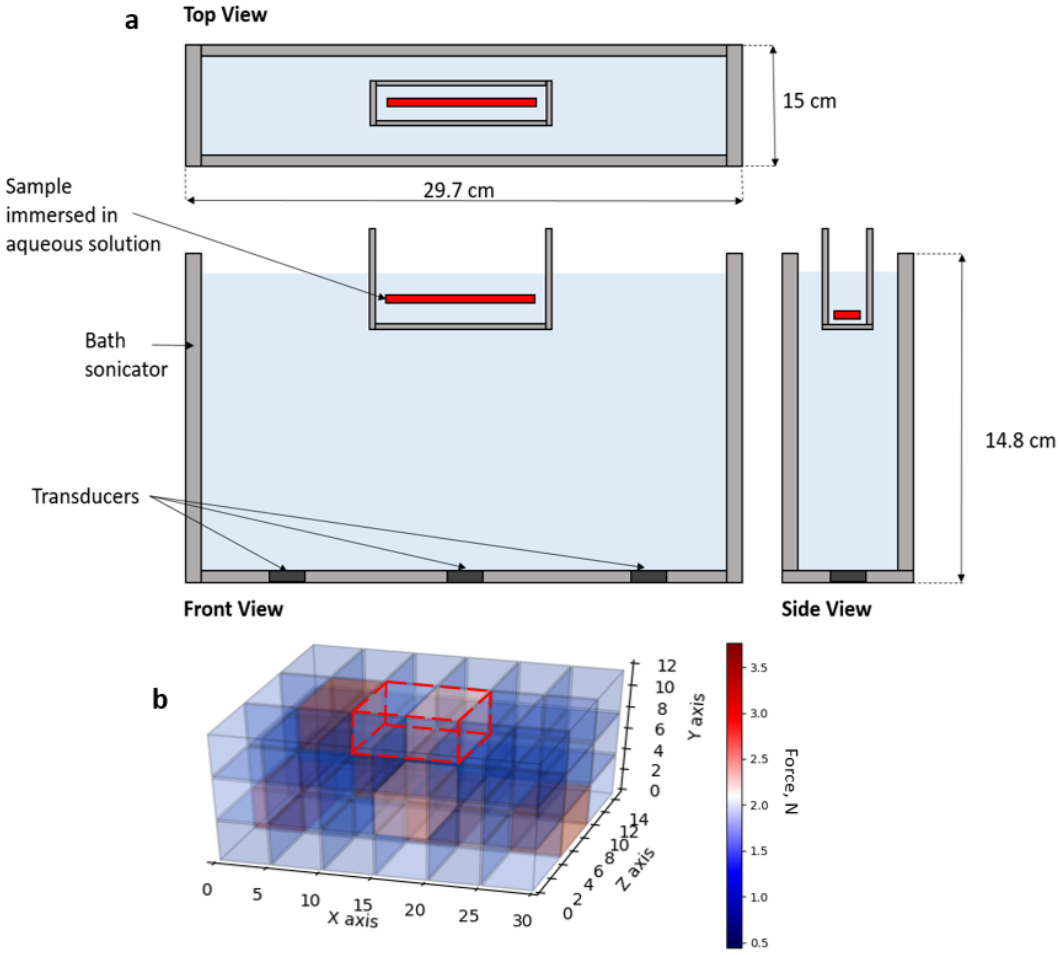

Figure 4.3: Schematics of the bath ultrasonicator used for the study. (a)Three piezo-transducers are coupled at the bottom of the tank but are not directly in contact with the bath's liquid. The transducers emit ultrasonic (45 kHz) pressure waves that propagate through the bath and to the sample which sits in the middle of the tank, immersed in an aqueous solution. Due to constructive/destructive interference of the emitted waves and reflections on the tank's sides, the power density of the ultrasonic pressure waves varies across the tank (b). Using a bespoke sensor, the characteristics of the ultrasonic waves were hence quantified at the location of the sample.

Vibration Sensor (model 285-784), RS Components, Northants, NN17 9RS, UK) was used to quantify the relative magnitude of the liquid displacement across the bath. Practically, the whole bath volume was divided into 54 identical size voxels (as shown in Figure 4.3b) and an AC measurement of the displacement taken in each voxel. To obtain the ultrasonic power in each voxel, two assumptions are made:

(i) all the power supplied to the transducers is converted into the periodic liquid displacement measured, and (ii) the ultrasonication energy at a given location varies with the square of the measured displacement. The first assumption is reasonable since no temperature variation of the liquid was recorded over the timescale of the measurement. The second assumption is standard for any oscillatory phenomenon. It can be therefore found:

$$P = k \sum_i D_i^2, \tag{4.2}$$

where P is the total power supplied to the bath, k is a proportionality constant and D_i is the average oscillatory displacement measured for voxel i. It should be noted that the displacement is measured in the form of a voltage, but this does not change the reasoning since the voltage is directly proportional to the real displacement. From the constant k, the distribution of power can then be determined across the bath and in particular for the voxel where the sample is located. Dividing the power attributed to this voxel by its area parallel to the ultrasound source, a power per unit area in the order of 800 Wm^{-2} was found. Given the approximations and assumptions made, an error of 50% on this value is expected. Calibrating the displacement sensor for its stiffness, it was also possible to deduce the force F_d exerted by the moving liquid on the sensor. Then, knowing the geometry and hence the drag factor of the sensor, F_d could be used to calculate the average velocity, v, of the moving bath liquid using the drag equation:

$$F_d = \frac{1}{2} \rho v A C_d, \tag{4.3}$$

where ρ is the mass density, A is the reference area of the sensor and C_d is the drag coefficient, taken here to be 1. Taking ρ = 997 kg m^{-2} and A = 1.5 mm x 15 mm, the velocity is found to be approximately 8 ms^{-1}. While only an estimate, this value seems reasonable for an ultrasonic bath. Generally, the above calculations are estimates that rely on several simplifications and assumptions. Uncontrolled effects such as possible cavitation are not considered. Therefore, the values derived are taken as indicators of the order of magnitude at play.

4.3.2 Sample Ageing

In both the pure water and saline solution, the static contact angle remains, on average, constant over time (box plot in Fig. 4.4a,b), with no observable trend within error (standard deviation of the measurements). This is despite an exponential decay in the oil layer's thickness (Fig. 4.4c). Both solutions exhibit a large spread of measured CA values with a rapid increase past 8 minutes of sonication. This transition approximately coincides with the point where the oil layer thickness starts to plateau after an initial rapid decrease (Fig. 3c). This behaviour suggests the appearance of defects in the oil layer, with possible localized exposure of the NP-functionalized surface underneath. This exposure is localized enough not to affect the CA value on average, but sufficient to induce droplet pinning and a higher CA variability. To better quantify this effect and confirm its origins, contact angle hysteresis (CAH) measurements were conducted on a new set of ageing samples, simultaneously tracking the oil layer thickness (Fig. 4.5). While the strategy allows for less measurement points than in Figure 4.4, it provides a more complete picture of the ageing process.

The CAH values in both solutions are initially low, starting with $2°$ and increasing to $6°$ with a wider spread after 4 minutes of sonication (Fig. 4.5a,d). The hysteresis spread rapidly increases up to values exceeding $30°$ for times exceeding 12 minutes. This variability can be quantified by an increase in the CAH standard deviation (Fig. 4.5b,e) and directly visualized by comparing representative images of the aqueous droplets sitting on the LIS during ageing (Fig. 4.5c,f). Little variation is seen in early droplets, whereas the droplets on aged LIS exhibit pinning and significant variations between droplets, consistent with the appearance of multiple localized defects in the oil layer. The details of these local surface changes are not trivial. Simple oil depletion would be consistent with the increased CA variability and CAH values, but directly exposing hydrophobic NPs should increase the CA upon ageing. This is clearly not the case (Fig. 4.4) pointing to localized structural and chemical changes to the porous NPs structure.

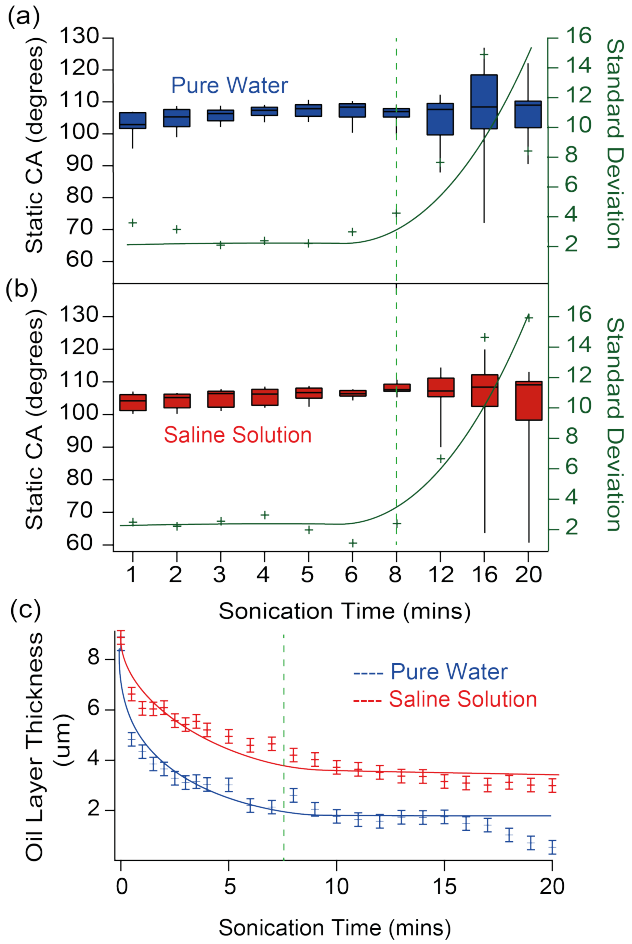

Figure 4.4: Accelerated ageing of the model LIS under ultrasonication in ultrapure water and in a 600 mM NaCl (saline) solution. For both ultrapure water (a) and saline solution (b), the evolution of the CAH is presented in box and whisker plots (black) showing the median value and the upper and lower quartiles. The standard deviation (red) is shown as a function of sonication time with a fitted curve serving as an eye guide. In both liquids, the average CA remains unchanged within error as the infused oil layer thickness decreases (c), but the spread of the CA values increases rapidly past 8 min of sonication (green dashed line). This indicates significant fluctuations arising with time, presumably due to pinning effects as the oil layer progressively becomes patchy. The oil layer thickness (c) was deduced from weight measurements taken every 30s ($<$ 5mins) or every 60s ($>$ 5 mins). Separate samples were used for the CAH data (a, b) and the weight measurements in (c) to avoid the extended time periods necessary to take CAH hysteresis measurements between weight measurements. The data represents 20 CA measurements taken over 5 different locations for each sample and at each time step for the box plots (a, b).

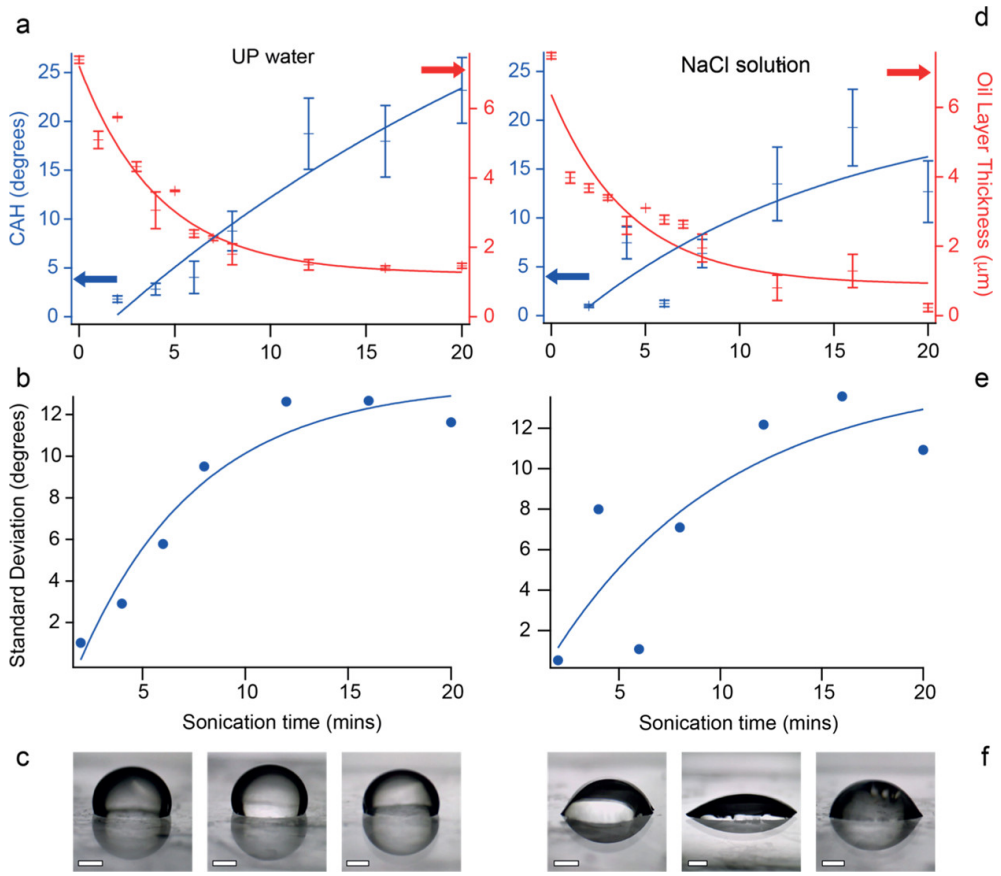

Figure 4.5: Changes in CAH upon accelerated ageing of LIS in ultrapure water and a 600 mM NaCl solution. The evolution of the CAH is shown in both solutions (a, d) with an exponential fit (blue line) and the errors bars representing the data standard error. The infused oil layer thickness is superimposed (red curve, exponential fit) for comparison. The standard deviation of the CAH (b, e) can be seen to increase as the sonication time increases, supporting the hypothesis of localized defects forming in the infused layer. Images (c,f) show representative droplets at early (1 min) and late (8 min) sonication times in both media. Each CAH data point in (a,d) represents 12 measurements taken over 4 samples for each solution. Arrows indicate the direction of the reference axis label. The scale bars in images (c,f) represent 1 mm.

4.3.3 Ageing Mechanisms

Examining the nanoscale details of the ageing porous NPs structure indicate that several related processes are simultaneously operating during the depletion of the initially thick oil layer (Fig. 4.6). Firstly, the oil removal partly exposes the NPs

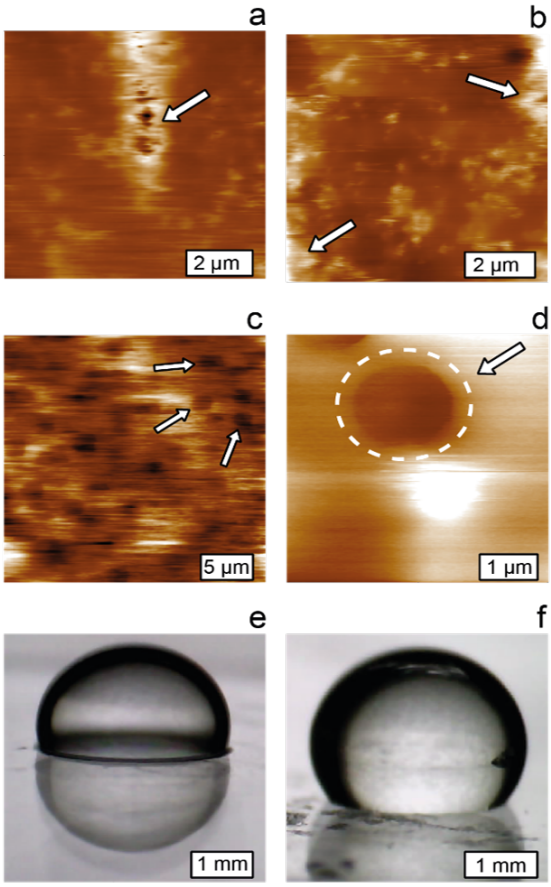

Figure 4.6: Images of the oil-aqueous solution interface during accelerated ageing. AFM images reveal a progressive depletion of the infused oil-layer, exposing some surface features of the NPs nanoporous layer (a). More features are visible at longer sonication time (b), consistent with the oil layer shedding to reveal the surface underneath with small nano-ridges emerging from the depleted oil layer (arrows in a-b). The main mechanism for oil removal (c) is the replacement of oil microdroplet by aqueous droplets, inducing characteristic circular depleted regions in the oil layer (arrows). A magnified view of one such circular depletion is highlighted by a white dashed circle and arrow (d). The horizontal streaks in (c-d) confirm that the AFM tip is still scanning a fluid and mobile layer. Optical images of droplets on fresh (e) samples show an oil ridge at the drop edge. When the layer is sufficiently depleted (f), the oil ridge is no longer visible. The color scale is as for Fig. 3.1, with a maximum height variation of 124 nm (a), 242 nm (b), 129 nm (c) and 90 nm (d).

structures underneath enabling them to become visible by AFM (Fig. 4.6a-b). Secondly, the exposed NPs-functionalized regions degrade in time, as will be shown

later in Fig. 4.7 (It is worth noting that these exposed features in general have distinct wetting properties compared to surface regions which are never infused). Thirdly, water microdroplets get trapped in the oil layer (Fig. 4.6c-d), locally changing the layer's wetting properties, and paving the way for degradation of the NP-functionalized surface. This entrapment of the aqueous solution can be directly visualized at the nanoscale by AFM imaging, with aqueous microdroplets appearing as circular depressions in the oil-water interface (arrows in Fig 4.6c-d). The entrapment results in oil droplets being pinched off the surface, and previously submerged microdroplets leaving the oil layer cloaked. As a result, it is impossible to remove the sonicated LIS from its aqueous bath without losing some of the infused oil layer.

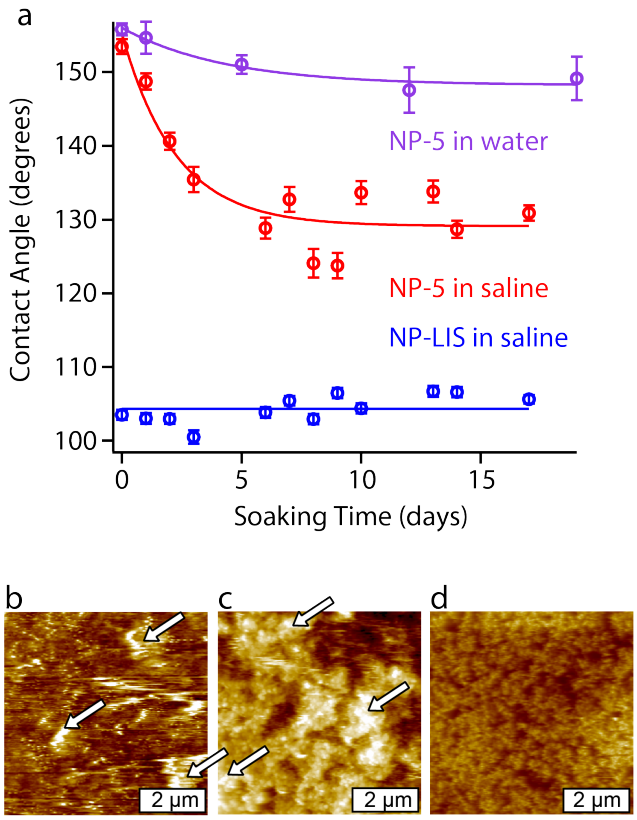

Figure 4.7: Impact of NP-5 soaking in an aqueous solution on the integrity and properties of the NPs layer. Over 20 days, the static CA decreases significantly on the nanoporous NP-5 surfaces in saline solution while no evolution is seen for the LIS (a). AFM images taken on the NP-5 surface at day 5 in pure water (b), the NP-5 surface at day 2 in saline solution (c), and the LIS surface at day 14 in the saline solution (d), reveal some key differences in ageing. Permanent surface degradation is evident for the non-infused surfaces (b, c) where large clusters are present (arrows) and more pronounced in the saline solution. Increased roughness is also visible on the LIS but much less pronounced, and the characteristic scanning streaks confirms the presence of a mobile oil layer. The color scale in all AFM images represents a height variation of 400 nm.

This effect could be confirmed by assessing the stability of pure water and saline emulsion formed in silicone oil by sonication (Fig. 4.8). Over a timescale of hours, the microdroplets can be seen, on average, to increase in size with the saline solution exhibiting a slightly higher stability. This is likely to be due to the fact that saline droplets have a higher colloidal stability than their pure water counterpart where only hydroxyl ions are able to stabilize the droplet [159]. When NaCl is

added at high molarity, the co-ions preferentially sit at the oil-water interface next to the hydroxyl ions, effectively creating an ionic surfactant layer which renders the droplet positively charged and more stable against coalescence [160].

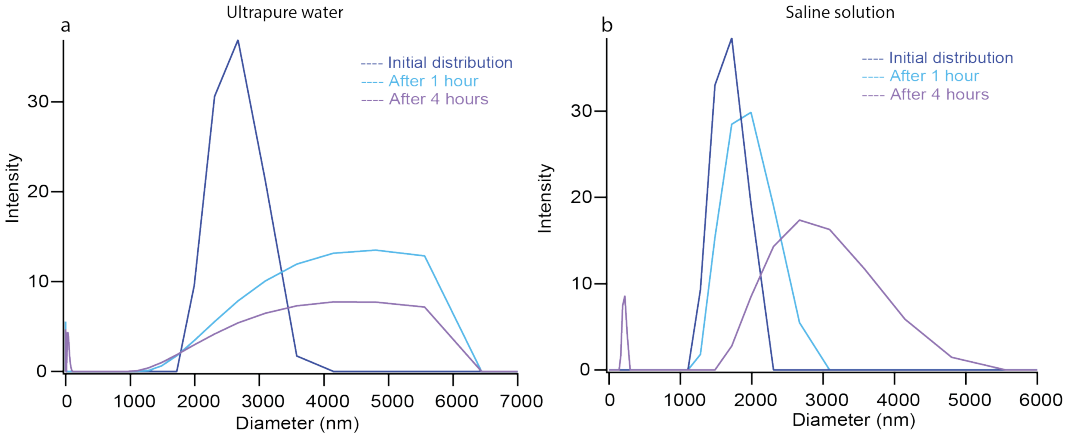

Figure 4.8: Stability of water-in-silicone oil emulsion for different aqueous solutions. The stability of the emulsion was determined by periodically measuring the droplet size distribution at different time intervals, after the initial emulsion creation by sonication. The water-in-oil emulsion droplets progressively coalesce over time, but the coalescence is more rapid in ultrapure water (a) than in the 0.6 M saline solution (b). This is visible by the fact that the peaks broaden faster in pure water than in the saline solution. The data was obtained using dynamic light scattering techniques (ZetaSizer-Nano).

The porous NPs-layer substrate used for the LIS ages too as a result of sonication. This occurs not only as a direct, mechanical result of the sonication waves, but also by increased exposure to the aqueous solution [21], an effect exacerbated in the presence of more stable saline droplets. Control sonication experiments carried out on NPs-functionalized surfaces without any oil present show that direct mechanical effects mainly decrease the porous layer's roughness from ∼60 nm to 35-40 nm (Fig 4.9). This is likely to be due to the removal of loose or protruding particles, leaving a more uniform surface. As can be expected, the wetting properties of the surface change with the roughness [14,15] (Fig 4.7a; NP-5 in water). Superhydrophobic surfaces have poor underwater stability due to the difficulty in retaining air pockets [21,161]. Here, sonication could force water against the surface, displacing any residual air pockets. However, the surface itself remains fully and

uniformly covered with the NPs well attached (Fig. 4.9). This suggests a limited impact of the pressure waves on the integrity of the nanoporous surface. Instead, damage to the nanoporous layer mainly results from prolonged exposure to the saline solution, which can cause the NPs to detach or become loose.

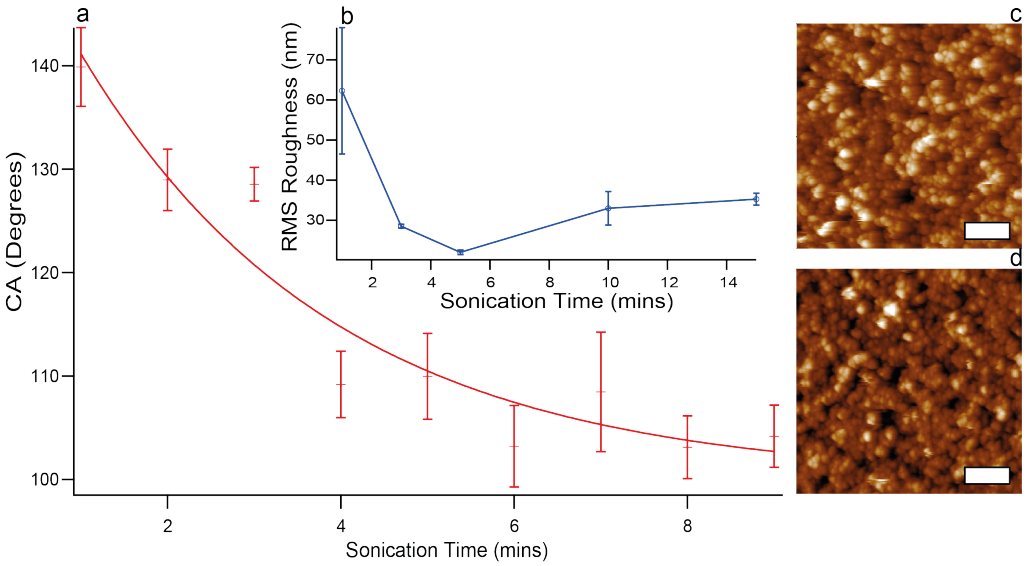

Figure 4.9: Changes in CA and roughness of NP-functionalized support surfaces upon sonication. The CA evolution measured over the NP-functionalized surface (red line, a) suggest a transition from a Cassie-Baxter to a Wenzel state. The evolution of the surface roughness shown in inset (blue line, b) is consistent with the interpretation, showing a decrease to a final plateau. The roughness evolution is likely to be a result of any loosely bound silica nanoparticles being removed, leaving only firmly attached particles. AFM images of the surface taken after 3 minutes sonication (c) and 15 minutes (d) show no dramatic change of the surface aside from possible NPs reorganization. Each CA data point represents the average of 5 measurements and its uncertainty the standard error over the measurements. Each roughness data point represents an average of 3 measurements and its uncertainty is given by the standard error over the measurements. Solid lines serve as an eye guide on both plots. The scale bars on AFM images (c-d) represent 400 nm. The colour scale is as for Fig 3.1 with a maximum height variation of 205 nm (c) and 192 nm (d).

Upon soaking in a saline solution, the un-coated nanoporous NPs layer exhibits a progressive decrease of static CA values (Fig. 4.7, NP-5 in saline), suggesting

a transition between two wetting states, similar to a Cassie to Wenzel transition. This interpretation is supported by the presence of some degradation of the surface with localized irregularities and NPs clustering revealed by AFM (Fig. 4.7c). The surface is also fragile with NPs easily removed during AFM imaging after only two days of soaking. The contact angle measurement (5 layers NP-LIS in saline, Fig. 4.7a) does not show any significant change. This result indicates that without any external perturbation, the oil layer provides a protective coating, preventing the solution from interacting with the NPs and degrading the surface. If the solution comes into contact with the NPs, it can destabilize and modify the surface. This is likely to be due to metal ions facilitating the removal of the hydrophobic ligands from the surface of the silica NPs. Since the ligand is tethered to the silica core by silane chemistry, they can be displaced under appropriate conditions [162]. This would result in hydrophobic ligand clusters aggregating on the surface, consistent with the AFM images of the degraded surface (Fig. 4.7b, c).

4.4 Discussion and Conclusion

LISs have the potential to revolutionize antifouling coating, offering a more efficient and environmentally friendly alternative to existing solutions. However, any real-life application requires a clear understanding of the LIS ageing over time so as to enable the targeted development of better, more flexible surfaces, that can withstand the demands of their intended application. Here, the ageing of the model LISs prepared according to standard protocols are tracked. Using a dual micro- and macroscale experimental strategy, functional changes in the LISs performance are linked with specific oil loss mechanisms and nanoscale effects in the porous layer. It is found that the initial oil layer is usually not at equilibrium, leading to significant oil loss, even when stored under ambient conditions and without any external perturbation. When immersed in aqueous solutions and exposed to high intensity ultrasonic pressure waves, the oil loss significantly accelerates, inducing changes in the CA and CAH. The pressure waves create aqueous micro-droplets in the oil layer, progressively pinching out the oil from the LIS, as cloaked droplets move out

of the oil phase back into the bulk aqueous solution. The rapidity of the depletion process is weakly dependent on the colloidal stability of the micro-droplets. This mechanism, to the best of our knowledge not previously reported, appears central to the ageing of the LIS exposed to the impact of waves. In our simple model LIS, this "pinching" mechanism induces an important side effect: the irreversible degradation of the hydrophobic NP coating used to retain the LIS' liquid. The NP coating plays an important role in the LIS performance, which is maintained more than ten times longer for the nanoporous NP-coated supports compared to the smooth flat supports. However, the current findings highlight inherent weaknesses in the use of facile nano-structured NP coating exposure of the LIS support to the aqueous solution, causing both chemical and structural degradations.

Taken together, the present results provide clues to design robust LISs, for example, aimed at real-life applications that entail the impact of water drops or waves. First, using a retention support that does not require chemical functionalisation, unlike the hydrophobised particles used here, would offer an obvious strategy to remedy LIS degradation, potentially increasing the lifetime of both the support and the resulting LIS. This is especially true for substrates exposed to saline solutions, where the contaminate degrades the substrate more quickly. If the LIS is designed for being reinfused periodically, chemical resistance to the environment (other than the infusing liquid) is necessary to avoid degradation over short timescales. Second, mechanical restructuring of the porous layer may also need to be considered depending on the application.

Overall, this chapter shows that the ageing effect on LISs can be significant when exposed to non-ideal environmental conditions. Practical and application-oriented developments of LISs are likely to become a key aspect to LIS adoption in technology and industry, beyond the many fundamental developments currently driving the field [66,77,80,136,163]. The ageing mechanisms depend on the specific details of the system considered and should be tailored for the applications of interest [17,37–39,85]. The present work could act as a reference point for future work involving the testing of new LIS applications, in particular the development of a standardized,

accelerated ageing strategy, to determine the robustness and durability of novel products.

4.5 Experimental Methods in Chapter 4

4.5.1 Preparation of Liquid Infused Substrates

Glass slides were prepared following a literature protocol as described in Chapter 2 and elsewhere[120]. Briefly, glass substrates were cleaned using Decon 90 (Sigma-Aldrich-Merck, Gillingham, UK), followed by alternating steps of rinsing and sonication (30 min bursts) in ultrapure water (18.2 mW Merck-Millipore, Hertfordshire, UK). Slides were then left to dry in air. Subsequent rinsing of the slides was carried out consecutively in acetone (purity 99% (Emplura), Sigma-Aaldrich-Merck, Gillingham, UK), and isopropanol (purity 99.8 %, Fisher Scientific, Loughbrough, UK) and dried under a stream of nitrogen. After 30 mins in air, a layer of hydrophobized nanoparticles was sprayed evenly across the slide surface (GLACO^{TM} spray, SOFT 99 Corp. Japan) and left to dry for 60 mins. Additional layers were applied every hour until a total of five coats was achieved unless otherwise specified. A drop (0.5 mL) of silicone oil (20 cSt at 25 °C, Sigma-Aaldrich-Merck, Gillingham, UK) was then placed at the centre of the slides and immediately spin coated (1000 rpm 1 min, then 500 rpm 1 min). Slides were used fresh, and any storage (outside ageing) was done with the slides placed in petri-dishes with closed lids at ambient temperatures.

4.5.2 Preparation of Dichlorodimethylsilane Hydrophobized Glass Substrates

Glass slides were hydrophobized with dichlorodimethylsilane (DMS) to serve as control experiments. The preparation is described in further detail in Chapter 2 and followed established protocols[121]. Slides were soaked sequentially in acetone and isopropanol, each for a minimum of 30 mins. They were then dried using a

stream of nitrogen, plasma cleaned for 15 mins (>30 W, VacuLAB-X, Tantec, UK) and subsequently dehydrated in an oven at 100 °C for 60 mins. The slides were then immediately placed inside a desiccator next to 1 ml of DMS placed in an open dish. The desiccator was then placed under vacuum overnight to allow for DMS vapor deposition on the slides. After functionalization, the slides were rinsed with acetone and ultrapure water and dried overnight at 40 °C.

4.5.3 Practical DLS Analysis

A drop of oil (100μl) was placed in approximately 10ml of either pure water or saline and placed in a sonic bath. 1 ml of the resulting solution was immediately pipetted into a cuvette and placed in the ZetaSizer Nano. An average of 12 measurements was used to create each peak displayed.

4.5.4 Ageing using Static Soaking

Freshly prepared nanoparticle-functionalized slides and the LIS were placed in a sealed beaker containing either ultrapure water or a 600 mM NaCl solution. The samples were removed periodically to make contact angle measurements or for nanoscale imaging with AFM.

4.5.5 Accelerated Ageing using Sonication

Samples were placed in a beaker containing either ultrapure water or a 600 mM NaCl solution and sonicated in bursts of 1 min, using a VWR, USC-TH bath sonicator (VWR, Lutterworth, UK). The ultrasonic bath operates at 45 kHz and has an average output power of 180 W. Using a bespoke liquid displacement sensor built from piezo-ceramic bi-morph (RS PRO Vibration Sensor, model 285-784, RS Components, Northants, NN17 9RS, UK), it was possible to estimate the average ultrasonication power at the location of the sample, yielding a value of 800 $\pm$ 400 Wm^{-2}. The associated oscillatory displacement velocity of the aqueous solution

at the sample's surface is in the order of 8 ms^{-1}. Similar to static ageing, samples were removed periodically to make contact angle measurements or for nanoscale imaging with AFM.

Chapter 5

Designing a Setup to Characterise Capillary Liquid Bridges on Liquid Infused Surfaces

Capillary liquid bridges (CLBs) are ubiquitous in nature and are present in many industrial processes. In order to model their behaviour, it is essential to develop suitable experimental tools able to characterize the bridges' geometry and the associated capillary force they induce on the contacting surfaces. While many existing setups are capable of characterizing capillary bridges formed between conventional surfaces, quantitative measurements on smart surfaces such as liquid-infused remain challenging. These surfaces typically exhibit weak contact line pinning and contact angle hysteresis resulting in unusually small changes in the capillary force they exert upon extension or compression of the bridge. Although it is precisely these properties that drive the interest into liquid infused surfaces, they render experimental characterization challenging when compared to non-infused surfaces. Here, this issue is tackled by developing a relatively inexpensive setup capable of measuring capillary forces with a sensitivity in the micronewton range, while

quantifying the bridge's geometry. The setup is fully motorized and can vary the relative position of the contacting surfaces while maintaining synchronous force and geometry measurements. New analysis software is also developed to retrieve the relevant geometrical parameters of the bridge from optical observations while minimizing errors and noise. Using example surfaces, the setup's capabilities are demonstrated, including for bridges between liquid infused surfaces.

Published as: Development of a setup to characterize capillary liquid bridges between liquid infused surfaces **Sarah J. Goodband**, Halim Kusumaatmaja, and Kislon Voïtchovsky, *AIP Advances* 12, 015120, 2022.

Also published as a Scilight: Blueprints offer replicable method to measure capillary liquid bridges, Chris Patrick

5.1 Introduction

Capillary liquid bridges are created when a droplet of liquid forms a stable link between two surfaces, usually solids. In nature, countless examples of water based CLBs can be found, from the cohesive force holding soil and sandcastles together [93], to the adhesion of small animals and insects to surfaces [94,95,164], the function of our joints [165] and in several respiratory diseases [91,92]. In technology and industrial applications, CLBs are also ubiquitous in processes such as soldering [166,167], lithography [88], oil recovery [89] and cement drying [90], with potential for medical processes such as stem cell and drug delivery [168]. The behaviour of CLBs is influenced by many environmental and physical factors as well as the fluid used to create the bridge. The exact shape of the CLB and the force it exerts on the contacting surfaces is determined by an interplay between the surface tension of the liquid, the shape of the surfaces, and the affinity between the liquid and the surfaces. Gravity also influences CLBs, but its effect only becomes noticeable at scales larger than the so-called capillary length; about 2 mm for pure water. Given the importance of CLBs in science and technology, considerable research aims at modelling [103,110,169,170] and experimentally characterizing their properties [171–173]

over a wide range of relevant conditions.

Experimentally, a variety of setups have been developed to explore CLBs stretched between parallel, or non-parallel solid plates. At the nanoscale, force measurements typically rely on atomic force microscopy [171,172] or similar devices [173]. Nanobridge sizes range from a few nanometers to hundreds of nanometers and the associated capillary forces from piconewton to tens of nanonewtons. Although highly precise spatially, such measurements do not allow for direct visualization for the CLB or characterization of its shape while being deformed. Asperities or chemical inhomogeneities of the surfaces can also dramatically affect the measurements which usually involve atomically flat, ideal surfaces that are not representative of most applications. In contrast, CLB measurements over the millimeter scale allow for direct visualization of the CLB evolution as the distance between surfaces changes [98,174–178]. At that scale, capillary forces are typically in the range of millinewtons [98,174] and the effect of gravity may need to be taken into consideration depending on the particular system considered [179]. Given the relatively large size of CLBs, the geometry and chemical properties of the surfaces can be well controlled on the CLB scale, including via the introduction of chemical patches [175,180], surface corrugations [181] or non-parallel geometries such as spheres [174] and wedges [176].

While standard nanoscale and millimeter-sized 'macroscale' measurements have enabled significant advances in the field, many phenomena involving CLBs fall in the in-between region, where capillary forces range between sub-micronewtons to hundreds of micronewtons. In this range, directly observing the CLB is usually still possible, but measuring the force it exerts on the contacting surfaces becomes challenging and requires bespoke experimental setups [182]. Such setups are usually expensive, highly specialized and unsuitable for routine measurements.

This gap is all the more problematic with the advent of liquid infused surfaces (LIS) where CLBs are only expected to induce micronewton force changes when extended, even at the millimeter scale. Simulations have captured some aspects of CLBs formed between LISs [110], but experimental studies are lagging behind, owing to the difficulties associated with such measurements.

In this chapter, I develop a novel setup to study CLBs between parallel plates with improved force sensitivity, down to the micronewton range. The plates can be functionalized with any desired surface making the system suitable for measurements on LISs. The setup, built from relatively inexpensive and commercially available parts, is fully motorized for relative displacements of the surfaces over several millimeters. It is versatile and can be easily adjusted to suit different geometrical configurations or work in specific environments. It can incorporate multiple cameras working simultaneously (here two) for more accurate measurements, and a bespoke software is developed to drive the experiments and subsequently analyze the data collected from the camera and the force sensor. I illustrate the setup's measurement capabilities by tracking the changes in force and geometry associated with the extension and compression of CLBs between salinized glass surfaces and between planar LISs that exhibit similar contact angles.

5.2 Setup Developed

The setup developed in this thesis uses a standard design[98,174,175] with one of the surfaces fixed and the other motorized and suspended to a high-precision force sensor. Cameras provide direct visualization of the CLB's geometry, with all pieces of hardware controlled and synchronized using the same computer software. While several hardware and software aspects of the development improve on existing setups, the key improvement is the force sensitivity (accuracy to 4 μN), with demonstrated measurements on CLBs between LISs. This improvement also entails some limitations that are discussed later (Chapter 5.5).

5.2.1 Components and Parts

The key building elements of the setup are a micronewton sensitive force cell (Novatech Measurements Limited, St Leonards on Sea, UK), a high-quality digital camera (IDS Imaging Development Systems GmbH, Obersulm, Germany) and motorized stages (Thorlabs LTD, Ely, UK), all interfaced, synchronized and controlled

using LabVIEW (National Instruments, Austin Texas, US). Each item is listed in Table 5.1 with the key elements labelled as 'essential' while optional improvements are labelled as 'optional'.

Part name and model	**Importance for set-up**
Base	
Nexus B4560A Breadboard, 450 mm x 600 mm x 60 mm, M6 x 1.0 Mounting Holes (Thorlabs)	essential
Z-stage mounting system	
Lab Clamp stands(Various)	essential
KVS30/M - Kinesis 30 mm Vertical Translation Stage, M6 and M4 Tapped Holes(Thorlabs)	essential
GNL10/M-Z8 - Large Motorized Goniometer, 25.4 mm Distance to Point of Rotation, ± 8°, Metric(Thorlabs)	optional
MT1/M-Z8 - 12 mm (0.47") One-Axis Motorized Translation Stage, M6 Taps(Thorlabs)	optional
KDC101 - K-Cube Brushed DC Servo Motor Controller (Thorlabs)	essential
Camera system	
MVL6X12Z - 6.5X Zoom Lens with 12 mm Fine Focus (Thorlabs)	essential

continues on next page

MVL6X05L - 0.5X Magnifying Lens Attachment for 6.5X Zoom Lens (Thorlabs)	essential
High sensitivity Digital camera UI-3880CP-M-GL Rev.2 (IDS)	essential
Custom extension tube for camera mounting (In-house)	essential
PT102/M - Right-Angle Bracket for PT Series Translation Stages (Thorlabs)	essential
Force sensor and mounting	
P300/M - 1.5" mounting post, M6, 300 mm (Thorlabs)	essential
C1511/M - 1.5" post mounting clamp, 63.5 x 63.5 mm^2 (Thorlabs)	essential
DSC USB Load cell Digitizer (Novatech)	optional
F329 Deci-Newton Load cell (Novatech)	essential
Custom force sensor mounting plate (In-house)	essential
PT1/M - 25.0 mm translation stage with standard micrometer, M6 (Thorlabs)	essential
Easyfix blue zinc-plated hose clip (Screw-fix)	essential
Illumination	
ICEFIRE T70 torch LED (Amazon)	essential

continues on next page

Custom diffusing screen (In-house)	essential
Second Camera Set-up	
Dino-lite-AM7915MZT-EDGE (Dino-lite)	optional
Lab clamp stands (Various)	optional

Table 5.1: List of the different parts used to create the CLB measurement setup. Some basic parts were made in-house.

The different items are assembled as shown in Fig. 5.1. The force sensor (Novatech, F329 Deci-Newton Loadcell), mounted on the vertical motorized stage (Thorlabs, KVS30/M), can operate symmetrically in both traction and compression. A top position with the sensor suspended to a custom-made holder was chosen. Both the top and bottom stages can be manually adjusted to change the sample position when loading, including the relative tilt angle (usually around 0.5 degrees) of the bottom plate. This is useful to apply minute corrections of the plate parallelism. Removable plates can be screwed into the force sensor, allowing for different surfaces to be easily and stably mounted. Suspending the force sensor has a number of benefits: it protects against liquid ingress when using very mobile droplets, prevents oil shed during longer experiments or due to droplet rolling contaminating the sensor, and gives the sensor some protection from the user who is less likely to knock or touch it. In this way, the sensor is only ever contacted by droplets that are gently brought into contact using the z-stage. The custom-built holder is attached to a thick post (Thorlabs, 300 mm post) to hold the entire unit steady as measurements are taken. An optional horizontal stage (Thorlabs, PT1/M - 25.0 mm Translation Stage) can be used for shearing experiments (suggested use in Chapter 7).

The main camera (IDS, UI-5880CP Rev. 2 GigE CMOS camera[183,184]), takes a video of the capillary bridge during the stretching experiment at 5 fps (or higher as

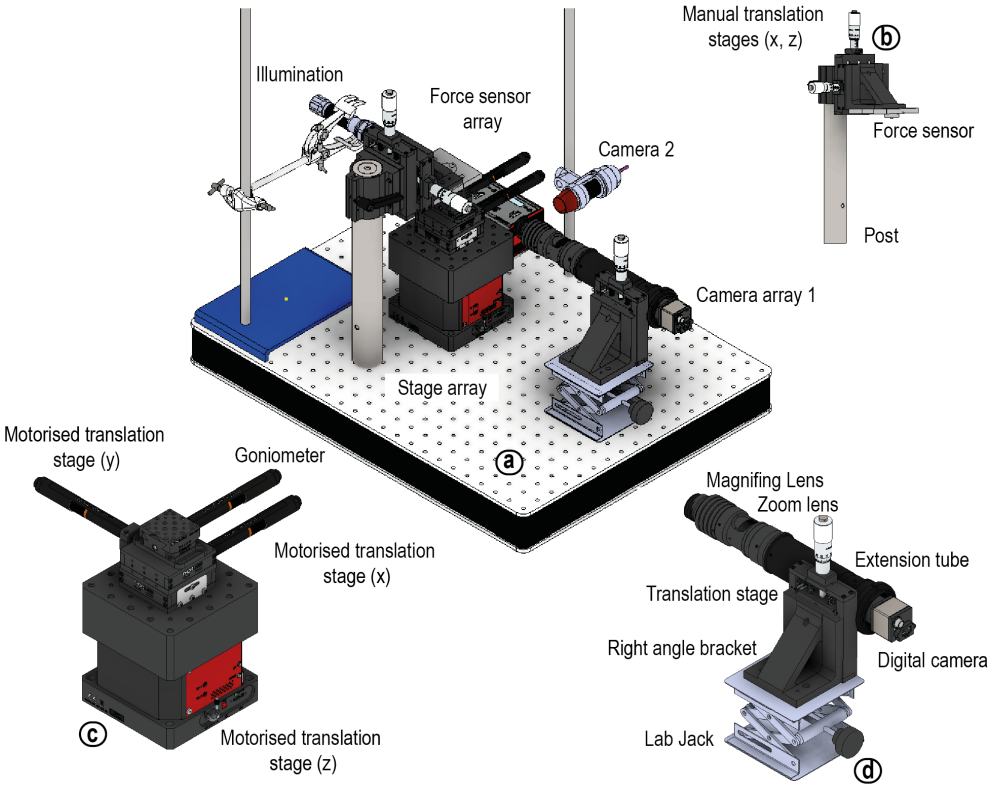

Figure 5.1: Technical drawing of the developed setup. (a) The fully assembled setup is shown without any of the wires to aid visualization. The main components are magnified in the edges with full labelling (b-d). (b) The force sensor is attached to a custom holder and is suspended above the stage array. There are manual stage controls attached to the force sensor mount to assist with set-up. (c) The Z, Y and tilt stages are all mechanically driven. (d) The main camera (UI) has an adjustable lab jack and manual stage for fine adjustments to the setup. The second camera (dino-lite) is mounted on a lab stand. Fine adjustment is not required for this camera since it is used primarily to ensure the plates are lateral, and determine how much (if any) the droplet has moved away from the front camera. Both cameras are mounted on custom holders.

required). It is focused so as to track accurately the edges of the CLB and angled with respect to the plates to get a good view of the top contact angle and the bridge reflection. The reflection provides a convenient way of determining the position of the surface contact accurately. Since experiments are conducted using identical contacting surfaces, tracking the bridge geometry at its top interface is sufficient to derive all the meaningful parameters for modelling in the absence of gravitational effects. The images from the video are time-stamped for synchronization with the

force sensor data, and subsequently post-processed using a bespoke python script to automatically extract the contact angles and radii of curvatures (see Chapter 5.2.3).

An optional secondary camera (Dino lite AM7915MZT – EDGE, Almere, The Netherlands) offers a synchronized side view of the CLB. It is primarily used for measuring the initial plate separation but can also be used to track droplet movement in the transversal direction to the plane imaged by the main camera. This is useful to monitor possible lateral motion of the CLB (and if necessary, bring suitable corrections) and to ensure the radii measured are correct. The second camera also helps identifying pinning events missed by the primary camera when working with standard surfaces. From both cameras, the diameter and the surface curvature of the droplet can be accurately quantified for each frame during post-processing.

All the hardware components of the setup interface with LabVIEW where a bespoke program controls their movement and collects all the data synchronously to ensure accurate timestamping of each component (see Appendix A2). The choice of using LabVIEW is motivated by the fact that it easily interfaces with the control software of most instruments. Many companies provide dynamic-link library (dll) and driver files such that the full capacity of all the instruments can be utilized without the need for machine-level programming. The entire setup is placed in a perspex box (custom built) with an anti-vibration stand (Thorlabs, B4560A - Nexus Breadboard) to prevent environmental changes from affecting the measurements. The perspex box and the anti-vibration table shield the delicate force sensor from uncontrolled environmental effects and reduce the noise in the system. The box also allows for the local environment (temperature and humidity) to be controlled around the capillary bridge.

5.2.2 Measurement Protocol

In a standard CLB stretching or compression experiment, the measurements are conducted as follows:

1. The two surfaces of interest are prepared on circular glass coverslips (Agar scientific, 24 mm) and glued onto custom-built thin metal mount using fast curing, air dry glue (Reprorubber thin pour, Bowers Group, Camberley, UK)). After 2 hours of curing, the surfaces and metal mounts are screwed into place in the static baseplate and the force sensor of the setup. The whole setup is then left to equilibrate for an hour before the measurements begin.

2. The camera and the light source are adjusted to ensure suitable visualization of the CLB for the desired experimental conditions.

3. The force sensor may be zeroed to remove the offset due to the weight of the sample and mount. For measurements where only the change of force is of interest, the system offset can simply be removed at the stage of data processing, leaving relative force measurements.

4. The force sensor and the camera begin recoding data. The measurement effectively commences approximately 1-2 mins after first contact. This allows the force sensor to be fully at equilibrium before starting to collect meaningful data.

5. The stage can be set to move at a particular velocity, and over a particular distance.

6. The stage can be set to repeat the stretching/compression motion as required.

7. After completion of the experiment, the timestamped data from each instrument is outputted as a text file (force) or video file (camera) for post processing.

8. The data is passed onto a python script for semi-automated post-processing and extraction of the geometrical parameters.

5.2.3 Software and Analysis

All the code for data acquisition and processing is available in Appendix A1 and 2. A brief description is also given below.

Setup control: Development of a LabVIEW setup to control the different pieces of equipment is relatively straightforward and based on the dll files provided by the different manufacturers or existing LabVIEW modules. The software controls the motion of the different stages (vertical, lateral, and tilt angle) as well as the cameras and the data acquisition with timestamping.

Data analysis: All the automated data analysis of the images captured by the cameras is carried out by custom made procedures programmed in Python. The procedure uses canny edge detection to obtain the silhouette of the bridge. By adjusting the two key detection parameters (minVal and maxVal), the number of edges detected can be increased or decreased to capture just the relevant image information. Constraints are added to the system to filter any features that could impede measurements. From these edge values, a second order polynomial curve is fitted to each side of the bridge. The curvature and gradient at each point of the edge are obtained from the first and second derivative of the quadratic polynomial fit, respectively. The gradient at the contact point with one of the plates is used to calculate the contact angle, while the corresponding curvature, K, is calculated using[185]:

$$K = \frac{|\frac{d^2y}{dx^2}|}{(1+(\frac{dy}{dx})^2)^{\frac{3}{2}}}, \tag{5.1}$$

The radius of curvature R_2 (see Chapter 1, Fig. 1.9) along the bridge side is simply the inverse of K in Eq. 5.1. Using the intercept of the lines with the top and bottom plate and similar triangles determines the radii (R_t and R_b, see Fig. 1) of CLB at the top and bottom. The radius of curvature R1 (see Chapter 1, Fig. 1.9) can then be calculated using $\frac{1}{R_1} = \frac{sin\theta_1}{R_t}$ and $\frac{1}{R_2} = \frac{sin\theta_2}{R_b}$ for the top and bottom plates, respectively. The process is shown schematically in Fig. 5.2. Depending on the set of data, the analysis procedure may occasionally fail to properly extract the geometrical parameters due to a variety of external factors such as unfavourable

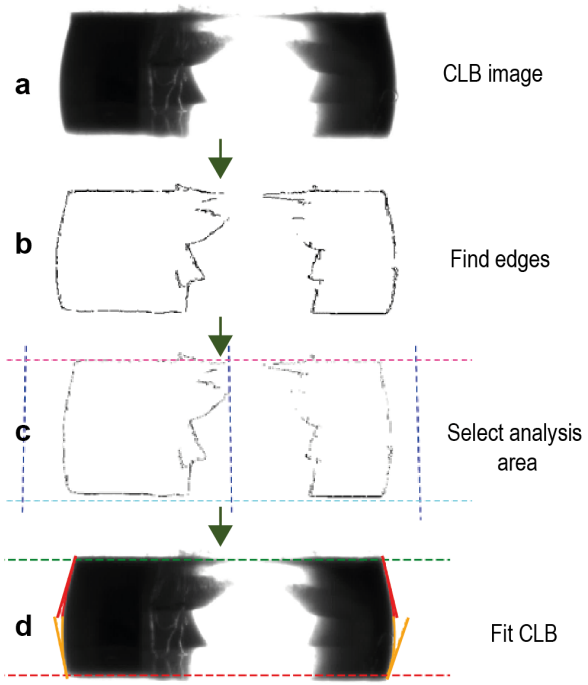

Figure 5.2: Flow diagram representation of the analysis process using a bespoke Python routine. Videos of droplets stretching are separated into frames, and each frame is analysed in turn. The edges of the bridge are detected using canny edge detection and an adjustable region of interest is selected. By selecting a region of interest, spurious additions to the images arising from noisy edge detection can be removed. The user then defines where the initial top and bottom of the bridge are, allowing for the contact angles and the different radii to be calculated. This process is repeated for each frame, with the software tracking the moving edges as the CLB expands.

light reflections and intensity or a particular positioning of the CLB. This typically translates as large, unjustified variations of the parameters between consecutive images (in particular in the contact angle and radius of curvature). If this occurs, a pre-processing step may be needed whereby certain image features or frames are removed by hand to assist in the edge detection. The fitting area may also be decreased to remove features close to the bridge edge that may interfere with the detection.

5.2.4 Comparing Measured and Calculated Forces

In an ideal experiment, the measured and calculated forces would be exactly the same. In reality, however, it is usually found that the force sensor has a small but measurable constant offset (typically 20 μN) when compared to the forces calculated from the CLB geometrical parameters using Eq. 1.10 (Fig. 5.3). While negligible for measurements involving solid surfaces, this offset needs to be taken into account when comparing calculated and measured forces with CLBs between LISs.

Practically, the experimental offset value is quantified in an objective and systematic manner for a given dataset by fitting the experimental data to the calculated data (least squares error minimization for the whole set). The process is illustrated in Fig. 5.3 where both experimental and calculated forces are given for an aligned set of data. This procedure was carried out systematically hereafter, and the data is displayed with the offset removed from the experimental measurement so as to allow better comparison of the absolute force values. The origin of the offset may be due to a variety of factors and appears to depend on the day and type of measurement conducted. This suggests that it could result from daily variation in the load cell calibration due to external parameters (temperature, humidity), or due to the position of the CLB during its set-up. However, given its small offset value, the fact that it is constant over a set of data and the possibility to compensate for it, I do not see this as a major issue.

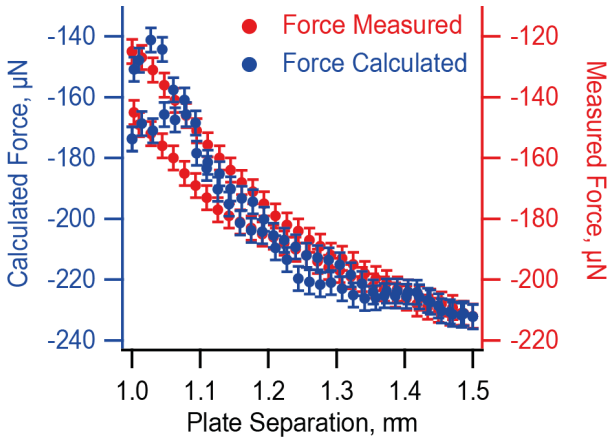

Figure 5.3: Example of force offset between the measured (red) and calculated forces (blue). The datasets have been aligned vertically using least square minimization, and the force values associated with each dataset is presented separately (left and right vertical axis). From the differences in the axis values, an offset of 20 μN between the measured and calculated forces is deduced. The uncertainties represent the standard error on the measurements.

5.3 Example of Successful Measurement

To illustrate the capabilities of the setup, some CLB measurements with surfaces composed of hydrophobic dimethyldichlorosilane-treated glass (DMS glass) and with LIS were conducted. The DMS glass was prepared by vapour deposition as described in reference[121]. The LIS was prepared following an established protocol as described elsewhere[74] and had an oil layer thickness of approximately 6 μm to limit oil ridge effects. During a measurement, the CLB is first extended by increasing the distance between the surfaces and subsequently returns to its initial position. The results are compared in Figure 6, showing a good agreement between the measured and calculated forces derived from the CLB geometry.

Fig. 5.4 illustrates the capabilities of the setup developed: both DMS glass and LIS induce a similar contact angle for the CLB, both bridges have similar dimensions, but the force variation when stretching experienced in both cases differ by a factor of $\sim$5. As expected, the contact angle hysteresis is much lower for LIS compared to DMS glass.

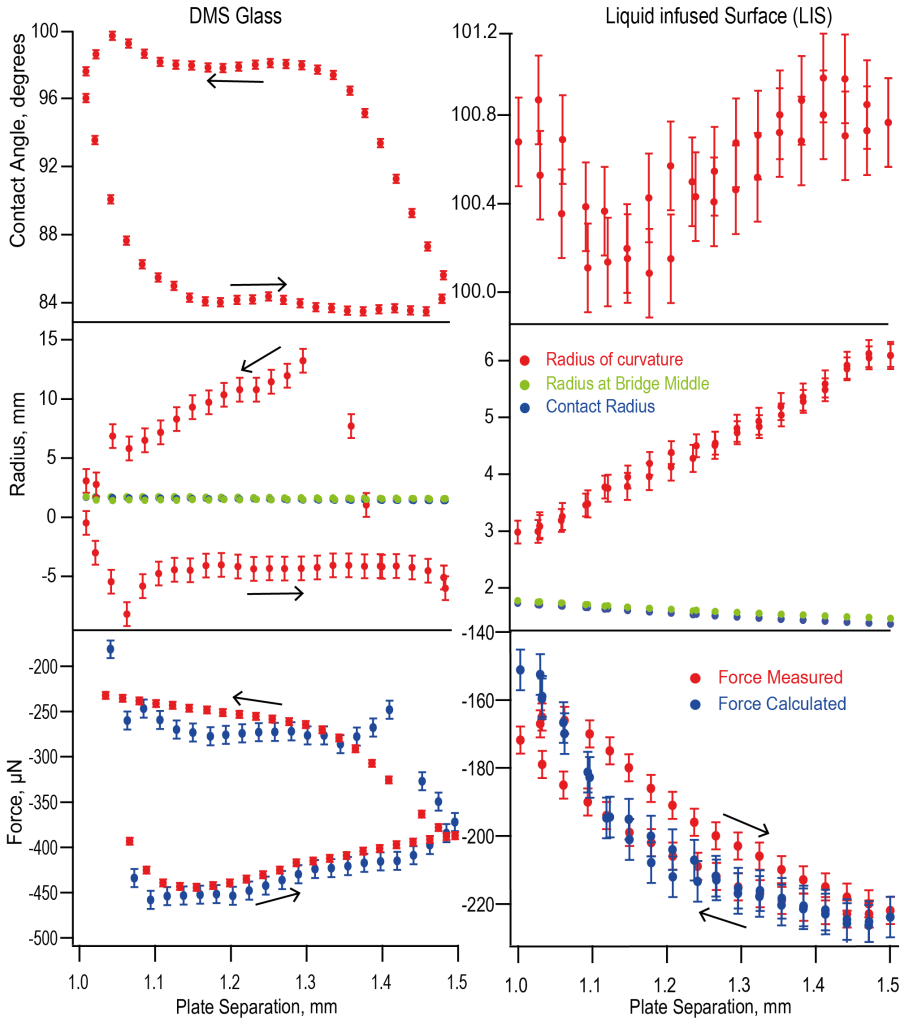

Figure 5.4: Comparative CLB measurements conducted on hydrophobized DMS glass (left) and LIS (right). The CLB contact angle with the top plate (top), contact and curvature radii (middle) and force (bottom) are shown. The variation in capillary forces is measured experimentally (red) and calculated using Eq. 1.11 based on the CLB geometrical parameters (blue). Note the difference in magnitude of the vertical scales between both experiments. Arrows indicate the measurement progression with time. The error bars represent the standard error on the measurements and may occasionally be too small to be seen. The data presented are compensated for the experimental offset (Fig. 5.3).

5.4 Troubleshooting and Limitations

5.4.1 Force Sensor Limitations

The force sensor is based on a load cell and is hence unavoidably affected by time dependent creep[186]. In practice, this means that rapid changes to the CLB geometry take several seconds to equilibrate in the associated force measurement. This should be taken into consideration when performing measurements with this setup because it imposes a limitation of the measurable CLB stretching and compressing velocities. The data shown was acquired at relatively slow stretching/compressing velocities (less than 0.01 mm/s) which provided a good agreement between the measured and calculated force values (Fig. 5.5a). In contrast, the same measurement repeated ten times faster (stretched/compressed at 0.1 mm/s) results in a significant deviation between the measured and calculated forces (Fig. 5.5b). The measured force becomes affected by a convolution with a time-dependent creep, artificially lowering the value of the measured force and preventing equilibrium measurement.

5.4.2 Bridge Pinning

Another interesting feature that can be explored is the pinning of CLB on solid surfaces. The force is measured globally for the entire bridge and is therefore always sensitive to pinning which often appears as an unexpected force evolution and a deviation from the theory (Fig. 5.6). Such pinning is, however, not always visible with the camera. This is because the camera effectively captures only a 2D projection of the 3D CLB which can create some difficulty for interpreting the results. By adjusting the side camera so that it can visualize the whole triple line of the CLB, it is possible to determine where pinning likely occurred (Fig. 5.6).

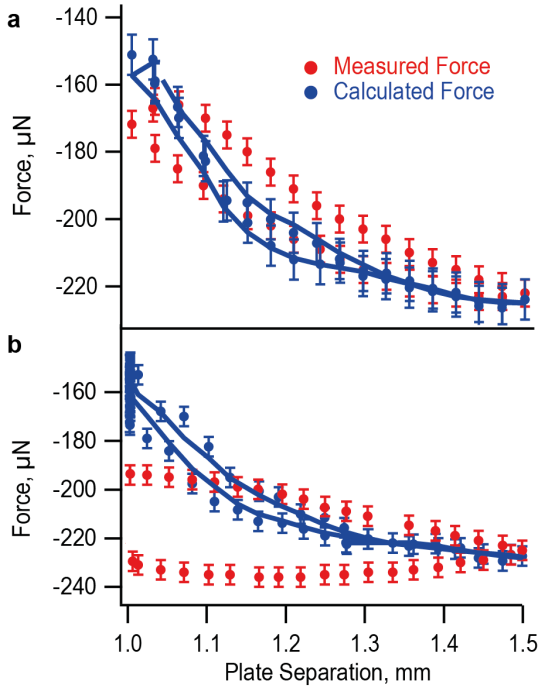

Figure 5.5: Effect of the load-cell time dependent creep on measurements. (a) When enough time is allowed by the cell to relax between consecutive measurements, a good agreement is found between the measured and calculated forces. Here the stretching/compression is conducted at a velocity of 0.008 mm/s. (b) Increasing the velocity by more than an order of magnitude to 0.1 mm/s makes creep effects appear with a significant difference between measured and calculated forces. This is most obvious when reversing the direction of motion, with the measured force being artificially lowered on the return journey. Both plots show the measured (red) and calculated (blue) forces. Eq. 1.11 was used with a 4 pts moving average applied (blue line). Error bars are the standard error for both measurements.

5.4.3 Oil Ridges for Capillary Liquid Bridges on Liquid Infused Surfaces

Oil ridges can arise on LIS with a thick surface oil layer. Experimentally, and for the type of LIS used here, this typically occurs when the oil layers exceed 12-14 μm (Fig. 5.7). The ridge appears as an obscured region where the CLB contacts the LIS' surface; ridges are mobile and can grow during measurements. The presence of ridges leaves a smaller region for fitting the CLB's edge. To some extent, this can be mitigated by adapting the analysis software so that it takes into account

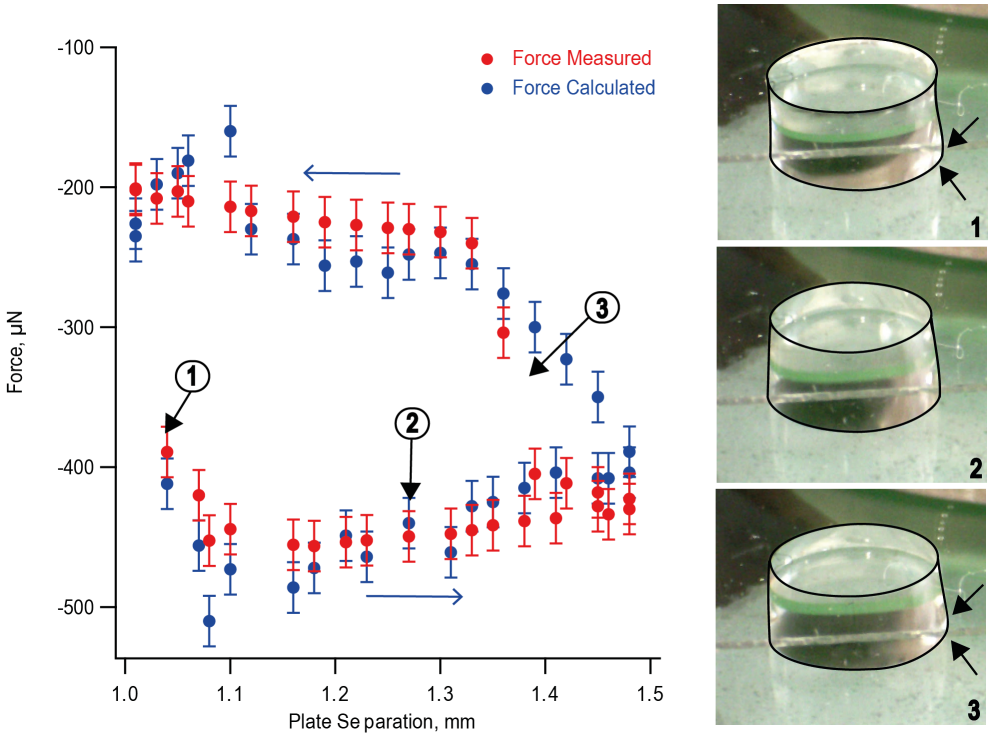

Figure 5.6: Example of pinning as detected by the setup for a CLB between surfaces of DMS glass. Image 1, 2 and 3 highlight the CLB at different times during the extension/recovery cycle. Images 1 and 3 correspond to instances of pinning (arrows) during the extension and return respectively. The pinning visually deforms the CLB which becomes asymmetrical. Image 2 is an example of the CLB while unpinned during the cycle. If the pinning is clearly visible in the image used for the geometrical analysis of the CLB (Image 1), the measured and calculated force tend to coincide. However, if the pinning occurs out of focus to the imaging plane, it may be missed out or only partially captured (Image 3), resulting in a sharp deviation between the measured and calculated forces. The measured (red) and calculated (blue, using Eq. 1.11) are shown. The offset between the two force curves has been removed as detailed in Fig.5.3.

the entire bridge to extract the geometrical parameters rather than only the region near the top of the oil ridge (see Appendix A2).

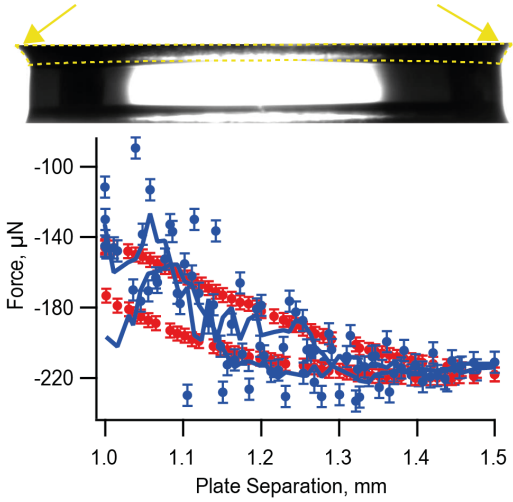

Figure 5.7: Example of CLB measurement in presence of an oil ridge. The oil ridge (dotted outline and arrows, top) renders the extraction of the contact angle and CLB radii at the top plate more challenging. By adjusting the fitting region used for the CLB's edge a better approximation can be achieved but the calculated force (blue, bottom plot) remains considerably more noisy than the measured force (red). A 4 pts moving average of the calculated force Eq. 1.11 is plotted in blue.

5.5 Discussion and Conclusion

The measurement setup developed in this thesis is designed to overcome the difficulties associated with studying CLBs between LISs. It also provides a modular set of components that offers flexibility with the ability to conduct many different types of CLB investigations. The key features of the setup are the integrated measurement of all variables, the high sensitivity of the force sensor and the custom-built analysis software to extract the relevant information from the experimental data.

The force measurement is sensitive enough to quantify the small force variations associated with experiments on LISs. It could also be used to probe forces variations associated with smaller liquid bridge deformations on conventional surfaces. The data can then be processed to high temporal accuracy with up to 20 images per second and 10 force sensor readings per second. Care must be taken to ensure that measurements are not affected by time dependent creep. While unavoidable in load cells, it can be mitigated by controlling the CLB stretching/compression velocities.

As the system has motorized stages that can move in all three direction (x, y and z), it is not limited to the simple stretching experiments shown here, but can also perform shearing experiments, or combinations of thereof. The stages position can be controlled with 0.1 μm accuracy if necessary. The isolation of the setup in a perspex box allows for control of the local environment around the CLB (e.g. humidity or temperature).

The accuracy of the calculations is currently limited by several factors. First, there is only one projection from which to measure the droplet geometry at any given time. Adding a second or third camera with a similar resolution could significantly improve the analysis by offering an average picture of the CLB and help identify pinning events. The cameras themselves can also be improved to avoid limitations inherent to the number of pixels available for the data analysis. This can be easily addressed by upgrading the camera with a model that has higher speed and resolution. The orientation of the cameras can also be readily adapted to view the footprint of the CLB or a side view, depending on the needs of the experiment.

Finally, the flexibility of the setup makes it an ideal tool to adapt to different types of systems. With measurements involving LISs, for example, large extensions can lead to higher droplet mobility and a smaller signal on the force sensor. Hence a compromise must be found in order to achieve repeatable measurement. For longer sets of measurements, using a glycerol solution instead of water reduces evaporation to a workable level over the timescales of the experiment.

In conclusion, I propose a fully motorized setup to track the characteristics of CLB between any two surfaces of interest. The setup is relatively inexpensive, comparable to the cost of an analytical balance. Its configuration is flexible, and it is particularly suitable for measurements where a high force sensitivity is required.

5.6 Experimental Methods in Chapter 5

5.6.1 Preparation of LIS Substrates

Glass slides were prepared following a literature protocol as described in Chapter 2 and elsewhere[120]. Briefly, glass substrates were cleaned using Decon 90 (Sigma-Aldrich-Merck, Gillingham, UK), followed by alternating steps of rinsing and sonication (30 min bursts) in ultrapure water (18.2 mW Merck-Millipore, Hertfordshire, UK). Slides were then left to dry in air. Subsequent rinsing of the slides was carried out consecutively in acetone (purity 99% (Emplura), Sigma-Aaldrich-Merck, Gillingham, UK), and isopropanol (purity 99.8 %, Fisher Scientific, Loughbrough, UK) and dried under a stream of nitrogen. After 30 mins in air, a layer of hydrophobized nanoparticles was sprayed evenly across the slide surface (GLACO^{TM} spray, SOFT 99 Corp. Japan) and left to dry for 60 mins. Additional layers were applied every hour until a total of five coats was achieved unless otherwise specified. A drop (0.5 mL) of silicone oil (20 cSt at 25 °C, Sigma-Aaldrich-Merck, Gillingham, UK) was then placed at the centre of the slides and immediately spin coated (1000 rpm 1 min, then 500 rpm 1 min). Slides were used fresh.

5.6.2 Preparation of Dichlorodimethylsilane Hydrophobized Glass Substrate

Glass slides were hydrophobized with dichlorodimethylsilane (DMS) to serve in control experiments. The preparation is described in further detail in Chapter 2 and followed established protocols[121]. Slides were soaked sequentially in acetone and isopropanol, each for a minimum of 30 mins. They were then dried using a stream of nitrogen, plasma cleaned for 15 mins (>30 W, VacuLAB-X, Tantec, UK) and subsequently dehydrated in an oven at 100 °C for 60 mins. The slides were then immediately placed inside a desiccator next to 1 ml of DMS placed in an open dish. The desiccator was then placed under vacuum overnight to allow for DMS vapor deposition on the slides. After functionalization, the slides were rinsed with

acetone and ultrapure water and dried overnight at 40 °C.

Chapter 6

Comparing the Behaviour of Capillary Liquid Bridges on Substrates with Different Wetting Properties

Capillary liquid bridges (CLBs) form a mobile link that can exert force on the contacting surfaces. They are commonly found in nature and underpin many industrial processes. Predicting the behaviour of CLBs can be achieved with theoretical models when at equilibrium, but the larger number of parameters at play renders systematic experimental studies challenging. The size of the system, the thermodynamical properties of the liquid and the surfaces, their mutual affinity and the detailed geometry of the interface can all influence the measurements. Additionally, pinning and hysteresis effects can render measurements system-specific and difficult to reproduce. Liquid-infused surfaces (LISs) can overcome these difficulties, but they present novel experimental challenges in order to derive quantitative information. In this study, we quantitatively compare the evolution of CLBs between solid hydrophilic surfaces, hydrophobic surfaces and LISs. In all cases the bridges have the same volume (10 μL) to ensure comparability, and all the CLB parameters are

quantified, including the capillary force it exerts on the surfaces as the bridge is extended and retracted. Comparison with theoretical models highlight the advantages and limitations of each system, including effects of line pinning and gravity. We also explore asymmetric bridges involving LISs and make recommendations for best practice when running experiments.

6.1 Introduction

Capillary liquid bridges (CLBs) form when a droplet of liquid bridges two surfaces, creating a mobile link that can exert a force on the surfaces. In nature, CLBs can be found in countless phenomena, from controlling the cohesion of soil and granular mixtures such as sandcastles[93], to the adhesion of insects and small animals to surfaces[94,95], and helping wading birds to feed[96]. CLBs are also present in many industrial processes such as in lithography[88], oil recovery[89], cement drying[90] or novel methods of drug delivery in medicine[91,92]. In all these examples, the macroscopic properties and evolution of the system considered depend on that of the individual CLBs present. The behaviour of the CLBs is in turn determined by the nature of the liquid, the size of the bridge, the properties of the surfaces as well as environmental factors such as temperature and humidity. The large number of parameters at hand is reflected by a considerable body of research investigating the impact of the surfaces geometry (e.g., planar or spherical)[101,106,108,173,187,188], their chemical and topographical patterning[100,104,189], the wetting properties for the liquid forming the bridge[182,190], and the system scale from nanometres[191–194] to millimetres[97,99,100]. Full characterisation of the CLB studies requires knowledge of the capillary force the bridge exerts on the contacting surfaces[97,99], variations in its contact radii and contact angles[98,103] as well as changes in its surface curvature[195].

Despite these advances, our understanding of CLBs remains incomplete, especially experimentally. The majority of experimental works on CLBs to date focus on hydrophilic surfaces where contact line pinning and the resulting hysteretic behaviours

dominate[98,100,103,108,188]. Studies on hydrophobic surfaces are scarce[100,103], and it is non-existent for smart surfaces such as LISs where contact line pinning and contact angle hysteresis are essentially removed[55,67,109,196]. A recent theoretical work by Shek et al.[110] suggests that the presence of a lubricating liquid in LISs leads to a fundamentally different force, contact angle and contact radius behaviours when compared to non-infused surfaces[110]. LISs have also been explored in terms of droplet transport between surfaces[197]. Understanding these behaviours is both important and timely given the expanding technological interest in LISs[19,21,68,77,78,198,199], including in the fields of coatings, printing, packaging, and microfluidics.

Here, we exploit a bespoke setup recently developed to tackle CLB measurements on LISs[200] in order to systematically compare the evolution of CLBs between 'standard' hydrophilic and hydrophobic surfaces as well as LISs. In each case the CLB geometry and the associated capillary force is quantified as the CLB is extended or retracted. Bridges with identical volume and composition are used in all cases and the hydrophobic surface is selected to exhibit a similar contact angle as LISs with the CLBs so as to allow direct comparison. We also examine the impact of gravity and CLBs with asymmetric surface composition. A fully quantitative comparison between the experimental results and theoretical predictions provides novel insights into the different factors at play in each system as well as recommendations for best practice.

6.2 Results and Discussion

6.2.1 Symmetric Capillary Liquid Bridges

Figure 6.1 shows a direct and visual comparison of symmetrical CLBs formed between two hydrophilic glass surfaces (Fig. 6.1a, d), two DMS-hydrophobised glass surfaces (Fig. 6.1b, e) and two LISs (Fig. 6.1c, f). For the sake of clarity, the hydrophilic glass and the DMS-hydrophobised glass surfaces will hereafter be re-

ferred to as 'Glass' and 'DMS' respectively. In each case, the CLBs are shown at the minimum (Fig. 6.1a-c) and maximum extension (Fig. 6.1d-f) of the bridge, as probed in this study. It is immediately obvious that the bridge's geometry is different in each case. With Glass, the hydrophilic contact results in CA close to 50 degrees before the extension. Due to a combination of pinning and sliding, the CA decreases as the bridge is extended (Fig. 6.1d). Over the DMS substrate, the CLB exhibits hydrophobic ($> 90°$) advancing angles at low extension and hydrophilic ($< 90°$) receding angles when extended. In contrast, the CLB on LISs exhibits little change in CAs upon extension due to its ability to slide without friction across the LIS. In all cases, the radius of the contact area between the CLB and the surfaces decreases with the bridge extension, both at the top and bottom contacts. The CLB on glass exhibits the smallest radius change due to significant pinning.

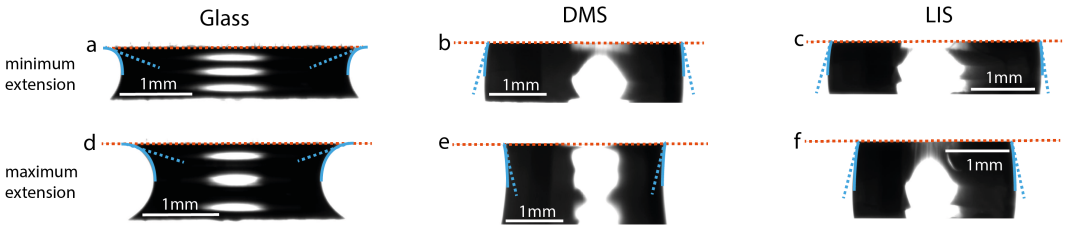

Figure 6.1: Comparison of the CLBs geometries between the Glass, DMS and LISs. In each case the CLB silhouette is given at minimum and maximum extensions. Spurious light reflections on the CLBs have been removed for clarity. For this data set, the focus was adjusted on the contact between the CLBs and the top plate. As a result, the bottom data is obscured and often not fully captured. An explanation of this can be found in Fig. 6.5

To better quantify the observations of Fig. 6.1, it is necessary to track the precise evolution of the different geometrical parameters such as CA, radius of the contact area between the bridge and the surfaces, and the surface curvature of the bridge as a function of the bridge extension. This is presented in Fig. 6.2, measured at the top of the CLBs in each case.

On the 'standard' Glass and DMS surfaces, the CA, contact and curvature radii

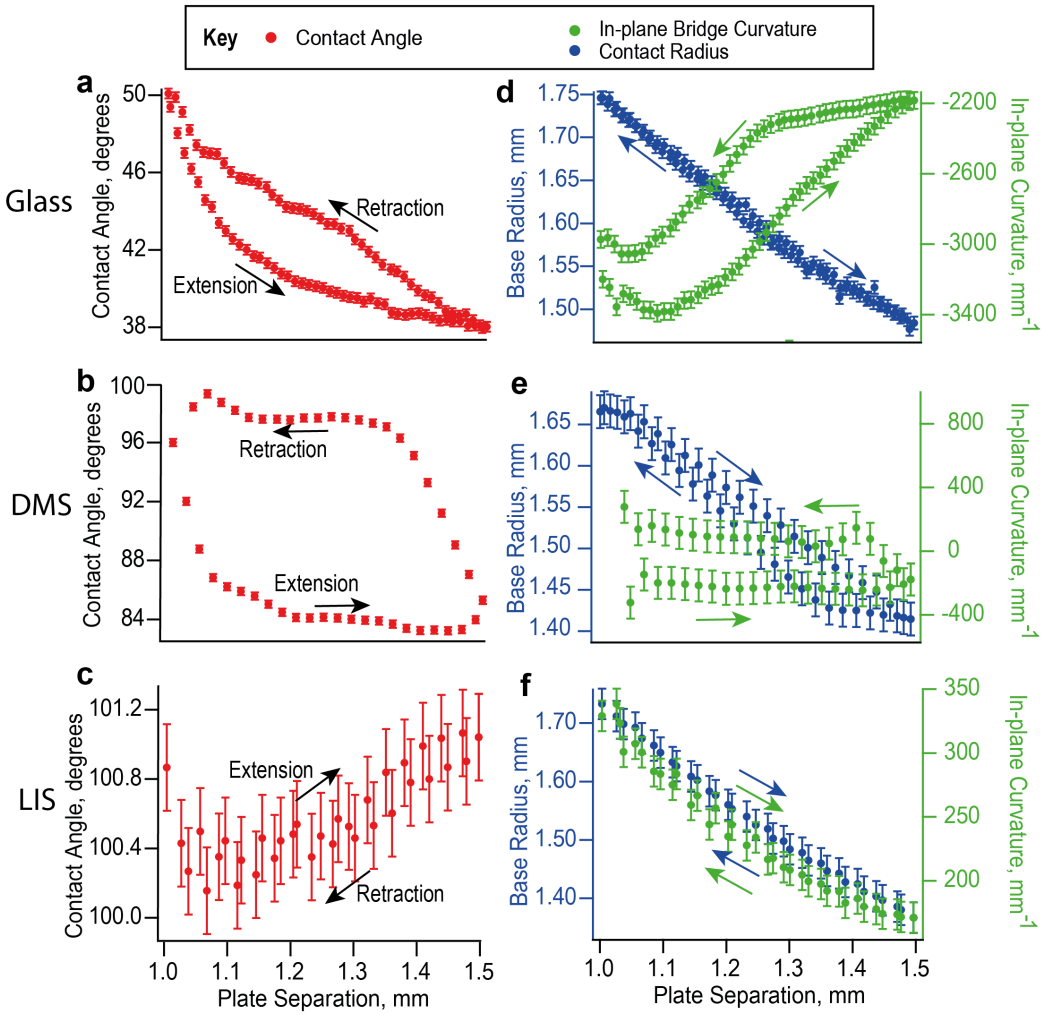

Figure 6.2: Comparison of the CA (red), contact radius (blue) and radius of curvature (green) of the CLB measured at the interface with the top surface during a extension-retraction cycle. The glass surface (a, d) shows a constantly changing contact angle, with a rate dependent on the bridge extension. This indicates a stick-slip behaviour of the contact line. The DMS surface (b, e) shows a constant advancing and receding contact angle. Contact line pinning can be seen in the contact radius over flat regions: the curvature is constant when the contact angle is constant but changes rapidly when pinned. The LIS (c, f) shows a contact angle that slightly increases as the bridge is extended. The change in contact angle, is not associated with pinning but is due to interactions with the oil layer (discussed later in the text). The radius decreases linearly.

vary as the CLB is extended. Over the glass surface (Fig. 6.2a, d), the CLB explores a large range of constantly changing CAs in conjunction with contact line motion.

No plateaus are observed either as the CLB contact line advances or recedes. This is indicative of a complicated stick-slip behaviour involving alternating pinning and rapid movements of the contact line. The pinning is obvious when comparing the change in contact radius between Glass and LISs (same bridge size). The Glass contact radius changes by 0.27 mm, while that of the LIS where no pinning takes place changes by 0.4 mm. The DMS surface shows the typical contact angle hysteresis expected on hydrophobic surfaces[98]. The advancing and receding CA (98° and 84° respectively) form two plateaus during the CLB retraction, respectively extension. The associated contact radius also exhibits a hysteretic behaviour. In contrast, the LIS shows no CA hysteresis within error. The contact angles, however, do increase with extension due to interaction of the CLB with the oil ridge of the LIS. This is addressed in more details further in the text, when discussing gravity effects. There is however no pinning and the surface base radius is free to move. The CLB on Glass shows high curvatures, 3000 $mm^{-}1$ on average, as a result of the low contact angles. CLBs on DMS and LISs show curvatures an order of magnitude smaller than Glass, but similar with each other (300 $mm^{-}1$). This can be explained by the similar contact angles they form with these surfaces. However, DMS explores both positive and negative curvatures as its contact angle varies from above 90 degrees to below 90 degrees, while LISs only experience positive curvatures due to their relatively constant contact angle.

Aside from the parameters presented in Fig. 6.2, it is useful to consider the displacement of the contact line over a full extension-retraction cycle; CLBs do not necessarily move uniformly when pinning occurs. This can be quantified by tracking the point of contact between each side of CLB and each surface, as visible in the 2D images of the system. Evaluating any asymmetry between the displacement of both sides of the bridge is a clear indication of pinning. Unsurprisingly, the smallest asymmetry is observed for Glass and LIS due to strong pinning and frictionless motion respectively. In contrast, a larger asymmetry is observed for DMS due to a combination of pinning and significant contact line displacement. This is consistent with the expected behaviour for each system as shown in Fig. 6.3.

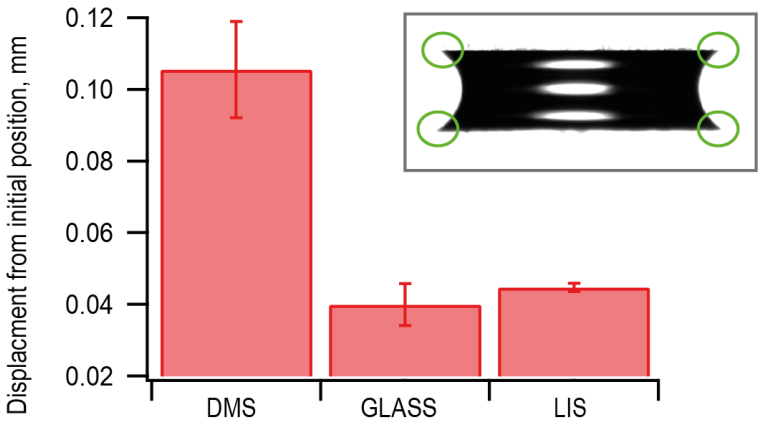

Figure 6.3: The change in initial position for the contact line is shown. Bars represent the mean displacement of the contact line as measured at 4 separate points. The hydrophilic surface can be seen to displace very little due to high pinning (as shown in Figure 6.2, the contact angle constantly changes). The error on the measurement represents the uneven movement of the contact lines (meaning one side may preferentially move more than the other). Comparing the two hydrophobic surfaces, the LIS slides very slowly during the course of the measurement. This means the contact lines displace at the same rate leaving a small error. The DMS experiences pinning and a large displacement (sliding), which means that the contact lines do not move evenly and remain pinned, leading to larger displacements and errors.

It should be noted that consistent experimental protocols are important for glass and DMS surfaces where pinning is dominant. Here, we always put the droplet initially on the bottom plate. Placing the droplet on the top plate can lead to very different measurement results (Fig. 6.4). Additionally, quantifying pinning requires accurate tracking of the contact line between the CLB and the surface. Experimentally, it can be challenging to achieve this quantification for both the upper and lower contact areas of the CLB simultaneously. This is because the camera is at an angle to avoid spurious light reflections and ensure optimal focus on the contact line between the bridge and the surfaces as shown in Fig. 6.5. If the bridge is assumed perfectly symmetrical, the data acquired at one extremity is sufficient. Here, however, we aimed to capture the information at both extremities to also quantify any impact of gravity, probe asymmetric bridges and evaluate the best experimental approach in light of the theoretical predictions. Practically, we found that the parameters derived do not vary within error between subsequent

extension/retraction cycles for a given CLB when taken at one given extremity. This was confirmed for each of the systems shown in Fig. 6.1. We therefore conducted measurements sequentially between the top and the bottom of the bridge by re-adjusting the camera wherever necessary.

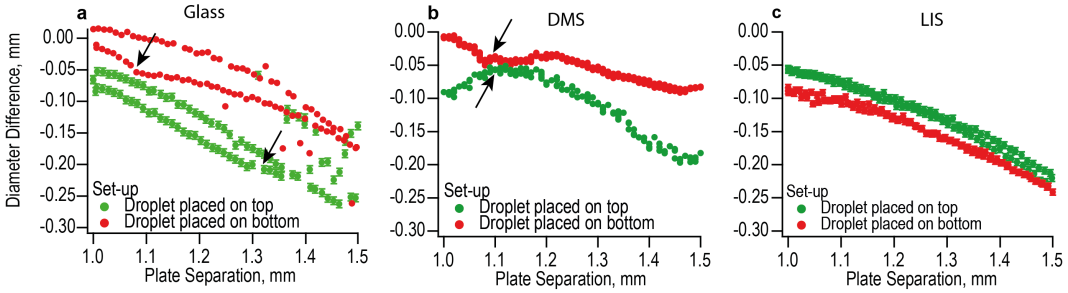

Figure 6.4: Pinning is important when setting up a liquid bridge. The placement of the droplet during set-up can affect the pinning behaviour during stretching. A 10 ul droplet placed on the top plate (red) or bottom plate(green) before forming a bridge with the other plate shows that the droplet preferentially interacts with the surface placed on before contact. The glass surface shows that when the droplet is initially placed on the top plate, the diameter can be initially larger than bottom plate. The curves also show features with shallow steps (arrows) which indicate pinning behaviours. On the LISs, we see that the curves are always smooth (indicating no pinning) and the diameter difference indicates that the droplet position at the start does not affect the final CLB performance. This behaviour is likely because placing the droplet on either the top or the bottom surface, forces the droplet into contact with the first surface and can lead to the droplet preferentially adhering to the first surface contacted. This leads to a larger starting diameter on the initial plate. Although the effect of gravity is the same for all CLBs, pinning can appear to reduce the effect of the gravity. This can cause the CLBs to have larger top radii than bottom radii, something which is unexpected when considering how gravity breaks the CLB symmetry.

From the evolution of CLBs' geometrical parameters (Fig. 6.6), it is possible to calculate the associated capillary force exerted by the bridge on the contacting surfaces using the equations presented in Chapter 1. Our setup also allows us to measure the force acting on the top surface directly, along the direction parallel to the main axis of the bridge (perpendicular to the surfaces). Figure 6.6 compares the calculated (Eq. 1.11) and measured force for each system, focusing on the top surface. The force acting on the bottom surface can be calculated from that derived for the top surface, taking into account gravity to deduce the 'bottom inferred force'

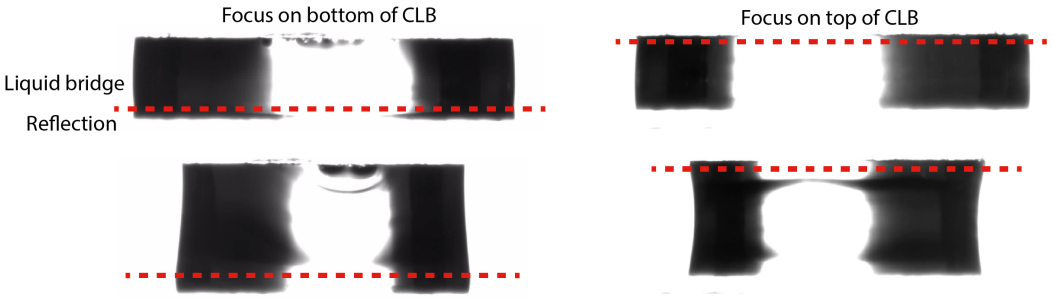

Figure 6.5: Due to the nature of the set-up design, it is challenging to simultaneously measure the top and bottom of the bridge and get a good view of both (assuming a 1 camera set-up). Instead, the camera needs to either focus on the top or the bottom of the bridge. For measurements that require information from both the top and bottom, then multiple stretches of the same droplet are required with some focusing on the top and some on the bottom of the bridge. It can be shown that the forces, CAs, curvatures etc do not evolve over the timescales of these experiments and remain constant. As shown in SI fig 2. In the above images taken on DMS, the bridge can be seen to have a reflection on either the top or bottom surface, a red line denotes the contact line of the bridge with the plate. This allows for an accurate detection of the bridge intersection with the plate, but means that often the part of the bridge which is not in focus is cut.

(Eq. 1.12), or directly calculated from the geometrical parameters measured at the interface between the CLB and the bottom surface, using the 'bottom calculated force' (Eq. 1.13). Generally, the forces measured on the top surface agree well with the top calculated force (Eq. 1.11) within error, including on LISs (Fig. 6.6a, c, e). This suggests that existing theoretical models, previously used for non-LISs, can be well adapted to predict the capillary forces on LISs, at least in the limit of the small oil ridge considered in this work. The magnitude of the capillary force, however, vary significantly between the different systems. On hydrophilic glass, the stronger interactions between the CLB liquid and the surface yield an absolute force value of $\sim$2mN with a variation of $\sim$ 1mN over an extension/retraction cycle. The absolute force magnitudes on the hydrophobic DMS and LIS are considerably smaller, and similar for both surfaces (in the order of 0.1 mN). However, the force variation over an extension/retraction cycle is five times larger for DMS than for

LIS (around 0.4 mN for DMS and only 0.06 mN for LISs), thanks to the frictionless LIS. On the Glass and on DMS surfaces occasional small deviations between the calculated and measured forces can be observed due to pinning. This is a result of data extraction from the experimental videos. The videos provide a 2D image of the CLB being extended, and pinned points can be missed from the analysis if not visible. A more detailed description of the analysis procedure can be found elsewhere[200].

6.2.2 The Effect of Gravity

Despite the overall good agreement between experiments and theoretical predictions (Fig. 6.6), a distinction can be made between comparison derived at the top surface (a, c, e) and at the bottom surface (b, d, f) where the data quality and the agreement with the theory is less accurate. To some extent this is expected, since the comparison is less direct than at the top surface. An additional problem comes from having to take into account the effect of gravity. While relatively straightforward in the theory, this complicates the measurements, especially on LISs. The CLBs used in this study are typically several millimetres wide for a height varying between 1 and 1.5 mm. For comparison, the capillary length of the bridge's glycerol solution is 2.39 mm (for pure water it is 2.7 mm). Gravitational effects must therefore be taken into account not only in terms of additional weight on the bottom surface, but also for its deformation of the CLB. The bond number shows that extended CLBs have a value between 0.1 and 0.4 (see Appendix A.3 for details of the calculations), indicating that gravity should be carefully considered in this CLB system.

The effect of gravity on the CLBs involving Glass and DMS surfaces can be seen by comparing the calculated forces on the bottom surface (Fig. 6.6b,d). The inferred and calculated bottom forces (Eq 1.12 and 1.13) are generally in good agreement within error. On LISs, however, things are more complicated. Firstly, the forces experienced by the LIS are considerably smaller than those on DMS or Glass and the relative measurement errors become inevitably larger. Secondly, the value of

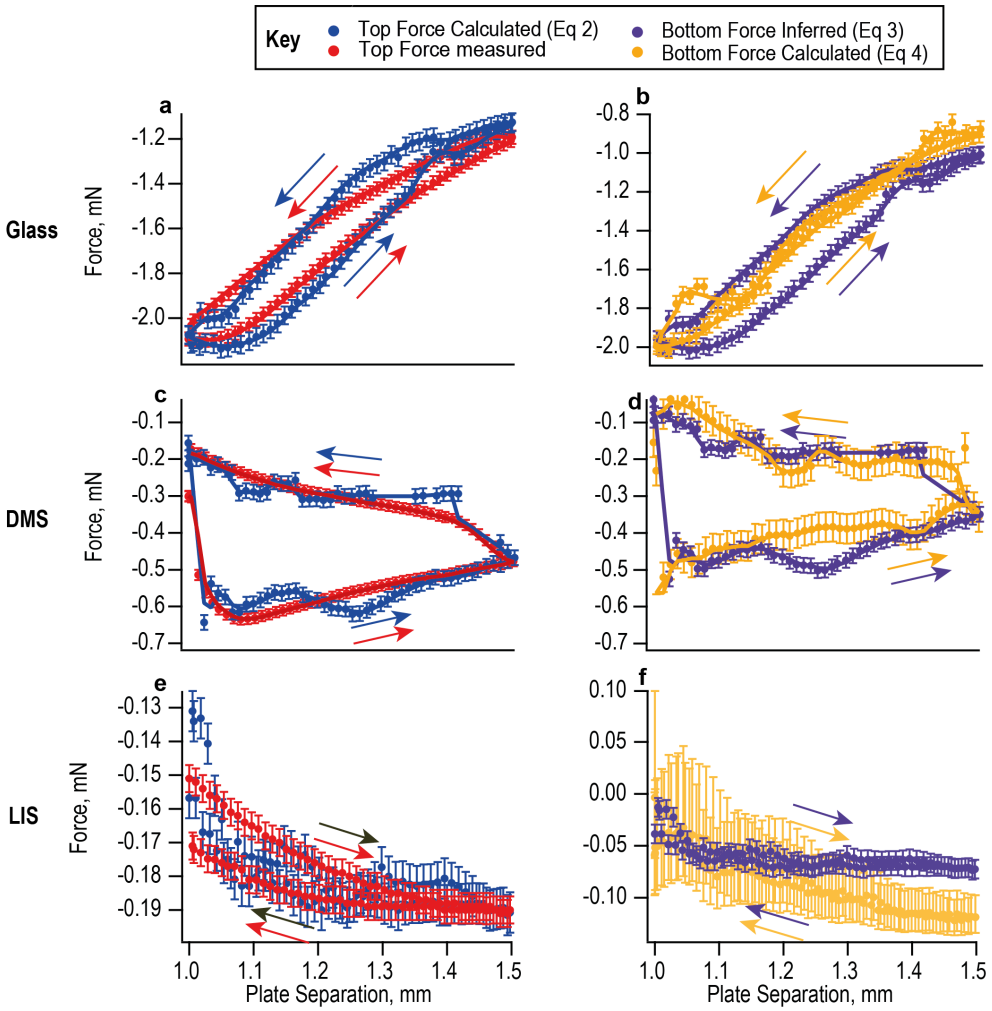

Figure 6.6: Comparison of the experimentally measured and calculated capillary forces exerted by CLBs on Glass (a,b), DMS (c,d) and LISs (d,e). The calculated force is obtained from the contact radius, bridge curvature and contact angle of the CLB and can be obtained separately for each surface (top or bottom). For the top surfaces the red and blue traces represent respectively the measured and top calculated force (Eq. 1.11). For the bottom surfaces, the purple and orange traces represent the bottom inferred and calculated force (Eqs.1.12 and 1.13 respectively). Small deviations from the measured values arise from pinning and occasional fitting difficulties with certain analysis frames. For Glass and DMS, we use a surface tension value of 67.4 mN/m [201] for the glycerol solution, while a surface tension of 50 ± 2 mN/m is used on LISs due to cloaking. This value is an average between a literature value [126] and an experimental measurement on a pendant drop analysed with Opendrop [123,124]. Errors represent the standard error.

the surface tension that should be used in the inferred and calculated bottom force equations (Eq.1.12 and 1.13) is not obvious since the CLB may be cloaked by the LIS oil. Cloaking is a known phenomenon in LIS systems [67,118,202] and occurs when the spreading coefficient of the oil over the bridge solution is positive [67]. Here, the spreading coefficient is estimated at ∼23 mN/m, suggesting the bridge to be fully cloaked by the LIS oil. However, our setup does not allow for direct observation or characterisation of the cloaking film or its thickness. This information would be needed for more accurate modelling since the surface tension of a cloaked liquid is known to change with cloaking thickness for thin films [203]. Instead, we experimentally measured the interfacial energy between the CLB solution and the oil using a pendant drop setup in conjunction with the Opendrop [123,124] software. We find a value of 48 mN/m, slightly below the literature value of 52.9 mN/m [126]. While relatively small, the difference is sufficient to affect the data significantly considering the small forces at play (around 20-25% of the force value). Finally, the cloaking may not be uniform and evolve over the course of an experiment, including possible oil transport between the two surfaces under gravity or through the bridge motion during extension. These effects cannot be addressed here.

Overall, surface tension is one of the largest sources of error when calculating capillary forces on systems using LISs. Significant errors can also arise from the need to evaluate the CLB curvature (R2), in particular close to the bottom surface where oil ridges can affect the measurement.

The effect of gravity can also be seen directly on the evolution of the CA formed by the CLB with the top and bottom surfaces. This is presented for each system in Fig. 6.7 with the red curves representing the CA on the top surface and the blue curves on the bottom surface. The glass surface shows CAs monotonically decreasing with extension, as expected from the contact line pinning and slip-stick motion. The top and bottom surfaces show similar angles with no obvious offset within error. A small offset should be present due to gravity acting on the contact line, but pinning obscures it.

The CAs evolution on DMS shows the hysteresis loop mentioned previously, with

both the top and bottom surfaces experiencing the same hysteresis within error (Fig. 6.7). In the case of the LIS, the CAs increase by 2-3 degrees as the bridge is extended, both on the top and bottom surfaces(Fig. 6.7c). The angles overlay on the outward and return and indicate no hysteresis or energy loss as a result of the CA change. However, a small ($\sim$2 degrees) but consistent offset exists between the apparent top and bottom contact angles. On LISs the CA can be affected by gravitational forces and by the size of the lubricant ridge. Deformation of the CLB under gravity causes the apparent CA to appear lower on the bottom plate. For a bridge of this size and height, the change in hydrostatic pressure between top and bottom is $\sim$6 mPa, enough to appreciably impact the contact line and the apparent CA. The same effect is likely to be at play on the glass and DMS systems but pinning effects at the contact line would make it difficult to observe.

Aside from the questions of CA offset and pinning, the fact that the CA on LIS increases upon CLB extension is fundamentally different from the evolution on the more standard surfaces. On LIS, the CA is no longer strictly a material parameter, but it depends on the pressure ratio in the droplet and in the lubricant: as the CLB is extended, the bridge Laplace pressure decreases. As a result, the apparent CA increases, consistent with previous theoretical predictions[31,204].

6.2.3 Asymmetrical Bridges

The results obtained so far show the evolution of CLBs in symmetrical systems of Glass, DMS and LISs. When the impact of gravity needs taking into consideration (LIS), the system ceased to be perfectly symmetrical, but the effects are subtle and the theoretical predictions remain valid within experimental error. To explore this further, we conducted experiments on systems asymmetric by design, with different surfaces at the top and bottom. However, to avoid one surface completely dominating the experiment, it is helpful to retain some similarity between the two surfaces. Here we do this by working with a system of DMS and LISs, with each surface either at the top or the bottom of the CLB. This asymmetric system is interesting because it represents a surface with no pinning, alongside a second

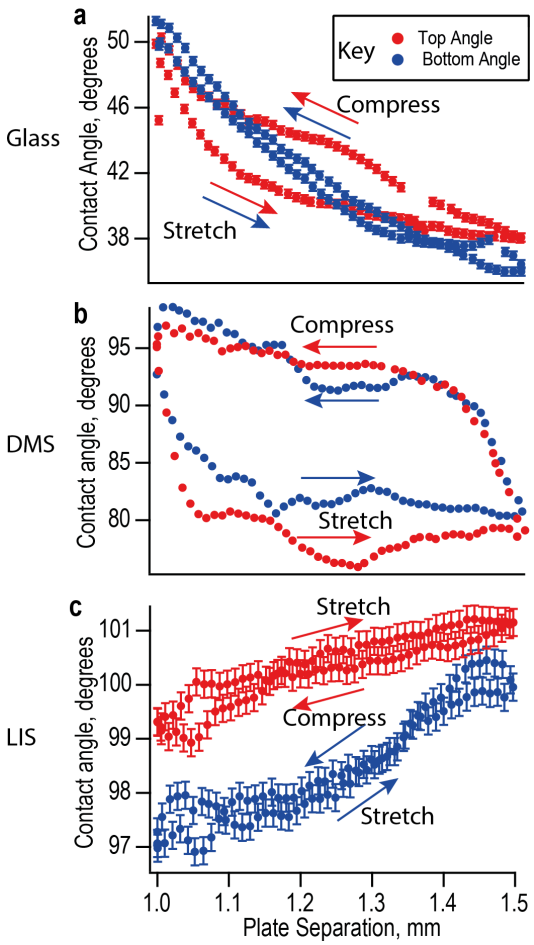

Figure 6.7: Showing how changes to the fitting region can change the measured value of the curvature. Blue curves represent the curvature measured close to the intersection with the top plate. Green curves represent the curvature measured close to the bottom plate (a) represents a curvature where half of the bridge is fitted to calculate the curvature and (b) represents a curvature where a quarter of the bridge is used to find the curvature. Errors on all curves represent 0.5 mm.

surface with similar contact angles but which experiences pinning. The results are shown comparatively in Fig. 6.8.

The CA measured on the LIS remains almost constant (98-100 degrees) regardless of whether the LIS is the top or bottom surface (Fig. 6.8a, red trace and Fig. 6.8b blue trace). The difference in contact angle between the two configurations is due to the deformation of the CLB under gravity, consistent with observations on the symmetric system (Fig. 6.6c). The evolution of the CA on the DMS

surfaces is however markedly different than the hysteresis loop observed for the symmetric DMS system. Instead, the 'loop' is elongated with monotonic changes in CA spanning larger absolute variations (Fig. 6.8a, blue trace and Fig. 6.8b red trace). This reflects the fact that the surface tension of the bridge has changed due to cloaking from its interaction with the LIS.

The radius of the contact area between the bridge and the surface changes by 0.5 mm at the interface with LISs with no hysteresis, and by <0.1 mm at the interface with DMS (Fig. 6.8c and d). As expected, the CLB preferentially slides across the LIS compared to the DMS surface where some pinning occurs.

When the LIS is at the bottom (and DMS at the top), the curvature of the CLB appear constant along the bridge, with similar values derived near to the top and bottom surfaces (Fig. 6.8e). Consistently, similar CAs are formed by the bridge with both surfaces at the start of the extension-retraction cycle (95 degrees with DMS and ∼98 degrees with LISs). The top DMS interface experiences only pinning while the bottom LIS interface only gravitational effects. The absence of gravitational effects at the top DMS interface, and the ability of the contact line to move easily at the bottom LIS interface, results in the DMS interface exhibiting a reduced CA hysteresis by comparison with a symmetrical DMS system. The bridge's capillary force also shows limited hysteresis, and an evolution reminiscent of the symmetric LIS system.

In contrast, when the LIS forms the top surface (Fig. 6.8e), a clear offset in curvature is observed between the top and bottom surfaces, with more than a 2 degree CA difference at the start of the cycle. In this configuration the DMS interface experiences both pinning and the increased hydrostatic pressure, whereas the top LIS interface experiences neither of these effects. The system is therefore more biased towards the DMS interface which completely dominates the CLB behaviour near the bottom surface: with a curvature remaining positive throughout the cycle and the capillary force exhibits significant hysteresis.

Comparison of the capillary forces measured, and inferred with the theoretical

predictions calculated from the CLB parameters, shows a good agreement (Fig. 6.8g, h). Overall, the changes in force are comparable to those measured for the symmetric LIS systems regardless of the configuration. This can be explained by a combination of two factors. Firstly, when a LIS is present in the system, the surface tension of the CLB drops from 67.4 mN/m[201] to 50 mN/m due to cloaking. Secondly, the LIS offers a non-pinning surface allowing a highly mobile contact line that will always move first to minimise the energy required to extend the bridge.

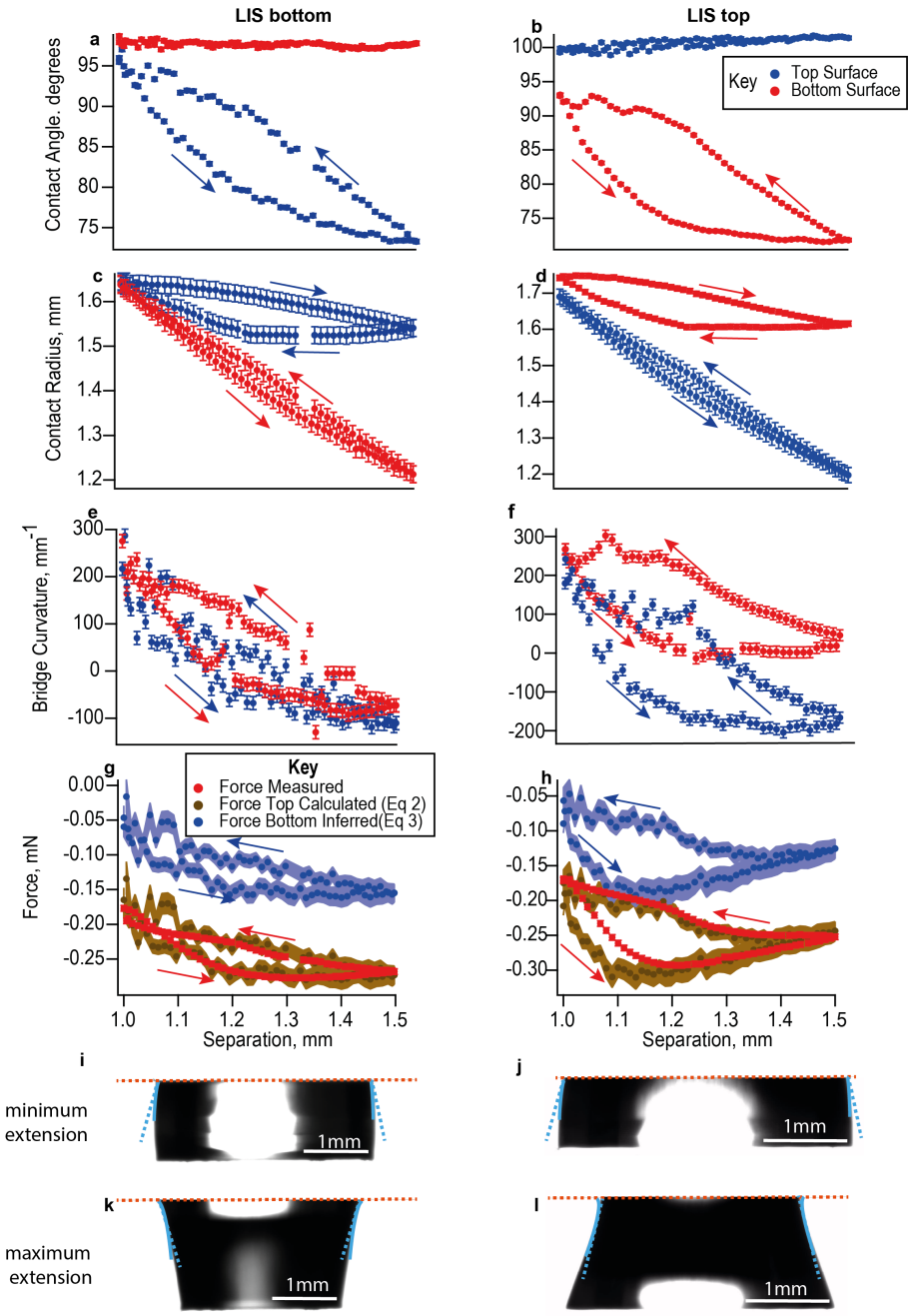

Figure 6.8: Comparative behaviour of asymmetric bridges with a LIS and DMS forming either the top or bottom surfaces over an extension-retraction cycle. In all cases, the top plate data is shown in blue and the bottom plate data shown in red. The evolution of the CA (a, b), the contact radii (c, d), the bridge curvature (e, f) and the capillary force (g, h) are shown comparatively within each case the data taken at the top and the bottom of the bridge. The CLBs can also be visualised at minimum (I, j) and maximum (k, l) extensions. The error bars in (a-h) represent the standard error.

6.3 Discussion and Conclusion

In this study the behaviour of CLBs as they are being extended and retracted was investigated. We compare CLBs formed by an aqueous glycerol solution bridging planar surfaces made of hydrophilic Glass, hydrophobic DMS and hydrophobic LISs. For symmetric systems, the results follow expected trends on non-LISs. At the interface with Glass, the CLB contact line exhibits a stick-slip behaviour which leads to a large but monotonic variation of CA upon extension of the bridge. The CLB curvatures are relatively high ($\sim$3000 mm^{-1}) as a result of the low CAs. The resulting capillary force is relatively large ($\sim$2 mN) due to the strong affinity of the bridge liquid for the Glass, but it shows little hysteresis. In contrast, CLBs between DMS surfaces exhibit significant CA hysteresis, with two clear plateaus observed for the advancing and receding angles. The behaviour is explained by an easier motion of the contact line along the hydrophobic surface, but still subject to pinning which dominates. The CLB curvatures are typically an order of magnitude smaller than with Glass ($\sim$300 mm^{-1}) due to the higher CAs, with both positive and negative curvatures values explored over a cycle. The resulting capillary force is also an order of magnitude lower than on Glass ($\sim$0.1 mN), but shows a clear hysteresis between the extension and retraction of the CLB. Experiments on LISs reveal an almost frictionless motion of the contact line with no visible hysteresis or pinning for CAs and contact radii variations. However, the CAs at the interface with LISs increase as the bridge extends due to the nature of the LIS when CA is no longer an intrinsic property of the system: as the CLB extends the Laplace pressure in the CLB decreases, leading to an increase in the apparent CA. The CLB curvatures are similar to those observed with DMS but remain consistently positive due to the lack of CA hysteresis. The same absence of hysteresis is also seen in the capillary force with variations less than five times smaller than for DMS. In all cases, the theoretical predictions match the experimental observations within error, although cloaking of the CLB needs to be taken into consideration for LISs.

Results on the LIS system also highlight the importance of gravity, a negligible contribution to systems with more 'standard' surfaces where force variations are

larger. Gravity acts to deform the CLB meniscus and increases the force on the bottom plate. This is particularly obvious for asymmetric systems comprising a DMS surface and a LIS at either the top or the bottom of the CLB. While in all cases, the CLB is cloaked and the CA are similar for both interfaces, the behaviour of the CLB is significantly different when the DMS is the top or the bottom surface (LIS bottom or top respectively). When DMS is at the bottom of the CLB, pinning is significantly more pronounced leading to different curvatures at the top and bottom of the bridge. The observed force profile and hysteresis also depends on the configuration with the DMS dominating the overall behaviour when at the bottom. This is rendered possible by the absence of pinning on the LIS, allowing the DMS to dominate the measurement.

Generally, comparing measurements and theoretical predictions is more challenging for CLBs involving LIS than for CLBs with standard surfaces. The direct effect of gravity can be taken into account, but more subtle effects such as cloaking or liquid transfer are more difficult to model accurately. Best agreement between experiment and theory is obtained when both probing the top interface of the CLBs, thereby bypassing gravity-related complications. This strategy was also found to help with the added difficulty of ridges formed by the LIS liquid on the CLB. Such ridges can obscure or change the measured CA due to changes in Laplace pressure in the CLB, rendering deduction of the bridge geometry more challenging. From a practical perspective, experimental force measurements on LISs can be challenging due to the high mobility of the droplets and the small force variations. Here a bespoke setup with enhanced sensitivity[200] was used. Keeping the experimental procedure consistent is crucial to minimise errors, controlling consistency of the measurements over several consecutive cycles. Another challenge of working with LISs is the cloaking and formation of oil ridges on the CLB by the lubricant.

Further work is needed to understand the interactions between the LIS lubricant and the CLB, in particular in relation to the changes in CAs as the bridge is extended, depending on the cloaking behaviour. This could be achieved theoretically with software such as Surface Evolver[205], previously used by Shek et al.[110] to model similar systems. Possible lubricant transfer at the surface of the CLB could

also be investigated using different viscosity lubricants linking up with previous work on droplet transfer [197]. Finally, more complex geometries could be explored, including with asymmetrical bridges. The present work illustrates some of the possibilities offered by asymmetrical bridges where a careful balance of interfacial properties can significantly change the system evolution only through the effect of gravity.

6.4 Experimental Methods in Chapter 6

6.4.1 Preparation of the surfaces

Standard Hydrophilic Surface

We selected glass as our reference hydrophilic surface for its routine use in CLB experiments and its importance in technological applications. Glass coverslips (25x25mm, VWR, Lutterworth, UK) were taken from a freshly opened box and used without further cleaning. Additional cleaning procedures such as with detergent or plasma can be used to render the glass surface more hydrophilic. However, such procedures tend to yield less reproducible results with CLBs, presumably due to an increased density of local surface defects and singularities. Such defects may be due to nanoscale local variations in the surface cleaning quality, activation of the surface or in the density of organics left behind. The typical root-mean square roughness of glass coverslips being $<$1nm [206], roughness effects can be neglected in our measurements.

Standard Hydrophobic Surface

Hydrophobic surfaces were obtained by functionalising clean glass coverslips with dichlorodimethylsilane. The preparation followed established protocols [121]. Briefly, the slides were immersed sequentially in acetone (purity 99% (Emplura©), Sigma-Aldrich-Merck, Gillingham, UK) and isopropanol (purity 99.8 %, Fisher Scientific,

Loughbrough, UK), and sonicated for 30 mins. They were then dried under a stream of nitrogen and allowed to air dry for 30 mins. The slides were then plasma cleaned for 10 mins (>30 W, VacuLAB-X, Tantec, UK) and further dehydrated in an oven at 100 °C for 60 mins. 1 ml of DMS was placed in an open dish in a desiccator along with the slides directly transferred from the oven. The desiccator was held under vacuum overnight to allow for vapor deposition of the DMS onto the slides. Slides were rinsed with acetone and ultrapure water, then dried overnight at 40 °C.

Liquid Infused Surfaces

Glass slides were prepared following a literature protocol as described in Chapter 2 and elsewhere[120]. In short, glass slides (Agar Scientific, 24mm) were first soaked in a solution of Decon-90 and ultrapure water. (18.2 MΩ, Merck-Millipore, Hertfordshire, UK). They were then rinsed and sonicated for bursts of 30 minutes in ultrapure water to remove any residual detergent. Slides were then allowed to air dry. Prior to coating, slides were rinsed with acetone (purity 99% (Emplura©), Sigma-Aaldrich-Merck, Gillingham, UK) and isopropanol (purity 99.8 %, Fisher Scientific, Loughbrough, UK) and dried under a stream of nitrogen. The slides were then further air dried for 30 minutes. Layers of nanoparticles were then applied to the surface using a liquid spray (GLACOTM spray, SOFT 99 Corp. Japan). Layers were left to dry for 60 minutes before the application of the next layer, until a total of 5 layers was applied. A silicone oil (20 cSt at 25 °C, Sigma-Aaldrich-Merck, Gillingham, UK) drop (500 μl) was then placed on the surface and spin coated immediately (2000 rpm 5 min, acceleration 300). The slides were used directly, or stored (with no oil coating) for a maximum of 2 weeks. Any storage was done in closed petri-dishes at ambient laboratory temperatures.

6.4.2 Measurement Procedure

The measurement procedure and equipment setup are as described in Chapter 5 or Ref. 191 [200]. To briefly summarise, the two surfaces under study are prepared using the protocols described above, then mounted onto a custom-built thin metal mount using fast curing, air dry glue (reprorubber thin pour, Bowers Group, Camberley, UK). The glue is given 2 hours to cure before the plate is mounted into the force sensor. The force sensor is the equilibrated for an hour before measurements are taken. A droplet (10 μl) is then placed onto the bottom surface, and gently brought into contact with the force sensor. The system is equilibrated for 2 minutes before the data is sampled. The bridge is then extended at a constant rate (extension phase) to a maximum extension of 0.5 mm from its starting position before being subsequently retracted (retraction phase) to its original position.

6.4.3 Measurement of the Surface Tension of the Different Liquids

The CLB measurements were conducted using an aqueous glycerol solution for the bridge (glycerol 80% in ultrapure water) to limit the impact of evaporation over time. Opendrop [123,124] was used to measure the surface tension of the silicon oil and the glycerol (80%) solution.

Chapter 7

Conclusions and Outlook

7.1 Conclusions

This thesis has investigated the behaviour of droplets and CLBs when placed on LISs. A variety of purely solid hydrophilic and hydrophobic surfaces are also investigated for comparison. LISs are designed to have excellent liquid repelling behaviour and as such have a number of desirable applications, such as anti-corrosion, anti-fouling, anti-icing and self-healing abilities. These desirable qualities also make LISs challenging to study, since the very qualities that make it highly liquid repellent also make the surface super slippery and hence the changes in geometry and forces experienced by the droplets and CLBs are small.

Chapter 3 looks at fabricating LISs to create the optimal model surface from widely used, inexpensive components. A rough porous layer, formed of 5 layers of NP spray was found to be optimal. This creates a porous network of approximately 1.6 μm layer which can be infused with a lubricant (here silicone oil). The surface roughness of the 5 layers of NPs is around 45 $\pm$ 5 nm. A DMS-functionalised glass slide was also fabricated as a comparison which has a roughness around 9 $\pm$ 1 nm. The CA measured on the NP and DMS-functionalised surfaces changes upon infusion with oil. For NP-LISs this reduces the CA from $\sim$150° to $\sim$101° and the DMS-functionalised surfaces increase from $\sim$95° to $\sim$101°. Since both

surfaces are exposing the ambient fluid to silicone oil of a similar thickness, it is expected that the CAs should be the same for both surfaces. The measured CAs are in agreement with the prediction based on the Youngs equation which predicts the CA to be $\sim 104^\circ \pm 2^\circ$. Oil loss was found to be minimal for both NP and DMS functionlised surfaces over the experimental timescales, making these surfaces suitable for characterisation and ageing experiments performed in Chapter 4. Creating a model system that is well characterised is important, since this baseline may change under external conditions. Understanding the basic variability allows the environmental/mechanical effects to be separated from those arising from fabrication, and hence allows for comparisons between different substrates.

The model surfaces created in Chapter 2 and 3 are then subjected to ageing processes aimed at mimicking the evolution of LISs in more realistic conditions. The experiments performed used a dual micro- and macroscale experimental strategy, where functional changes in the LISs performance were linked to specific oil loss mechanisms and nanoscale effects in the porous layer. It was found that the initial oil layer was not at equilibrium, leading to significant oil loss, even when stored under ambient conditions and without any external perturbation. When immersed in aqueous solutions and exposed to high intensity ultrasonic pressure waves, the oil loss significantly accelerates, inducing changes in the CA and CAH. The pressure waves create aqueous micro-droplets in the oil layer, progressively pinching out the oil from the LIS, as cloaked droplets move out of the oil phase back into the bulk aqueous solution. The rapidity of the depletion process is weakly dependent on the colloidal stability of the micro-droplets. This mechanism appears central to the ageing of the LIS exposed to the impact of waves. In the simple model LIS (created in Chapter 4), this "pinching" mechanism induces an important side effect: the irreversible degradation of the hydrophobic NP coating used to retain the infusing liquid. The NP coating plays an important role in the LIS performance, which is maintained more than ten times longer for the nanoporous NP-coated supports compared to the smooth flat supports. However, the current findings highlight inherent weaknesses in the use of facile nano-structured NP coating; exposure of the LIS support to the aqueous solution causes both chemical and structural degra-

dations. This work could act as a reference point for future work involving the testing of new LIS applications, in particular the development of a standardized, accelerated ageing strategy, to determine the robustness and durability of novel products.

The forces experienced by CLBs on LISs were then studied compared to two other non-LISs surfaces. LISs can be challenging to study, since the forces measured on LISs are comparatively small. Chapter 5 solves this by designing a setup and analysis code capable of taking integrated measurements of all variables, measuring changes in forces with high sensitivity and software capable of extracting the relevant parameters from the experimental data. The force measurement is sensitive enough to quantify the small force variations associated with experiments on LISs and could also be used to probe force variations associated with smaller liquid bridge deformations on conventional surfaces. The data can then be processed to high temporal accuracy with up to 20 images per second and 10 force sensor readings per second. The system has motorized stages that can move in all three direction (x, y and z) and the stages position can be controlled with 0.1 μm accuracy if necessary. The isolation of the setup in a perspex box allows for control of the local environment around the CLB (e.g. humidity or temperature). The system designed here is not limited to the simple stretching experiments shown here but can also perform shearing experiments (see future work section), or their combinations thereof. It could also be used to stretch bridges to larger separations, or to stretch different materials such as fibres.

CLBs are commonly found in nature and in many industrial processes. They are present at different length scales, from nanoscale AFM experiments to millimetre-scale liquid bridges formed between plates. Chapter 6 demonstrates the behaviours of capillary liquid bridges on different hydrophobic and hydrophilic surfaces, which builds on the initial data captured in Chapter 5. The stretching and compressing behaviours of CLBs on hydrophobic and hydrophilic substrates were compared. Importantly, hydrophobic surfaces that have pinning and no pinning were also compared. It is found that the forces on LISs are much smaller than those on conventional hydrophobic and hydrophilic surfaces due to the frictionless surface they

present. The lack of pinning also leads to little hysteresis in the force-separation curves. Glass and hydrophobised glass experience pinning and CAH, which lead to hysteresis in the force-separation curves as seen in other literature studies [98,103]. They also lead to larger measured forces. Due to the droplet size studied and the small capillary forces measured on LISs, gravitational forces are important in this work. Capturing the gravitational contribution was carefully considered, due to the difficulties in simultaneously measuring the geometrical parameters at the top and bottom plate. It was also found that interactions of the lubricant layer with the CLB on LISs lead to changes in the measured contact angle. This lubricant-CLB interaction may have more pronounced impact under different fabrication or stretching conditions and should be studied further. There is a possibility of expanding this work (using this similar setup) to include LIS fabricated from different materials, or to stretch the bridges further to determine their stability on LIS.

Altogether, this work looked to answer a number of questions. Firstly, to understand how LISs age. As well as discovering a new ageing mechanism, whereby water enters the lubricant layer as a micro-emulsion, there is a growing body of evidence that water can also nucleate at the oil-solid interface [207]. This occurs due to water dissolving into the oil layer after soaking and spontaneously nucleating at the interface. In terms of wider implications for LISs, this itself is extremely important. Since water is likely to come into contact with the porous layer, any application for LISs which requires the surface to be submerged (eg. antifouling coatings for boats) should consider the possibility of degradation due to the ingress of water (whether through diffusion or through ageing processes). These processes would both speed up oil loss on the LIS, reducing the surfaces useful lifetime. There are still a large number of open questions on ageing. Would it be sufficient to make a porous structure that was more robust against solution based degradation? Is there a better way to make the porous structure such that the oil is more resistant to shedding? In high humidity environments (such as tropical locations) would water enter the oil layer or condense on the surface? Is submersion in solution required?

Secondly, there is the question of whether current models are suitable for characterising forces on LISs. Current models have been found to characterise CLBs on

LISs. One key question that remains is the cloaking of the CLB with the LIS lubricant. Cloaking is important for considering LISs applications, since it depletes the oil layer through cloaked CLBs taking lubricant away as they are shed. It also changes the surface tension of the CLB which impacts factors such as bridge stability and shape. These factors are important in many industrial processes, for example in inkjet printing, where controlling the shape/stability of the CLB is important to improve the print resolution [208].

Thirdly, the pinning and wetting behaviours of different hydrophobic and hydrophilic substrates are considered. Pinning leads to hysteresis in the system, which indicates energy loss. In terms of industrial processes, or cleaning, using LISs requires the least amount of energy when manipulating CLBs or droplets. Although not considered here, using combinations of hydrophobic and LISs might also offer a method of droplet transport, since the CLBs preferentially stay on the hydrophobic surface and not the LIS when in asymmetric bridge configurations, similar to the work of Nath et al [197] who used LISs with two different viscosity oils for a similar purpose.

In conclusion, the work conducted in this PhD provides novel insights into the wetting behaviour of droplets and capillary liquid bridges involving LISs, helping to better understand ageing effects on LISs, capillary forces, pinning and CAH on hydrophobic and hydrophilic surfaces, and cloaking phenomena. The findings also highlight some important and pressing questions regarding LIS technology as well as fundamental aspects such as cloaking or oil loss mechanisms. The next section examine some of these questions in the light of the work presented here, proposing specific lines of inquiry.

7.2 Outlook and Future Work

Building on the works in this thesis, here I discuss several key questions worthy of further investigations.

7.2.1 Changing the Fabrication Materials

The experiments in this thesis focused on one model LIS, but could equally have been expanded to use other LIS fabrication methods and materials. One of the key reasons for surface degradation during the ageing (Chapter 4) is the interaction of the porous substrate with the ambient liquid environment (here saline or pure water solutions). This was due to two mechanisms; the depletion of the lubricant layer, and through the pressure waves creating micro-droplets which can interact with the substrate (or are forced into contact with it). Depletion is due to fluid flows and surface agitation, as well as due to the micro-droplets in the lubricant layer pinching off and carrying a cloak of oil away. The creation of an emulsion in the lubricant layer may contribute to the surface damage, even though a layer of oil remains on the substrate.

To counteract these two ageing mechanisms it is necessary to increase the stability of the oil layer, and also to stabilise the porous support against solution based damage. Both these strategies help to prevent lubricant depletion to allow the LIS to retain its slippery properties. Using a support that does not require chemical functionalisation (unlike the NP here) would be an option to limit LIS degradation and would ultimately increase the lifetime of the LIS. These supports would need to be equally as easy to prepare and uniform as the NP ones. One such surface, the preliminary result of which is shown in Fig. 7.1 may offer a solution. Silica beads are deposited on a silicon wafer to create a uniform porous network (Fig. 7.1 shows these beads deposited but not sintered). The beads would then be sintered to the surface to create a well attached layer before being immersed in lubricant. This method comes with limitations in scaling the sample size. However, for small scale experimental work looking at lubricant losses and more fundamental physics, it would be suitable. This design would require a great deal of fine tuning to work out the optimum NP concentration for deposition and heating ramps for furnace sintering work. The sintering may also lead to changes in the silica bead properties due to heating at high temperatures.

Lubricant layer thickness, viscosity[18,83,142,210] and its application mechanisms

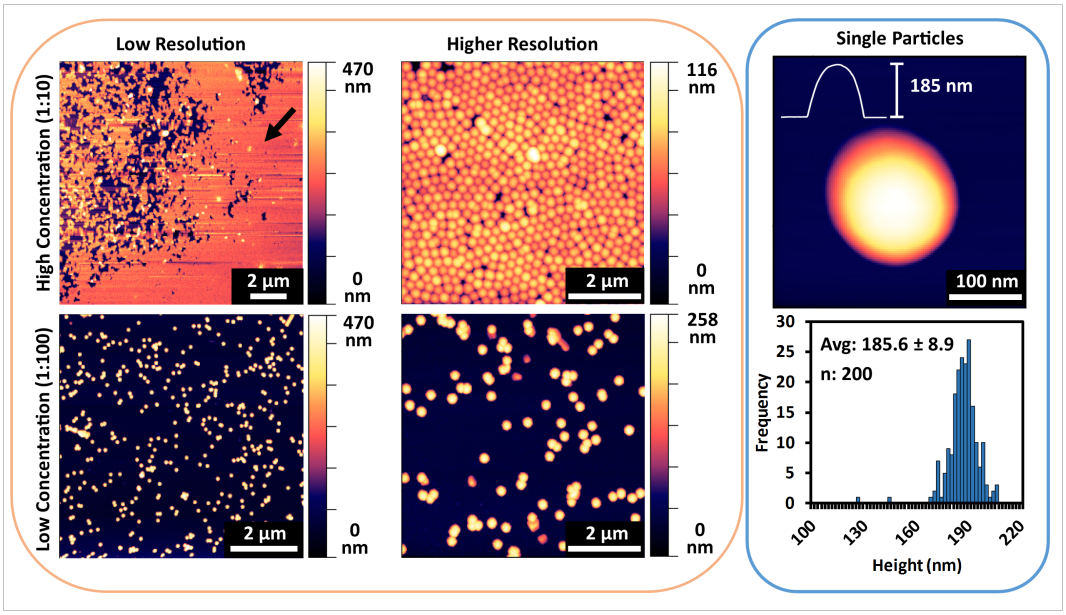

Figure 7.1: An alternative surface may be made from silica beads that are sintered. In this image, a simple deposition experiment is performed to determine how the beads would be placed on the surface prior to sintering. When doing this, we were following a paper by Ling et al [209]. Two concentrations of silica bead solutions are shown alongside low and high resolution images of the beads placed on the surface. The beads are around 200 nm in diameter, as shown by the single bead image and the accompanying histogram. In terms of creating a porous surface, layers such as those found in the high concentration solution could be formed and then sintered to adhere the beads permanently to the surface. This structure, unlike the chemically modified ones, would be resistant to any damage caused by liquid incursion into the oil layer. *Image reproduced with permission from Aaron Elbourne, RMIT University, Australia.*

(spin coating, immersion, dip coating etc) [18] also affect LIS performance. In this study, the fabrication methods were kept constant (spin coating slides to 6-8um oil layer thickness). In general, higher viscosity lubricants deplete from the surface more slowly [210] and resist abrasion better than lower viscosity lubricants but with the caveat that the mobility of surface fouling is reduced/sheds more slowly. However, this is dependent on the viscosity ratio (the ratio of the viscosity of the working liquid over that of the infused liquid). Lower viscosity oils have been shown to have higher retention when exposed to shear flows [83] if the viscosity ratio is high. This again indicates that depending on the conditions the surface will be exposed

to (e.g. air or liquid and the type of wear), the lubricant should be appropriately chosen. Viscosity will also impact the critical lubricant layer thickness required to maintain the self-healing LIS properties [142] which increases with increasing oil viscosity. A series of experiments that look at varying the oil viscosity and thickness using this new porous substrate, and measure its depletion would be instructive and may lead to a different choice of materials in the future.

7.2.2 Lubricant-Bridge Interactions

Another question that was apparent in this research is the lubricant cloaking of the CLB, and how this changed the surface tension it. However, there were certain difficulties in measuring the surface tension and certain assumptions had to be made about its effect and thickness since it was not visible to the cameras used. Cloaking can offer stability to liquid droplets [211] and may also stabilise CLBs when stretching [111]. Working with a none cloaking lubricant would allow experiments to verify the impact of cloaked bridges versus uncloaked bridges. One particularly interesting experiment would be to continue to stretch the bridges, to see if on LISs, the oil would displace some of the glycerol at the bridge centre to form a binary CLB as observed for Petkov et al. [111]. In their experiment, a binary/sandwich type bridge forms as oil fills the space of the glycerol to ensure the CLB does not rupture. A related envelopment instability has also been identified at small separations for modelled LISs [110]. This would be interesting as it would lead to the creation of more stable CLBs over shorter and longer stretching distances.

Due to the cloaking of the liquid bridge, the top and bottom LISs were connected together by a thin film of oil. It may be possible that this created a flow of oil between the two plates. Flows of liquids, acting against gravity have been found to stabilise some CLBs [212,213]. Changing the oil layer thickness of the top and bottom plate, may allow the direction of the flow of oil to be controlled, assuming that the oil layer will seek to equilibrate the thickness over both plates.

Another understudied aspect in this thesis is the relationship between the oil layer

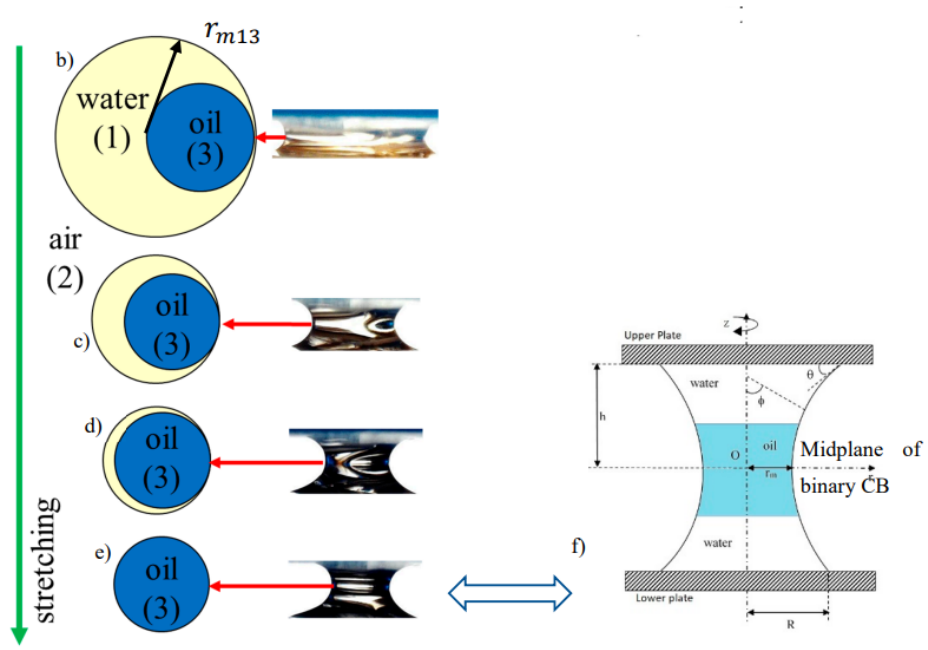

Figure 7.2: A binary type bridge is stretched leading to the oil displacing the water to prevent bridge rupture. On LISs where the oil is known to cloak the liquid bridges, it may be interesting to study the lubricant-CLB dynamics to determine whether the oil has a similar stabilising effect. *Figure reproduced with permission from Petkov, P.V.; Radoev, B. Investigation of Single and Binary of "Sandwich" Type Convex Liquid Capillary Bridges, Stretched between Two Flat Surfaces (Experimental Approach). Colloids Interfaces 2019, 3, 68. https://doi.org/10.3390/colloids3040068. Copywrite MDPI 2019.*

and the contact angle experienced by LISs. As seen in Chapter 6, the CA increases as the bridge is stretched. This was not as a result of pinning, but most likely a result of the lubricant ridge pulling on the CLB as it moved. At higher velocities this effect should become more pronounced, similarly if a more viscous lubricant were used, the meniscus should be more deformed. As well as conducting further experiments, modelling could be used to verify this effect. The Surface Evolver[205], which is discussed in further detail in Appendix A.4, may provide a suitable solution.

7.2.3 Shearing CLBs

The set-up created in Chapter 5 is capable of performing shearing experiments as well as stretching. Preliminary experiments shown in Fig. 7.3 show that the shearing forces were very small for this particular set-up (0.5 mm separation, 5 ul CLB), but this avenue could be explored using different conditions (e.g. using larger droplets, pure glycerol solutions, smaller separations, etc) to get a larger force to measure. Shearing experiments on LISs are more challenging than stretching ones, because the shearing motion causes the bridge to slide around, leading the CLB to be out of focus, out of frame, or reaching the edge of the sample (where there are sometimes defects/edge effects). Extending the plate length and the frame of view can help to counteract the lateral sliding effects. Another possibility might be to have an asymmetric bridge, whereby one surface is pinned (similar to the asymmetric bridge experiments in Chapter 6) and the other surface is the LIS. This changes the properties of the bridge, but would make measurements simpler.

Shearing CLBs on substrates can give information on many phenomena, such as adhesion, friction, and stick-slip behaviours which are important for many tribology studies. Shearing studies may complement and build on work that looks at sliding droplets on LISs[68,116] and other surfaces[214,215]. It may also help to investigate whether droplets or CLBs are sliding, rolling or tank-treading as they move across the surface under different conditions.

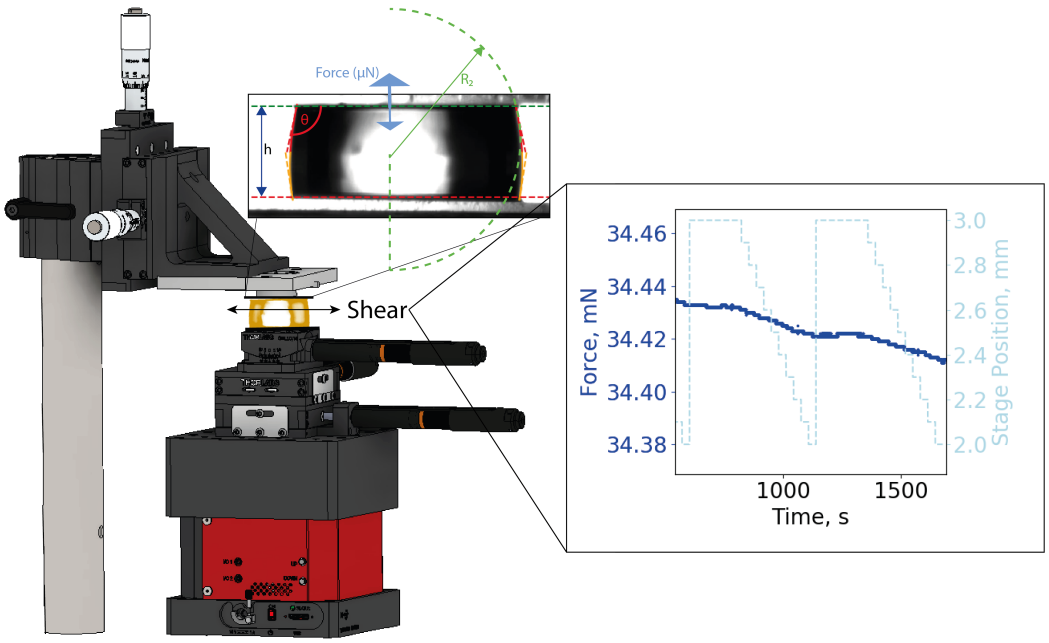

Figure 7.3: The setup for this experiment is shown alongside a preliminary experiment. The experimental setup is similar to stretching experiments in Chapter 6 but instead uses a lateral stage to shear the liquid bridge. The forces experienced by LISs when shearing are relatively small for this particular setup (0.5 mm separation, 5 ul, water CLB). The droplet is slowly sheared at 0.005 mm/s before being returned to its original position. The droplet is also sliding predominantly to the right as the measurement takes place. This suggests another external factor (such as a slightly tilted plate) is influencing the measurement.

Appendix A

Analysis Code

A.1 LabVIEW Code

A.1.1 Camera Control

'Camera Control' LabVIEW script: This script was written to control a Dino lite AM7915MZT – EDGE or a High sensitivity Digital camera UI-3880CP-M-GL Rev.2 by changing the camera in the drop down list. It is partially modified from labview example 'grab and save to avi'. The variables in the script are detailed in Table I. A block diagram for the code is shown in Figure A.1.

A.1.2 Force Sensor Control

'Force Sensor Control' LabVIEW script: This script was written to control a F329 Deci-Newton Loadcell attached to DSC USB Loadcell Digitizer (to increase signal). For this instrument, changes to parameters, eg the number of readings per second, must be changed in the devices own software (here DSCUSB toolkit). The code used is modified from LabVIEW example 'continuous serial for write and read' for a serial instrument. The code was set to write the data to file. A block diagram of the code is shown in Figure A.2.

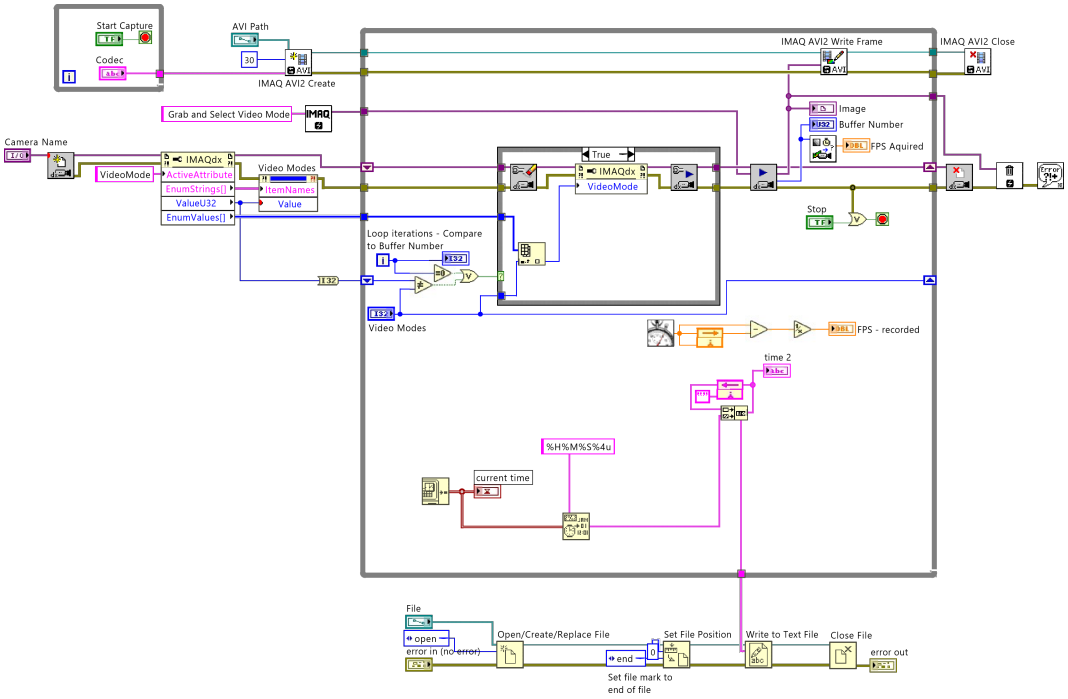

Figure A.1: A block diagram of the LabVIEW code 'camera control'.

Variable	Control Value
Camera Name	The camera you wish to use
Video Modes	Choose the number of frames and the number of pixels for imaging
Buffer number/loop iterations	Compare these two values to make sure that the program does not drop frames while saving.

Table A.2: A table of variables found in the camera control labview script.

A.1.3 Stage Control

'Stage Control' Labview script: This script was written to control the motion of a Thorlabs KVS30/M - Kinesis 30 mm Vertical Translation Stage. There are a number of variables: detailed in the Table II below that can be changed to modify

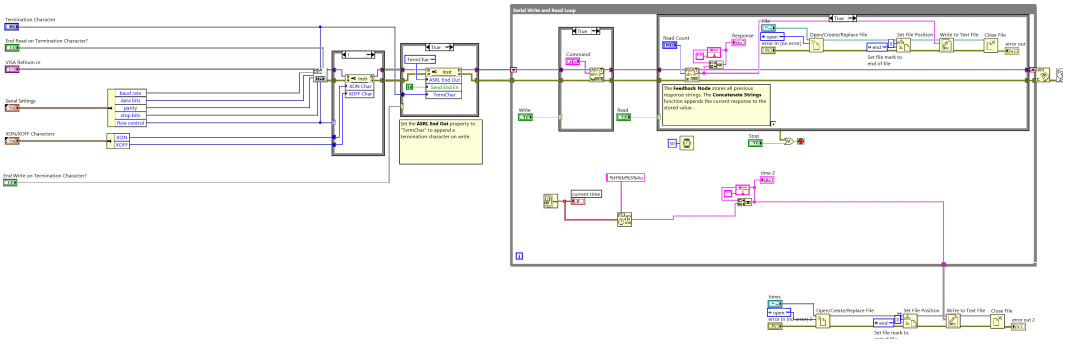

Figure A.2: A block diagram of the LabVIEW code 'Force sensor control'

the behaviour or stepping motion of the stage. A block diagram of the code is shown in Figure A.3.

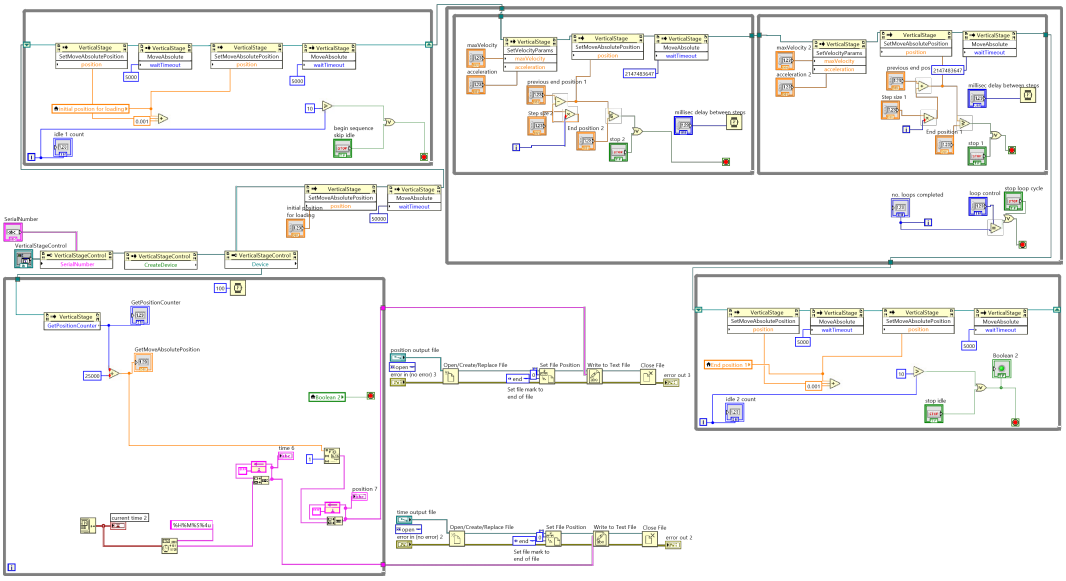

Figure A.3: A block diagram of the LabVIEW code 'Stage control'.

Variable	Control Value
MaxVel/MaxVel2	The velocity that the stage shall travel at in the forward/backward motion
Acceceleration/acceleration2	The maximum accerleration of the stages in the forward/backward motion.
Initial position for loading	The stage loading position (for liquid bridge).
Prev end pos1/prev end pos	The starting position and the ending position of the stage.
Step size/step size1	The size of step the stage should take in the forward/backward motion.
End position/end pos1	The end position of the stage in the forward/backward motion.
Milisec delay/milisec delay1	If you want a short wait time in between steps in the forward/backward motion.
Loop control	How many times the stage should repeat the forward/backward motion.
SerialNumber	The serial number of the device used.

Table A.4: A table of variables found in the stage control script.

A.2 Python Analysis Code

A.2.1 Extraction of Parameters (Simple Video)

'Extract data from simple video' was designed to extract CA, Radii (contact radius and radius of curvature) and bridge heights from a capillary liquid bridge video. It is assumed that the liquid bridge occupies at minimum 200 pixels for accurate fitting. The user is asked to provide information about several video parameters, which are detailed in table IV which are used to track the droplet motion. To

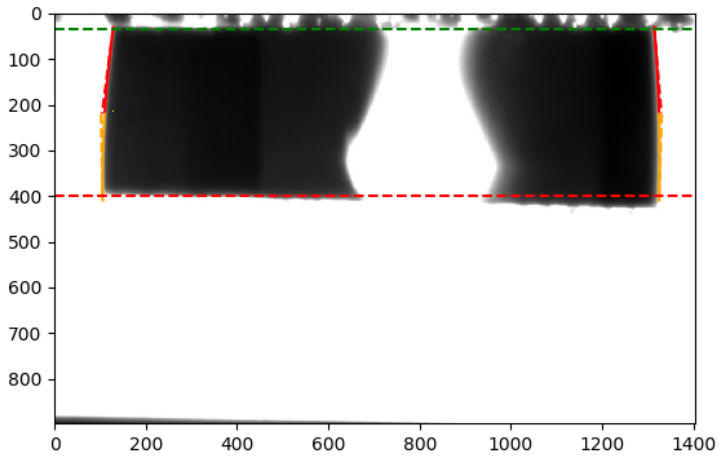

Figure A.4: The stretching of a liquid bridge between two hydrophobized (DMS) glass plates. The image displays good fitting to the liquid bridge edge, in particular for the red curves where the data is extracted (top plate). Any occasional poor fitting can be filtered during post processing of videos. The bottom of the bridge is partially obscured by the spherical plate meaning that if any data is required from the bottom plate, the camera must be repositioned to focus on this surface.

summarise the script briefly. The user is asked to provide information about the video motion and is then asked for a video file. This video file is split into individual frames for analysis and then the frames analyzed in turn. Each frame is first turned into a black and white image before passing to the canny edge detector. The edges of the droplet are found and the droplet edge is converted into an array of points. The user is then asked for the region they want to fit to the droplet (ie, which part of the array is your data) and where the droplet is approximately so that the left

and right sides of the droplet can be distinguished. These select points split into 4 quadrants and are then fitted to a second order polynomial. These four quadrants represent the droplet at the top left, bottom left and the top right and bottom right as shown in Figure A.4. The user then defines the starting top and bottom of the droplet (before motion). The top most point is used to calculate all the variables such as the CA and Radii but this can be changed by the user. Details of these calculation can be found in Chapter 5. The extracted frames, canny edge detection frames and frames fitted to the polynomial are saved for the user to view. All calculated variables are stored in text files and saved. The code is displayed below.

```
"""
Created on Fri Feb 22 15:01:00 2019

@author: Sarah Goodband (lpps65)
"""
#write down any notes here about the video




#import necessary functions
    ↪ ------------------------------------------------
import cv2
import numpy as np
from matplotlib import pyplot as plt
from PIL import Image
import glob
import math
import shapely.geometry as SG
from shapely.ops import linemerge
import os
```

Variable	Control Value
m1	The frame in which the CLB motion begins.
d_c	The frame in which the CLB motion begins.
s1	Compare these two values to make sure that the program does not drop frames while saving.
e1	The number of frames in the video.
step size	The number of pixels moved each bridge step.
vid_cap	The video under analysis
y_range	The array that you want to fit your polynomial to
y_fit	The area you want to be fitted by your polynomial
bottom	The known starting position of CLB in pixels
top	The top of the CLB in pixels

Table A.6: A table of variables found in the 'extract data from a simple video' script.

```
import scipy.optimize
import matplotlib.style



#some code to define finding intersections
```

```
def _rect_inter_inner(x1,x2):
    n1=x1.shape[0]-1
    n2=x2.shape[0]-1
    X1=np.c_[x1[:-1],x1[1:]]
    X2=np.c_[x2[:-1],x2[1:]]
    S1=np.tile(X1.min(axis=1),(n2,1)).T
    S2=np.tile(X2.max(axis=1),(n1,1))
    S3=np.tile(X1.max(axis=1),(n2,1)).T
    S4=np.tile(X2.min(axis=1),(n1,1))
    return S1,S2,S3,S4


def _rectangle_intersection_(x1,y1,x2,y2):
    S1,S2,S3,S4=_rect_inter_inner(x1,x2)
    S5,S6,S7,S8=_rect_inter_inner(y1,y2)

    C1=np.less_equal(S1,S2)
    C2=np.greater_equal(S3,S4)
    C3=np.less_equal(S5,S6)
    C4=np.greater_equal(S7,S8)

    ii,jj=np.nonzero(C1 & C2 & C3 & C4)
    return ii,jj


#Computes the (x,y) locations where two curves intersect. The curves
    ↪ can be broken with NaNs or have vertical segments.
def intersection(x1,y1,x2,y2):
    ii,jj=_rectangle_intersection_(x1,y1,x2,y2)
    n=len(ii)

    dxy1=np.diff(np.c_[x1,y1],axis=0)
    dxy2=np.diff(np.c_[x2,y2],axis=0)
```

```
    T=np.zeros((4,n))
    AA=np.zeros((4,4,n))
    AA[0:2,2,:]=-1
    AA[2:4,3,:]=-1
    AA[0::2,0,:]=dxy1[ii,:].T
    AA[1::2,1,:]=dxy2[jj,:].T

    BB=np.zeros((4,n))
    BB[0,:]=-x1[ii].ravel()
    BB[1,:]=-x2[jj].ravel()
    BB[2,:]=-y1[ii].ravel()
    BB[3,:]=-y2[jj].ravel()

    for i in range(n):
        try:
            T[:,i]=np.linalg.solve(AA[:,:,i],BB[:,i])
        except:
            T[:,i]=np.NaN


    in_range= (T[0,:] >=0) & (T[1,:] >=0) & (T[0,:] <=1) & (T[1,:]
        ↪ <=1)

    xy0=T[2:,in_range]
    xy0=xy0.T
    return xy0[:,0],xy0[:,1]

#here are some arrays to store numbers in

left_angles_t = []
```

```
right_angles_t = []
left_angles_b = []
right_angles_b = []
frame_no = 0
min_b = []
min_t = []
r1_pos_t = []
r1_pos_b = []
intersect_left_xt = []
intersect_left_yt = []
intersect_left_xb = []
intersect_left_yb = []
intersect_right_xt = []
intersect_right_yt = []
intersect_right_xb = []
intersect_right_yb = []
R2_t_l = []
R2_b_l = []
R2_t_r = []
R2_b_r = []
rad_top = []
rad_bottom = []
rad_largest = []
R2_arcs = []



#give the program some information to calculate where the bridge is
    ↪ ----------------------------change me to fit
#motion begins at
m1 = 5
#direction changes
```

```
d_c = 35
# stops
s1 = 66
#video ends at
e1 = 1000

#so make list to make our adding array to track motion
list1 = [0] * m1
list2 = [0] * (e1-s1)
step_size = 5



forward = np.arange(1, (d_c - m1+1), 1)
for1 = []

for i in forward:
    for1.append(i*step_size)
    #for1.append(i*step_size)
    #for1.append(i*step_size)

backward = np.arange(1, (s1 - d_c), 1)
back1 = []
for i in backward:
    back1.append((d_c-m1)*step_size - i*step_size)
    #back1.append((d_c-m1)*step_size - i*step_size)
    #back1.append((d_c-m1)*step_size - i*step_size)
print (list1)

master_list = []
total_list = master_list + list1 + for1 + back1 + for1 + back1 +
    ↪ for1 + back1 +for1 + back1 +for1 + back1 +for1 + back1 +list2
```

```
print (total_list)
print (len(total_list))

#take the video you want
vidcap = cv2.VideoCapture('camera_times_11.avi') #
    ↪ ----------------------------------------the video you want
    ↪ to analyse
success,image = vidcap.read()
count = 0
while success:
  cv2.imwrite("frame_saves\\frame%d.tif" % count, image) # save
      ↪ frame as TIF file
  success,image = vidcap.read()
  print('Read a new frame: ', success)
  #print (count)
  count += 1

#do something to everyframe in video
filenames = sorted(glob.glob('frame_saves\\frame*.tif'), key=os.path
    ↪ .getmtime)
count = 1
for f in filenames:
    print(f)
    img = cv2.imread(f, 0)
    edges = cv2.Canny(img,50,150) #was 300
    cv2.imwrite('frame_saves_edges\\cannyframe%d.tif' % count, edges
        ↪ )
    count += 1

filenames_1 = sorted(glob.glob('frame_saves_edges\\cannyframe*.tif')
    ↪ , key=os.path.getmtime)
```

```
counter1 = 0
for f in filenames_1:
    print (f)
    print ('counter', counter1)
    #the canny image does not make image black and white - so must
        ↪ threashold-----
    #Pixels higher than this will be 1. Otherwise 0.
    THRESHOLD_VALUE = 200
    #Load image and convert to greyscale
    try:
        original = Image.open(filenames[counter1])
    except IndexError:
        break
    img = Image.open(f)
    img = img.convert("L")
    imgData = np.asarray(img)
    thresholdedData = (imgData > THRESHOLD_VALUE) * 1.0
    #now show the data if you want?
    '''plt.imshow(img,cmap = 'gray')
    plt.title('Original Image'), plt.xticks([]), plt.yticks([])
    plt.imshow(thresholdedData,cmap = 'gray')
    plt.title('threshold data Image'), plt.xticks([]), plt.yticks
        ↪ ([])
    plt.show()'''

    #section finished - lets just check
    print ('finished section')

    #get the set of coordinates from the thresholded image
        ↪ ------------------------
    indices = np.where(thresholdedData == [1])
```

```
#print (indices)
coordinates = zip(indices[0], indices[1])


co_ords = np.asarray(coordinates)
#print (co_ords)
y_ords =indices[0]
x_ords = indices[1]




#so now we have the pixel position of all of the thresholded
    ↪ points
# - it's time to implement the code
    ↪ .----------------------------------------
#import some functions



#this array are the y points we want the R1 values for
    ↪ ------------------------
y_range = np.arange((190),(400+total_list[counter1]), 1) #
    ↪ ------------------------------------------------------------------------
    ↪ initial array
#this is the array to keep the values in
R1_values = []
x_left =[]
x_right = []
R2_left = []
R2_right = []


#first we find the radius at each point (R1)
for i in y_range:
```

```
#print (i)
line = SG.LineString(list(zip(x_ords,y_ords)))
#print ('line', line)
yline = SG.LineString([(min(x_ords), i), (max(x_ords), i)])
#print ('yline', yline)
#print ('here' , line.intersection(yline))
#print (linemerge(line.intersection(yline)))


try:
    np.array(line.intersection(yline))
except TypeError:
    #print ('double value founf')
    coords1 = np.array(linemerge(line.intersection(yline)))
    x_rad1 = coords1[:,0]
    R_1 = abs(np.amin(x_rad1) - np.amax(x_rad1))
    x_left.append(np.amin(x_rad1))
    x_right.append(np.amax(x_rad1))
    #print (R_1)
    R1_values.append(R_1)
    #R1_values.append(0.00)
    #x_left.append(0.00)
    #x_right.append(0.00)
    continue
coords = np.array(line.intersection(yline))
#print(coords)
try:
    x_rad = coords[:, 0]
except IndexError:
    x_rad = [0, 0]
    continue
```

```
    #print (x_rad)
    R_1 = abs(x_rad[0] - x_rad[1])
    x_left.append(x_rad[0])
    x_right.append(x_rad[1])
    #print (R_1)
    R1_values.append(R_1)
    #findR1(x_ords, y_ords, i)
    #print (R1_values)

#print something to check we have finished
    ↪ ------------------------------------
print ('R1 found')



#take the left and right array and fit polynomial (2nd order )
    ↪ to it
#x_left and x_right are the two arrays to fit to

#need to make sure that the zeros are gone from the array -
    ↪ these were lines
#where there were no x values
#create two new arays that have no zeros in

x_right_noz = []
x_left_noz = []
y_range_noz_l = []
y_range_noz_r = []
R1_values_noz_l = []
R1_values_noz_r = []
#there is a lot of mess in the middle of the image that we need
    ↪ to clean up
```

```
#since the mess is all inside this makes cleaning easier
#getting an array for the polynomial to fit to for the left and
    ↪ right side-------------- you can change these to make the
    ↪ array fit better - but watch out because you don't want to
    ↪  cut out data
#left here
counter = 0
for i in x_left:
    if i < 600:
        x_left_noz.append(i)
        y_range_noz_l.append(y_range[counter])
        R1_values_noz_l.append(R1_values[counter])
        counter = counter+1
    else:
        counter = counter+1

#and for the right
counter = 0
for i in x_right:
    if i > 600:
        x_right_noz.append(i)
        y_range_noz_r.append(y_range[counter])
        R1_values_noz_r.append(R1_values[counter])
        counter = counter+1
    else:
        counter = counter+1


#lets divide the array into two parts here, fit the top and
    ↪ bottom seperately, less prone to errors
def split_list(a_list):
```

```
    half = len(a_list)//2
    return a_list[:half], a_list[half:]

y_range_noz_l_t, y_range_noz_l_b = split_list(y_range_noz_l)
y_range_noz_r_t, y_range_noz_r_b = split_list(y_range_noz_r)

x_left_noz_t, x_left_noz_b = split_list(x_left_noz)
x_right_noz_t, x_right_noz_b = split_list(x_right_noz)



#fit a polynomial here
    ↪ ----------------------------------------------------
#to make fitting easier the x and y have switched here so x = f(
    ↪ y)
#left bottom

polyfit_l_b = np.polyfit(y_range_noz_l_b, x_left_noz_b, 2) #here
    ↪  it is order 2
p_l_b = np.poly1d(polyfit_l_b)
#print (polyfit_l_b)
#print(np.poly1d(polyfit_l_b))


#right bottom
polyfit_r_b = np.polyfit(y_range_noz_r_b, x_right_noz_b, 2) #
    ↪ here it is order 2
p_r_b = np.poly1d(polyfit_r_b)
#print (polyfit_r_b)
#print(np.poly1d(polyfit_r_b))


#left top
polyfit_l_t = np.polyfit(y_range_noz_l_t, x_left_noz_t, 2) #here
```

```
    ↪ it is order 2
p_l_t = np.poly1d(polyfit_l_t)
#print (polyfit_l_t)
#print(np.poly1d(polyfit_l_t))

#right top
polyfit_r_t = np.polyfit(y_range_noz_r_t, x_right_noz_t, 2) #
    ↪ here it is order 2
p_r_t = np.poly1d(polyfit_r_t)
#print (polyfit_r_t)
#print(np.poly1d(polyfit_r_t))



#now we doubly differentiate the polynomial
    ↪ ----------------------------------
#bottom
p2_l_b = np.polyder(p_l_b, 2)
print ('left-b', np.poly1d(p2_l_b))
p22_l_b = np.poly1d(p2_l_b)

p2_r_b = np.polyder(p_r_b, 2)
print ('left-b', np.poly1d(p2_r_b))
p22_r_b = np.poly1d(p2_r_b)



#top
p2_l_t = np.polyder(p_l_t, 2)
#print (np.poly1d(p2_l_t))
p22_l_t = np.poly1d(p2_l_t)

p2_r_t = np.polyder(p_r_t, 2)
```

```
#print (np.poly1d(p2_r_t))
p22_r_t = np.poly1d(p2_r_t)

#recall we have p_r and p_l as our functions
#differentiate the funcitons (grad)
p1_l_t = np.polyder(p_l_t, 1)
#print (np.poly1d(p1_l_t))
p11_l_t = np.poly1d(p1_l_t)

p1_r_t = np.polyder(p_r_t, 1)
#print (np.poly1d(p1_r_t))
p11_r_t = np.poly1d(p1_r_t)

p1_l_b = np.polyder(p_l_b, 1)
#print (np.poly1d(p1_l_b))
p11_l_b = np.poly1d(p1_l_b)

p1_r_b = np.polyder(p_r_b, 1)
#print (np.poly1d(p1_r_b))
p11_r_b = np.poly1d(p1_r_b)

#now the polynomial is well fitted we can cal R1 and R2 for each
    ↪ point
y_fit = np.arange(150, (440+total_list[counter1]), 1) #
    ↪ ------------------------------------------------------------------------
    ↪ amend me to fit

y_fit_t, y_fit_b = split_list(y_fit)

x_fit_r_t = p_r_t(y_fit_t)
x_fit_l_t = p_l_t(y_fit_t)
```

```
x_fit_r_b = p_r_b(y_fit_b)
x_fit_l_b = p_l_b(y_fit_b)

R1_fit_t = abs(x_fit_r_t - x_fit_l_t)
R1_fit_b = abs(x_fit_r_b - x_fit_l_b)
#print ('R1 fit bottom', R1_fit_b)



#the bottom point is decided
bottom = 427+total_list[counter1]#
    ↪ ------------------------------------------------------------------------------
    ↪ bottom of bridge
top = 160#
    ↪ ------------------------------------------------------------------
    ↪ top of bridge
position_t = y_fit_t.tolist().index(top)
position_b = y_fit_b.tolist().index(bottom)

def func_line_l_t(xx):
    ang_l_t = x_l_t[position_t] * (xx - y_fit_t[position_t]) +
        ↪ x_fit_l_t[position_t]
    return ang_l_t

def func_line_r_t(xx):
    ang_r_t = x_r_t[position_t] * (xx - y_fit_t[position_t]) +
        ↪ x_fit_r_t[position_t]
    return ang_r_t

def func_line_l_b(xx):
    ang_l_b = x_l_b[position_b] * (xx - y_fit_b[position_b]) +
        ↪ x_fit_l_b[position_b]
```

```
    return ang_l_b

def func_line_r_b(xx):
    ang_r_b = x_r_b[position_b] * (xx - y_fit_b[position_b]) +
        ↪ x_fit_r_b[position_b]
    return ang_r_b

def x_line(x):
   x_line = x
   return x_line

#calc differential at point ie the gradient
x_l_t = p11_l_t(y_fit_t)
x_r_t = p11_r_t(y_fit_t)
x_l_b = p11_l_b(y_fit_b)
x_r_b = p11_r_b(y_fit_b)

print ('finished␣fitting')

fig9, ax = plt.subplots()
#fit the top sections left and right
ax.scatter(y_range_noz_l_t, x_left_noz_t, label = 'left␣side',
    ↪ color = 'red')
ax.plot(y_fit_t, p_l_t(y_fit_t), label = 'left␣fit', color = '
    ↪ red' )
ax.scatter(y_range_noz_r_t, x_right_noz_t, label = 'right␣side',
    ↪  color = 'red')
ax.plot(y_fit_t, p_r_t(y_fit_t), label = 'right␣fit', color = '
    ↪ red')
#fit the bottom section left and right
ax.scatter(y_range_noz_l_b, x_left_noz_b, label = 'left␣side',
```

```
    ↪ color = 'orange')
ax.plot(y_fit_b, p_l_b(y_fit_b), label = 'left fit', color = '
    ↪ orange' )
ax.scatter(y_range_noz_r_b, x_right_noz_b, label = 'right side',
    ↪  color = 'orange')
ax.plot(y_fit_b, p_r_b(y_fit_b), label = 'right fit', color = '
    ↪ orange')
ax.axvline(x=y_fit_t[position_t], color='g', linestyle='--')
ax.axvline(x=y_fit_b[position_b], color='r', linestyle='--')
#and compare to full data set...
ax.scatter(y_ords, x_ords, label = 'original')
#plot the tangent grads to cal angle
ax.plot(y_fit_t, func_line_r_t(y_fit_t), label = 'right angle',
    ↪ color = 'red', linestyle ='--' )
ax.plot(y_fit_t, func_line_l_t(y_fit_t), label = 'left angle',
    ↪ color = 'red', linestyle ='--' )
ax.plot(y_fit_b, func_line_r_b(y_fit_b), label = 'right angle',
    ↪ color = 'orange', linestyle ='--' )
ax.plot(y_fit_b, func_line_l_b(y_fit_b), label = 'left angle',
    ↪ color = 'orange', linestyle ='--' )
plt.savefig('figs\\frame%d.tif' % frame_no)
plt.legend()
plt.close(fig9)



print ('max left', min(min(x_left_noz_b), min(x_left_noz_t)))
print ('min right', max(max(x_right_noz_t), max(x_right_noz_b)))
largest_width = max(max(x_right_noz_t), max(x_right_noz_b))-min(
    ↪ min(x_left_noz_b), min(x_left_noz_t))
smallest_width = min(min(x_right_noz_t), min(x_right_noz_b))-max
    ↪ (max(x_left_noz_b), max(x_left_noz_t))
```

```
    #print (largest_width)


# #here we can calculate R2 using arcs - this is an extra check -
    ↪ not necessarily needed!
# if max(x_right_noz_t)> min(x_right_noz_b):
# place = x_right_noz_t.index(max(x_right_noz_t))
# cod = y_range_noz_l_t[place]
# initial = y_range_noz_l_t[0]
# width = (cod-initial)*2
# height = abs(max(x_right_noz_t)-x_right_noz_t[0])
# rad_here = (height/2)+((width**2)/(8*height))
# R2_arcs.append(rad_here)
# else:
# place = x_right_noz_b.index(max(x_right_noz_b))
# cod = y_range_noz_l_b[place]
# initial = y_range_noz_l_b[0]
# width = (cod-initial)*2
# height = abs(max(x_right_noz_b)-x_right_noz_b[0])
# rad_here = (height/2)+((width**2)/(8*height))
# R2_arcs.append(rad_here)
# #plt.show()


    fig10, ax = plt.subplots()
    im2 = original.rotate(0)
    im2.transpose(Image.FLIP_LEFT_RIGHT)
    plt.imshow(im2,cmap = 'gray')
    ax.plot(func_line_r_t(y_fit_t), y_fit_t, label = 'right␣angle',
        ↪ color = 'red', linestyle ='--' )
    ax.plot(func_line_l_t(y_fit_t), y_fit_t, label = 'left␣angle',
        ↪ color = 'red', linestyle ='--' )
    ax.plot(func_line_r_b(y_fit_b), y_fit_b, label = 'right␣angle',
```

```
    ↪ color = 'orange', linestyle ='--' )
ax.plot(func_line_l_b(y_fit_b), y_fit_b, label = 'left angle',
    ↪ color = 'orange', linestyle ='--' )
#plot the fit
#top
ax.plot(p_l_t(y_fit_t), y_fit_t, label = 'left fit', color = '
    ↪ red' )
ax.plot(p_r_t(y_fit_t), y_fit_t, label = 'right fit', color = '
    ↪ red' )
#bottom
ax.plot(p_l_b(y_fit_b), y_fit_b, label = 'left fit', color = '
    ↪ orange')
ax.plot(p_r_b(y_fit_b), y_fit_b, label = 'right fit', color = '
    ↪ orange')
#plot lines of bottom and top
ax.axhline(y=bottom, color='red', linestyle='--')
ax.axhline(y=top, color='green', linestyle='--')
plt.savefig('figs_1\\frame%d.tif' % frame_no)
#ax.scatter(x_ords, y_ords)
plt.close(fig10)
#plt.show()



#add in here we wwant to know thw position of the bottom and top
    ↪  meniscus when line crosses bottom and top
#bear in mind it might not always be accurate - especially as we
    ↪  are only fitting the top really

#now have top and bottom intersection code
#top left
y1 = y_fit_t
```

```
x1 = func_line_l_t(y_fit_t)
x2=func_line_l_t(y_fit_t)
y2=func_line_l_t(y_fit_t)*0+top
x_t_l,y_t_l=intersection(x1,y1,x2,y2)

intersect_left_xt.append(x_t_l[0])
intersect_left_yt.append(y_t_l[0])

#top right
y1 = y_fit_t
x1 = func_line_r_t(y_fit_t)
x2=func_line_r_t(y_fit_t)
y2=func_line_r_t(y_fit_t)*0+top
x_t_r,y_t_r=intersection(x1,y1,x2,y2)

intersect_right_xt.append(x_t_r[0])
intersect_right_yt.append(y_t_r[0])

#bottom left
y1 = y_fit_b
x1 = func_line_l_b(y_fit_b)
x2=func_line_l_b(y_fit_b)
y2=func_line_l_b(y_fit_b)*0+bottom
x_b_l,y_b_l=intersection(x1,y1,x2,y2)

intersect_left_xb.append(x_b_l[0])
intersect_left_yb.append(y_b_l[0])

#bottom right
y1 = y_fit_b
x1 = func_line_r_b(y_fit_b)
```

```
x2=func_line_r_b(y_fit_b)
y2=func_line_r_b(y_fit_b)*0+bottom
x_b_r,y_b_r=intersection(x1,y1,x2,y2)

intersect_right_xb.append(x_b_r[0])
intersect_right_yb.append(y_b_r[0])




#now make assumption that this line is good fit to angle
    ↪ ---------------------
left_angle_t = 90-(math.degrees(math.atan(x_l_t[position_t])))
right_angle_t = 90+(math.degrees(math.atan(x_r_t[position_t])))
left_angle_b = 90+(math.degrees(math.atan(x_l_b[position_b])))
right_angle_b = 90-(math.degrees(math.atan(x_r_b[position_b])))

left_angles_t.append(left_angle_t)
right_angles_t.append(right_angle_t)
left_angles_b.append(left_angle_b)
right_angles_b.append(right_angle_b)



if left_angle_t >90:
    aa = min(min(x_left_noz_b), min(x_left_noz_t))
    R2_t_l.append(1/(p22_l_t.c[0]/(1+(p11_l_t(x_fit_l_t[
        ↪ position_t]))**2)**(3/2)))
    R2_b_l.append(1/(p22_l_b.c[0]/(1+(p11_l_b(x_fit_l_b[
        ↪ position_b]))**2)**(3/2)))
    R2_t_r.append(1/(p22_r_t.c[0]/(1+(p11_l_t(x_fit_l_t[
        ↪ position_t]))**2)**(3/2)))
    R2_b_r.append(1/(p22_r_b.c[0]/(1+(p11_l_t(x_fit_l_t[
```

```
            ↪ position_b]))**2)**(3/2)))
        rad_largest.append(largest_width)
    else:
        bb = max(max(x_left_noz_b), max(x_left_noz_t))
        R2_t_l.append(1/(p22_l_t.c[0]/(1+(p11_l_t(x_fit_l_t[
            ↪ position_t]))**2)**(3/2)))
        R2_b_l.append(1/(p22_l_b.c[0]/(1+(p11_l_b(x_fit_l_b[
            ↪ position_b]))**2)**(3/2)))
        R2_t_r.append(1/(p22_r_t.c[0]/(1+(p11_l_t(x_fit_l_t[
            ↪ position_t]))**2)**(3/2)))
        R2_b_r.append(1/(p22_r_b.c[0]/(1+(p11_l_t(x_fit_l_t[
            ↪ position_b]))**2)**(3/2)))
        rad_largest.append(smallest_width)

    mini_t = min(R1_fit_t)
    mini_b = min(R1_fit_b)
    min_b.append(mini_b)
    min_t.append(mini_t)
    y_pos_t = y_fit_t[R1_fit_t.tolist().index(min(R1_fit_t))]
    y_pos_b = y_fit_b[R1_fit_b.tolist().index(min(R1_fit_b))]
    r1_pos_t.append(y_pos_t)
    r1_pos_b.append(y_pos_b)
    rad_top.append(abs(x_t_l[0]-x_t_r[0]))
    rad_bottom.append(abs(x_b_l[0]-x_b_r[0]))

    frame_no += 1
    counter1 = counter1+1

#angles are here
print (left_angles_t)
print (left_angles_b)
```

```
np.savetxt('left_angles_t.txt', left_angles_t,)
np.savetxt('left_angles_b.txt', left_angles_b,)
print (right_angles_t)
print (right_angles_b)
np.savetxt('right_angles_t.txt', right_angles_t)
np.savetxt('right_angles_b.txt', right_angles_b)


#all correct below - saved seperately for convenience
np.savetxt('intersect_left_xb.txt', intersect_left_xb)
np.savetxt('intersect_left_yb.txt', intersect_left_yb)
np.savetxt('intersect_left_xt.txt', intersect_left_xt)
np.savetxt('intersect_left_yt.txt', intersect_left_yt)
np.savetxt('intersect_right_xb.txt', intersect_right_xb)
np.savetxt('intersect_right_yb.txt', intersect_right_yb)
np.savetxt('intersect_right_xt.txt', intersect_right_xt)
np.savetxt('intersect_right_yt.txt', intersect_right_yt)


#R2 is the radius of curvature
np.savetxt('R2_t_l.txt', R2_t_l)
np.savetxt('R2_t_r.txt', R2_t_r)
np.savetxt('R2_b_l.txt', R2_b_l)
np.savetxt('R2_b_r.txt', R2_b_r)

#compare to the R2 value obtained above
#np.savetxt('R2-arcs.txt', R2_arcs)

#Radius of top and bottom and middle
np.savetxt('rad_top.txt', rad_top)#correct
np.savetxt('rad_bottom.txt', rad_bottom)#correct
```

```
np.savetxt('rad_largest.txt', rad_largest)
```

A.2.2 Extraction of Parameters (Complex Video)

'Extract_data_from_a_complex_video' works in the same way as the previous code, but instead of splitting the droplet edges into 4 quadrants, it splits it into 2. This gives a larger number of pixels to fit to the droplet edge and so improves the fitting. The parameters used are the same as the simple video analysis. To use this modified version, change the above function on line 309 to: def split_list(a_list): return a_list, a_list

A.2.3 Combine Extracted data with Stage and Force Data

'combine_extracted_data_with_others' brings together the data extracted from 'Extract_data_from_simple_video' and data from the force sensor (forces) and stages (positions). It interpolates between points meaning that all data can be plotted against each other. Each device has a time file alongside readings taken. It is these time files that are used to synchronize data between devices. Table V gives a list of variables found in the code.

```
"""
Created on Tue Sep 24 14:13:14 2019


@author: Sarah Goodband (lpps65)
"""
#import any functions needed here
import pylab
import matplotlib.pyplot as plt
from scipy.optimize import curve_fit
from scipy import asarray as ar,exp
import numpy as np
from scipy import special
```

Variable	Control Value
Fs_res1	Force sensor values
Fs_times1	Force sensor times
Stage_pos1	Stage positions (from the translation stages)
Stage_t1	Stage times
Cam_t1	Times from camera data
R2_bl/R2_tl/R2_br/R2_tr	The radius of curvature as measured in each of the 4 quadrants at the point of contact with the surface.
bottom_l_x/ bottom_l_y/ bottom_r_x/ bottom_r_y	Co-ordinates of the point of contact of the bridge with the bottom surface.
top_l_x/top_l_y/top _r_x/top_r_y	Co-ordinates of the point of contact of the bridge with the top surface
ang_lb/ang_lt/ang_rb/ ang_rt	CAs of the CLB with the surface

Table A.8: A table of variables found in the 'combine_extracted_data_with_others' script.

```
from scipy.special import erf
import matplotlib.pyplot as plt
from scipy.interpolate import interp1d



#force sensor data inputted here - import the Force and the times
    ↪ -----------------
#fs response here
fs_res1 = np.loadtxt("fs_response_1.txt")
```

```
#need to calibrate the fs data to convert from N to mN
fs_res1 = fs_res1*1000 #---------make mN

#fs times here, need to be converted in seconds instead of hours,
    ↪ mins, seconds from labview
fs_t1 = np.loadtxt("fs_times_2.txt")
fs_times1 = []

for i in fs_t1:
    length = len(str(i))
    if length==11:
        v1 = int(str(i)[:2])
        v2 = int(str(i)[2:4])
        v3 = int(str(i)[4:6])
        v4 = int(str(i)[7:11])
        total = v1*60*60+v2*60+v3+0.0001*v4
        #print (total)
        fs_times1.append(total)
    elif int(str(i)[:2]) > 24:
        v1 = int(str(i)[:1])
        v2 = int(str(i)[1:3])
        v3 = int(str(i)[3:5])
        v4 = int(str(i)[6:10])
        total = v1*60*60+v2*60+v3+0.0001*v4
        #print (total)
        fs_times1.append(total)
    else:
        v1 = int(str(i)[:2])
        v2 = int(str(i)[2:4])
        v3 = int(str(i)[4:6])
        v4 = int(str(i)[7:11])
```

```
        total = v1*60*60+v2*60+v3+0.0001*v4
        #print (total)
        fs_times1.append(total)



print ('stage times 1 finished')
#need stage_times to have a better format. So minus from it the
    ↪ smallest num - so we just get a difference
smallest_fs1 = np.min(fs_times1)
fs_diff1 = fs_times1-smallest_fs1



#plot fs data
    ↪ ------------------------------------------------------------------
    ↪
fig1, ax = plt.subplots()
plt.xlabel('Time, s')
plt.ylabel('force, mN')
#ax.set_xlim(xmin=0, xmax=200)
plt.scatter(fs_diff1, fs_res1, s=2, label='run1')
plt.legend()
fig1.tight_layout()
plt.show()



#begin importing the stage datas
    ↪ ----------------------------------------------
#positional data for stage here
stage_pos1 = np.loadtxt("stage_position_2.txt")
#stage_position = np.hsplit(stage_pos,1)
print('stage_position finished' )
```

```
#time data for stage here
stage_t1 = np.loadtxt("stage_times_2.txt")
#print (stage_t1)
stage_times1 = []

for i in stage_t1:
    length = len(str(i))
    if length==11:
        v1 = int(str(i)[:2])
        v2 = int(str(i)[2:4])
        v3 = int(str(i)[4:6])
        v4 = int(str(i)[7:11])
        total = v1*60*60+v2*60+v3+0.0001*v4
        #print (total)
        stage_times1.append(total)
    elif int(str(i)[:2]) > 24:
        v1 = int(str(i)[:1])
        v2 = int(str(i)[1:3])
        v3 = int(str(i)[3:5])
        v4 = int(str(i)[6:10])
        total = v1*60*60+v2*60+v3+0.0001*v4
        #print (total)
        stage_times1.append(total)
    else:
        v1 = int(str(i)[:2])
        v2 = int(str(i)[2:4])
        v3 = int(str(i)[4:6])
        v4 = int(str(i)[7:11])
        total = v1*60*60+v2*60+v3+0.0001*v4
        #print (total)
```

```
        stage_times1.append(total)

print ('stage␣times␣1')



#need stage_times to have a better format. So minus from it the
    ↪ smallest num - so we just get a difference
smallest_stage1 = np.min(stage_times1)
#print('smallest_stage1', smallest_stage1)
stage_diff1 = stage_times1-smallest_stage1
#print(stage_diff1)

#find the minimum of both arrays so one can easily plot them
    ↪ together
value1 = smallest_fs1-smallest_stage1
if value1 < 0:
    overall_smallest1 = smallest_fs1
else:
    overall_smallest1 = smallest_stage1
#print (overall_smallest1)

#now we can see the better arranged data for timesteps
fs_times1 = fs_times1 - overall_smallest1
stage_times1 = stage_times1 - overall_smallest1



#for plotting the overal datas
fig3, ax1 = plt.subplots()
ax1.scatter(fs_diff1, fs_res1, s=2, label='run1', color = 'blue')
ax1.tick_params('y', colors='black')
plt.xlabel('Time,␣s')
```

```
plt.ylabel('force, mN', color='black')
plt.legend()

ax2 = ax1.twinx()
ax2.plot(stage_times1, stage_pos1, color='lightblue', linestyle='
    ↪ dashed', label ='run1')
ax2.tick_params('y', colors='grey')
plt.ylabel('stage position, mm', color='grey')
plt.legend()
fig3.tight_layout()
plt.show()

#camera data from the previous script imported here
    ↪ ------------------------------------------------

#camera times here
cam_t1 = np.loadtxt("camera_times_2.txt")
cam_times1 = []

for i in cam_t1:
    length = len(str(i))
    if length==11:
        v1 = int(str(i)[:2])
        v2 = int(str(i)[2:4])
        v3 = int(str(i)[4:6])
        v4 = int(str(i)[7:11])
        total = v1*60*60+v2*60+v3+0.0001*v4
        #print (total)
        cam_times1.append(total)
    elif int(str(i)[:2]) > 24:
        v1 = int(str(i)[:1])
```

```
        v2 = int(str(i)[1:3])
        v3 = int(str(i)[3:5])
        v4 = int(str(i)[6:10])
        total = v1*60*60+v2*60+v3+0.0001*v4
        #print (total)
        cam_times1.append(total)
    else:
        v1 = int(str(i)[:2])
        v2 = int(str(i)[2:4])
        v3 = int(str(i)[4:6])
        v4 = int(str(i)[7:11])
        total = v1*60*60+v2*60+v3+0.0001*v4
        #print (total)
        cam_times1.append(total)



print ('cam_times1', cam_times1)
#now we add in the camera code - so use diff above for ease
cam_times1 = cam_times1 - overall_smallest1
cam_times1 = cam_times1[::30]
cam_times1 = cam_times1[4:265]

#cam_times1 = cam_times1[111:]
    ↪ #-----------------------------------------you need to
    ↪ change this to match the frames you chose
cam_times_frame_no = np.arange(0, 7923, 30)
cam_times_frame_no = cam_times_frame_no[4:265]
print (cam_times_frame_no)
#cam_times_frame_no = cam_times_frame_no[111:]
print (cam_times_frame_no)
cam_times_frame_no = cam_times_frame_no.tolist() #
```

```
    ↪ ----------------------change this to above too!
print (cam_times_frame_no)
print (len(cam_times_frame_no))
print (len(cam_times1))

#import other files we need
    ↪ ------------------------------------------------------------------------------
    ↪
R2_bl = np.loadtxt("R2_b_l.txt")
R2_tl = np.loadtxt("R2_t_l.txt")
R2_br = np.loadtxt("R2_b_r.txt")
R2_tr = np.loadtxt("R2_t_r.txt")

#import more files such as position etc to cal the rad and suchneck
    ↪ rad etc
#positions of the different contact lines
bottom_l_x = np.loadtxt('intersect_left_xb.txt')
bottom_l_y = np.loadtxt('intersect_left_yb.txt')

bottom_r_x = np.loadtxt('intersect_right_xb.txt')
bottom_r_y = np.loadtxt('intersect_right_yb.txt')

top_l_x = np.loadtxt('intersect_left_xt.txt')
top_l_y = np.loadtxt('intersect_left_yt.txt')

top_r_x = np.loadtxt('intersect_right_xt.txt')
top_r_y = np.loadtxt('intersect_right_yt.txt')

dia_b = abs(bottom_l_x-bottom_r_x)
dia_t = abs(top_l_x-top_r_x)
```

```
#angles of the top and bottom
ang_lb = np.loadtxt('left_angles_b.txt')
ang_lt = np.loadtxt('left_angles_t.txt')
ang_rb = np.loadtxt('right_angles_b.txt')
ang_rt = np.loadtxt('right_angles_t.txt')



#now we want to interpolate the datas
    ↪ ----------------------------------------


f_stage = interp1d(stage_times1, stage_pos1)
f_force = interp1d(fs_diff1, fs_res1)

stage_av = f_stage(cam_times1[2:190])
force_av = f_force(cam_times1[2:190])

#time and position
    ↪ ------------------------------------------------------------
fig4 = plt.subplots()
plt.scatter(stage_av, force_av, color = 'orange')
plt.plot(stage_av, force_av, color = 'orange')
plt.xlabel('Time, s')
plt.ylabel('position, mm')
plt.show()

#time and position
    ↪ ------------------------------------------------------------
fig4 = plt.subplots()
plt.plot(cam_times1[2:190], stage_av, color = 'orange')
plt.xlabel('Time, s')
plt.ylabel('position, mm')
```

```
plt.show()



#here let's save the data so it's more readable/easy to use
np.savetxt('F:\\camera_data_using\\20.12.04_data\\for␣poster\\
    ↪ d1_10ul_20CST_THIN_step0.05_acc2_rep3_0.003mms_9␣-␣Copy\\
    ↪ model_data_2\\position_run_2ul_LIS_0.1mms_1.txt', stage_av)
np.savetxt('F:\\camera_data_using\\20.12.04_data\\for␣poster\\
    ↪ d1_10ul_20CST_THIN_step0.05_acc2_rep3_0.003mms_9␣-␣Copy\\
    ↪ model_data_2\\force_run_2ul_LIS_0.1mms_1.txt', force_av)

np.savetxt('F:\\camera_data_using\\20.12.04_data\\for␣poster\\
    ↪ d1_10ul_20CST_THIN_step0.05_acc2_rep3_0.003mms_9␣-␣Copy\\
    ↪ model_data_2\\diameter_bottom_2ul_LIS_0.1mms_1.txt', dia_b
    ↪ [2:190])
np.savetxt('F:\\camera_data_using\\20.12.04_data\\for␣poster\\
    ↪ d1_10ul_20CST_THIN_step0.05_acc2_rep3_0.003mms_9␣-␣Copy\\
    ↪ model_data_2\\diameter_top_2ul_LIS_0.1mms_1.txt', dia_t
    ↪ [2:190])

np.savetxt('F:\\camera_data_using\\20.12.04_data\\for␣poster\\
    ↪ d1_10ul_20CST_THIN_step0.05_acc2_rep3_0.003mms_9␣-␣Copy\\
    ↪ model_data_2\\R2_bl_2ul_LIS_0.1mms_1.txt', R2_bl[2:190] )
np.savetxt('F:\\camera_data_using\\20.12.04_data\\for␣poster\\
    ↪ d1_10ul_20CST_THIN_step0.05_acc2_rep3_0.003mms_9␣-␣Copy\\
    ↪ model_data_2\\R2_tl_2ul_LIS_0.1mms_1.txt', R2_tl[2:190] )
np.savetxt('F:\\camera_data_using\\20.12.04_data\\for␣poster\\
    ↪ d1_10ul_20CST_THIN_step0.05_acc2_rep3_0.003mms_9␣-␣Copy\\
    ↪ model_data_2\\R2_br_2ul_LIS_0.1mms_1.txt', R2_br[2:190] )
np.savetxt('F:\\camera_data_using\\20.12.04_data\\for␣poster\\
```

```
    ↪ d1_10ul_20CST_THIN_step0.05_acc2_rep3_0.003mms_9␣-␣Copy\\
    ↪ model_data_2\\R2_tr_2ul_LIS_0.1mms_1.txt', R2_tr[2:190] )

np.savetxt('F:\\camera_data_using\\20.12.04_data\\for␣poster\\
    ↪ d1_10ul_20CST_THIN_step0.05_acc2_rep3_0.003mms_9␣-␣Copy\\
    ↪ model_data_2\\la_bottom_2ul_LIS_0.1mms_1.txt', ang_lb[2:190])
np.savetxt('F:\\camera_data_using\\20.12.04_data\\for␣poster\\
    ↪ d1_10ul_20CST_THIN_step0.05_acc2_rep3_0.003mms_9␣-␣Copy\\
    ↪ model_data_2\\la_top_2ul_LIS_0.1mms_1.txt', ang_lt[2:190])
np.savetxt('F:\\camera_data_using\\20.12.04_data\\for␣poster\\
    ↪ d1_10ul_20CST_THIN_step0.05_acc2_rep3_0.003mms_9␣-␣Copy\\
    ↪ model_data_2\\ra_bottom_2ul_LIS_0.1mms_1.txt', ang_rb[2:190])
np.savetxt('F:\\camera_data_using\\20.12.04_data\\for␣poster\\
    ↪ d1_10ul_20CST_THIN_step0.05_acc2_rep3_0.003mms_9␣-␣Copy\\
    ↪ model_data_2\\ra_top_2ul_LIS_0.1mms_1.txt', ang_rt[2:190])

np.savetxt('F:\\camera_data_using\\20.12.04_data\\for␣poster\\
    ↪ d1_10ul_20CST_THIN_step0.05_acc2_rep3_0.003mms_9␣-␣Copy\\
    ↪ model_data_2\\framw_no_2ul_LIS_0.1mms_1.txt',
    ↪ cam_times_frame_no[2:190])
#here the know initial separation is 1mm. So whatever the stage
    ↪ started at can be removed and 1mm is the starting value.
np.savetxt('F:\\camera_data_using\\20.12.04_data\\for␣poster\\
    ↪ d1_10ul_20CST_THIN_step0.05_acc2_rep3_0.003mms_9␣-␣Copy\\
    ↪ model_data_2\\sep_cm_2ul_LIS_0.1mms_1.txt', stage_av-stage_av
    ↪ [0]+1)
```

A.2.4 Visualise all Data

'Visualise all data' was designed to visualise the data extracted against a model (here eq.2). It also scales the data from pixels to mm and allows the user to select

individual stretches and compression for separate analysis. It takes the variables shown in Table VI:

Variable	Control Value
top_rad	The top contact radius of the CLB.
top_ang	The angle at the point of contact with the top surface.
R1	Here also the top contact radius – this file is different if you measure the variables at a different point.
R2	The radius of curvature at the top of the bridge.
Sep_mm	The separation of the plates in mm.
force	The force measured by the load cell.
sg_tens/sw_tens	the surface tension of an 80% glycerol-water mix or pure water (can be changed).
drop_dens_g/drop_dens_w	The density of an 80% glycerol-water mix or pure water (can be changed)
R2_f1, sep_m_f1, R1_f1, R_mid_f1, top_ang-f1, force_f1	If splitting the arrays into separate stretching or compressing motions, these are the arrays used to split the main array.

Table A.10: A table of variables found in the 'extract data from a simple video' script.

```
"""
Created on Mon Jul 13 16:09:34 2020
```

```
@author: Sarah Goodband (lpps65)

This is the force on the top plate.
"""
import numpy as np
import math
import matplotlib.pyplot as plt

def movingaverage(interval, window_size):
    window= np.ones(int(window_size))/float(window_size)
    return np.convolve(interval, window, 'same')

top_rad = np.loadtxt("diameter_top_2ul_LIS_0.1mms_1.txt")
top_ang = np.loadtxt("la_top_2ul_LIS_0.1mms_1.txt")
R1 = np.loadtxt("diameter_top_2ul_LIS_0.1mms_1.txt")
R2 = np.loadtxt("R2_tl_2ul_LIS_0.1mms_1.txt")
R_mid = np.loadtxt("rad_largest.txt")
sep_mm = np.loadtxt("sep_cm_2ul_LIS_0.1mms_1.txt")
force = np.loadtxt("force_run_2ul_LIS_0.1mms_1.txt") # in mN

con = 3.27E-3 #- this is calculated from the image/given by camera
    ↪ sometimes
#convert all the above values to m
top_rad = (top_rad/2)*con*1E-3
R1 = (R1/2)*con*1E-3
R2 = R2*con*1E-3
sep_m = sep_mm*1E-3
R_mid = (R_mid/2)*con*1E-3
#some set variables
sg_tens = 6.74E-2 # glycerol
```

```
sw_tens = 7.2E-2 # water
drop_v = 1E-8
drop_dens_g = 1204 #glycerol
drop_dens_w = 997



#---------------
#split into regions
#forward
R2_f1 = R2[0:33]
sep_m_f1 = sep_m[0:33]
R1_f1 = R1[0:33]
R_mid_f1 = R_mid[0:33]
top_ang_f1 = top_ang[0:33]
force_f1 = force[0:33]

#backward
R2_b1 = R2[32:64]
sep_m_b1 = sep_m[32:64]
R1_b1 = R1[32:64]
R_mid_b1 = R_mid[32:64]
top_ang_b1 = top_ang[32:64]
force_b1 = force[32:64]
#calculated force
    ↪ ------------------------------------------------------------------
    ↪
fig5 = plt.subplots()
plt.plot(sep_m_f1, force_f1, color = 'lightblue', label = 'forward')
plt.scatter(sep_m_f1, force_f1, color = 'lightblue')


plt.plot(sep_m_b1, force_b1, color = 'blue', label = 'backward')
```

```
plt.scatter(sep_m_b1, force_b1, color = 'blue')
plt.xlabel('Plate separation, s')
plt.ylabel('Force, mN')
plt.legend()
plt.show()

#we put fits as section specific-----------------------
polyfit_R1_f1 = np.polyfit(sep_m_f1, R1_f1, 2) #here it is order 2
p_R1_f1 = np.poly1d(polyfit_R1_f1)

polyfit_R_mid_f1 = np.polyfit(sep_m_f1, R_mid_f1, 2) #here it is
    ↪ order 2
p_R_mid_f1 = np.poly1d(polyfit_R_mid_f1)

polyfit_R2_f1 = np.polyfit(sep_m_f1, R2_f1, 2) #here it is order 2
p_R2_f1 = np.poly1d(polyfit_R2_f1)

polyfit_top_ang_f1 = np.polyfit(sep_m_f1, top_ang_f1, 2) #here it is
    ↪  order 2
p_top_ang_f1 = np.poly1d(polyfit_top_ang_f1)

#we put fits as section specific-----------------------
polyfit_R1_b1 = np.polyfit(sep_m_b1, R1_b1, 2) #here it is order 2
p_R1_b1 = np.poly1d(polyfit_R1_b1)

polyfit_R_mid_b1 = np.polyfit(sep_m_b1, R_mid_b1, 2) #here it is
    ↪ order 2
p_R_mid_b1 = np.poly1d(polyfit_R_mid_b1)

polyfit_R2_b1 = np.polyfit(sep_m_b1, R2_b1, 2) #here it is order 2
p_R2_b1 = np.poly1d(polyfit_R2_b1)
```

```
polyfit_top_ang_b1 = np.polyfit(sep_m_b1, top_ang_b1, 2) #here it is
    ↪  order 2
p_top_ang_b1 = np.poly1d(polyfit_top_ang_b1)

#calculated force
    ↪ ------------------------------------------------------------------
    ↪
fig5 = plt.subplots()

plt.rcParams['font.size'] = '20'

plt.plot(sep_m_f1*1E3, p_R1_f1(sep_m_f1)*1E3, color = 'lightblue',
    ↪ label = 'forward')
plt.scatter(sep_m_f1*1E3, R1_f1*1E3, color = 'lightblue')
plt.plot(sep_m_b1*1E3, p_R1_b1(sep_m_b1)*1E3, color = 'blue', label
    ↪ = 'backward')
plt.scatter(sep_m_b1*1E3, R1_b1*1E3, color = 'blue')
plt.xlabel('Plate␣separation,␣mm')
plt.ylabel('Base␣Radius,␣mm')
plt.legend()
plt.show()

#calculated force
    ↪ ------------------------------------------------------------------
    ↪
fig5 = plt.subplots()
plt.plot(sep_m_f1, p_R2_f1(sep_m_f1), color = 'lightblue', label = '
    ↪ forward')
plt.scatter(sep_m_f1, R2_f1, color = 'lightblue')
plt.plot(sep_m_b1, p_R2_b1(sep_m_b1), color = 'blue', label = '
```

```
    ↪ backward')
plt.scatter(sep_m_b1, R2_b1, color = 'blue')
plt.xlabel('Plate␣separation,␣s')
plt.ylabel('R2')
plt.legend()
plt.show()

#calculated force
    ↪ ------------------------------------------------------------------
    ↪
fig5 = plt.subplots()

plt.rcParams['font.size'] = '20'

plt.scatter(sep_m_f1*1E3, R1_f1*1E3, color = 'orange', label = 'R1')
plt.scatter(sep_m_b1*1E3, R1_b1*1E3, color = 'orange')

plt.scatter(sep_m_f1*1E3, R2_f1*1E3, color = 'red', label = 'R2')
plt.scatter(sep_m_b1*1E3, R2_b1*1E3, color = 'red')

plt.scatter(sep_m_f1*1E3, R_mid_f1*1E3, color = 'yellow', label = '
    ↪ Rm')
plt.scatter(sep_m_b1*1E3, R_mid_b1*1E3, color = 'yellow')

plt.xlabel('Plate␣separation,␣mm')
plt.ylabel('Radius,␣mm')
plt.legend()
plt.show()



#calculated force
```

```
    ↪ ------------------------------------------------------------------
    ↪
fig5 = plt.subplots()
plt.plot(sep_m_f1, p_top_ang_f1(sep_m_f1), color = 'lightblue',
    ↪ label = 'forward')
plt.scatter(sep_m_f1, top_ang_f1, color = 'lightblue')
plt.plot(sep_m_b1, p_top_ang_b1(sep_m_b1), color = 'blue', label = '
    ↪ backward')
plt.scatter(sep_m_b1, top_ang_b1, color = 'blue')
plt.xlabel('Plate␣separation,␣s')
plt.ylabel('Angle,␣degrees')
plt.legend()
plt.show()

#calculated force
    ↪ ------------------------------------------------------------------
    ↪
ax, fig = plt.subplots()



plt.plot(sep_m_f1*1E3, top_ang_f1, color = 'lightblue', label = '
    ↪ forward')
plt.scatter(sep_m_f1*1E3, top_ang_f1, color = 'lightblue')
plt.plot(sep_m_b1*1E3, top_ang_b1, color = 'blue', label = 'backward
    ↪ ')
plt.scatter(sep_m_b1*1E3, top_ang_b1, color = 'blue')
plt.xlabel('Plate␣separation,␣mm')
plt.ylabel('Angle,␣degrees')
plt.legend()
plt.show()
```

```
#clean the forward(not always needed)
    ↪ ------------------------------------------------------------------------------
    ↪
R2_f1_clean = []
sep_m_f1_clean = []
R1_f1_clean = []
R_mid_f1_clean = []
top_ang_f1_clean = []
force_f1_clean = []
count = 0
for i in R2_f1:
    if 0.05>i>-0.05:
        R2_f1_clean.append(i)
        sep_m_f1_clean.append(sep_m_f1[count])
        R_mid_f1_clean.append(R_mid_f1[count])
        R1_f1_clean.append(R1_f1[count])
        top_ang_f1_clean.append(top_ang_f1[count])
        force_f1_clean.append(force_f1[count])

        count = count+1
    else:
        count = count+1

R1_av_f1 = movingaverage(R1_f1_clean, 5)
R_mid_av_f1 = movingaverage(R_mid_f1_clean, 5)
R2_av_f1 = movingaverage(R2_f1_clean, 5)

#we put fits as section specific-----------------------
polyfit_R1_f1_clean = np.polyfit(sep_m_f1_clean, R1_f1_clean, 2) #
    ↪ here it is order 2
p_R1_f1_clean = np.poly1d(polyfit_R1_f1_clean)
```

```
polyfit_R_mid_f1_clean = np.polyfit(sep_m_f1_clean, R_mid_f1_clean,
    ↪ 2) #here it is order 2
p_R_mid_f1_clean = np.poly1d(polyfit_R_mid_f1_clean)

polyfit_R2_f1_clean = np.polyfit(sep_m_f1_clean, R2_f1_clean, 2) #
    ↪ here it is order 2
p_R2_f1_clean = np.poly1d(polyfit_R2_f1_clean)

polyfit_top_ang_f1_clean = np.polyfit(sep_m_f1_clean,
    ↪ top_ang_f1_clean, 2) #here it is order 2
p_top_ang_f1_clean = np.poly1d(polyfit_top_ang_f1_clean)

#again for the backward
    ↪ ------------------------------------------------------------------------
    ↪
R2_b1_clean = []
sep_m_b1_clean = []
R1_b1_clean = []
R_mid_b1_clean = []
top_ang_b1_clean = []
force_b1_clean = []
count = 0
for i in R2_b1:
    if 0.05>i>-0.05:
        R2_b1_clean.append(i)
        sep_m_b1_clean.append(sep_m_b1[count])
        R_mid_b1_clean.append(R_mid_b1[count])
        R1_b1_clean.append(R1_b1[count])
        top_ang_b1_clean.append(top_ang_b1[count])
        force_b1_clean.append(force_b1[count])
```

```
        count = count+1
    else:
        count = count+1

R1_av_b1 = movingaverage(R1_b1_clean, 5)
R_mid_av_b1 = movingaverage(R_mid_b1_clean, 5)
R2_av_b1 = movingaverage(R2_b1_clean, 5)

#we put fits as section specific-----------------------
polyfit_R1_b1_clean = np.polyfit(sep_m_b1_clean, R1_b1_clean, 2) #
    ↪ here it is order 2
p_R1_b1_clean = np.poly1d(polyfit_R1_b1_clean)

polyfit_R_mid_b1_clean = np.polyfit(sep_m_b1_clean, R_mid_b1_clean,
    ↪ 2) #here it is order 2
p_R_mid_b1_clean = np.poly1d(polyfit_R_mid_b1_clean)

polyfit_R2_b1_clean = np.polyfit(sep_m_b1_clean, R2_b1_clean, 2) #
    ↪ here it is order 2
p_R2_b1_clean = np.poly1d(polyfit_R2_b1_clean)

polyfit_top_ang_b1_clean = np.polyfit(sep_m_b1_clean,
    ↪ top_ang_b1_clean, 2) #here it is order 2
p_top_ang_b1_clean = np.poly1d(polyfit_top_ang_b1_clean)



#save the angle data
np.savetxt('angle_data\\top_ang_f1_clean.txt', top_ang_f1_clean)
np.savetxt('angle_data\\sep_m_f1_clean1.txt', sep_m_f1_clean)
```

```
np.savetxt('angle_data\\top_ang_b1_clean.txt', top_ang_b1_clean)
np.savetxt('angle_data\\sep_m_b1_clean1.txt', sep_m_b1_clean)
np.savetxt('angle_data\\force_f1_clean1.txt', force_f1_clean)
np.savetxt('angle_data\\force_b1_clean1.txt', force_b1_clean)

#calculated force
    ↪ ----------------------------------------------------------------------
    ↪
fig5 = plt.subplots()
plt.plot(sep_m_f1, p_R2_f1_clean(sep_m_f1), color = 'lightblue',
    ↪ label = 'forward')
plt.scatter(sep_m_f1, R2_f1, color = 'lightblue')
plt.plot(sep_m_b1, p_R2_b1_clean(sep_m_b1), color = 'blue', label =
    ↪ 'backward')
plt.scatter(sep_m_b1, R2_b1, color = 'blue')
plt.xlabel('Plate␣separation,␣s')
plt.ylabel('R2')
plt.legend()
plt.show()

itter = np.arange(0, (len(top_ang_f1_clean)), 1)
itter2 = np.arange(0, (len(top_ang_b1_clean)), 1)
#the different calculations use different levels of smoothing/
    ↪ averaging on the data before plotting.
#cal = nothing done to points
#cal1 = using cleaned arrays that are averaged
#cal2 =moving average

#create an array for our calucalted force values
force_cal_f1 = []
sep_cal_f1 = []
```

```
force_cal1_f1 = []
force_cal2_f1 = []



force_cal_b1 = []
sep_cal_b1 = []
force_cal1_b1 = []
force_cal2_b1 = []




for i in itter:

    calc_force_f1 =((-2*np.pi*sg_tens*R1_f1_clean[i]*np.sin(np.pi*
        ↪ top_ang_f1_clean[i]/180))+(np.pi*(R1_f1_clean[i]**2)*((1/
        ↪ R1_f1_clean[i])+(1/R2_f1_clean[i]))*sg_tens))*1000
    calc_force_clean1_f1 =((-2*np.pi*sg_tens*R1_av_f1[i]*np.sin(np.
        ↪ pi*top_ang_f1_clean[i]/180))+(np.pi*(R1_av_f1[i]**2)*((1/
        ↪ R1_av_f1[i])+(1/R2_av_f1[i]))*sg_tens))*1000
    calc_force_clean_f1 =((-2*np.pi*sg_tens*p_R1_f1_clean(
        ↪ sep_m_f1_clean[i])*np.sin(np.pi*p_top_ang_f1_clean(
        ↪ sep_m_f1_clean[i])/180))+(np.pi*(p_R1_f1_clean(
        ↪ sep_m_f1_clean[i])**2)*((1/p_R1_f1_clean(sep_m_f1_clean[i
        ↪ ]))+(1/p_R2_f1_clean(sep_m_f1_clean[i])))*sg_tens))*1000 #
        ↪ calc_force_clean =((-2*np.pi*sg_tens*R1_av[i]*np.sin(np.pi
        ↪ *top_ang[i]/180))+(np.pi*(R1_av[i]**2)*((1/R1_av[i])+(1/
        ↪ R2_av[i]))*sg_tens)+(np.pi*(R_mid_av[i]**2)*drop_dens_g
        ↪ *9.8*(sep_m[i])))*1000
    calc_force_f1_ng =((-2*np.pi*sg_tens*R1_f1_clean[i]*np.sin(np.pi
        ↪ *top_ang_f1_clean[i]/180))+(np.pi*(R1_f1_clean[i]**2)*((1/
        ↪ R1_f1_clean[i])+(1/R2_f1_clean[i]))*sg_tens))*1000
```

```
    force_cal_f1.append(calc_force_f1)
    force_cal1_f1.append(calc_force_clean_f1)
    force_cal2_f1.append(calc_force_clean1_f1)
    sep_cal_f1.append(sep_m_f1_clean[i]*1E3)



np.savetxt('backforward\\cal_force_f1.txt', force_cal_f1)
np.savetxt('backforward\\R1_igor_f1.txt', R1_f1)
np.savetxt('backforward\\cal_force_clean_f1.txt', force_cal1_f1)
np.savetxt('backforward\\cal_force_clean1_f1.txt', force_cal2_f1)
np.savetxt('backforward\\sepmm_igor_f1.txt', sep_cal_f1)



for i in itter2:

    calc_force_b1 =((-2*np.pi*sg_tens*R1_b1_clean[i]*np.sin(np.pi*
        ↪ top_ang_b1_clean[i]/180))+(np.pi*(R1_b1_clean[i]**2)*((1/
        ↪ R1_b1_clean[i])+(1/R2_b1_clean[i]))*sg_tens))*1000
    calc_force_clean1_b1 =((-2*np.pi*sg_tens*R1_av_b1[i]*np.sin(np.
        ↪ pi*top_ang_b1_clean[i]/180))+(np.pi*(R1_av_b1[i]**2)*((1/
        ↪ R1_av_b1[i])+(1/R2_av_b1[i]))*sg_tens))*1000
    calc_force_clean_b1 =((-2*np.pi*sg_tens*p_R1_b1_clean(
        ↪ sep_m_b1_clean[i])*np.sin(np.pi*p_top_ang_b1_clean(
        ↪ sep_m_b1_clean[i])/180))+(np.pi*(p_R1_b1_clean(
        ↪ sep_m_b1_clean[i])**2)*((1/p_R1_b1_clean(sep_m_b1_clean[i
        ↪ ]))+(1/p_R2_b1_clean(sep_m_b1_clean[i])))*sg_tens))*1000 #
        ↪ calc_force_clean =((-2*np.pi*sg_tens*R1_av[i]*np.sin(np.pi
        ↪ *top_ang[i]/180))+(np.pi*(R1_av[i]**2)*((1/R1_av[i])+(1/
        ↪ R2_av[i]))*sg_tens)+(np.pi*(R_mid_av[i]**2)*drop_dens_g
        ↪ *9.8*(sep_m[i])))*1000
```

```
    calc_force_b1_ng =((-2*np.pi*sg_tens*R1_b1_clean[i]*np.sin(np.pi
        ↪ *top_ang_b1_clean[i]/180))+(np.pi*(R1_b1_clean[i]**2)*((1/
        ↪ R1_b1_clean[i])+(1/R2_b1_clean[i]))*sg_tens))*1000
    #print (calc_force)
    force_cal_b1.append(calc_force_b1)
    force_cal1_b1.append(calc_force_clean_b1)
    force_cal2_b1.append(calc_force_clean1_b1)
    sep_cal_b1.append(sep_m_b1_clean[i]*1E3)



np.savetxt('backforward\\cal_force_b1.txt', force_cal_b1)
np.savetxt('backforward\\R1_igor_b1.txt', R1_b1)
np.savetxt('backforward\\cal_force_clean_b1.txt', force_cal1_b1)
np.savetxt('backforward\\cal_force_clean1_b1.txt', force_cal2_b1)
np.savetxt('backforward\\sepmm_igor_b1.txt', sep_cal_b1)



#calculated force
    ↪ ----------------------------------------------------------------
    ↪
fig5 = plt.subplots()
plt.plot(sep_cal_f1, force_f1_clean, label = 'forward', color = '
    ↪ lightblue')
plt.scatter(sep_cal_f1, force_f1_clean, color = 'lightblue' )

plt.plot(sep_cal_b1, force_b1_clean, label = 'backward', color = '
    ↪ blue')
plt.scatter(sep_cal_b1, force_b1_clean, color = 'blue' )
plt.xlabel('Plate␣separation,␣s')
plt.ylabel('Force␣calculated,␣mN')
```

```
plt.legend()
plt.show()

#calculated force
    ↪ ----------------------------------------------------------------
    ↪
fig5 = plt.subplots()
plt.plot(sep_cal_f1, force_cal_f1-force_cal_f1[31], color = '
    ↪ lightgreen', label = 'no␣correction')
plt.scatter(sep_cal_f1, force_cal_f1-force_cal_f1[31], color = '
    ↪ lightgreen')
plt.plot(sep_cal_b1, force_cal_b1-force_cal_b1[0], color = 'green')
plt.scatter(sep_cal_b1, force_cal_b1-force_cal_b1[0], color = 'green
    ↪ ')

plt.plot(sep_cal_f1, force_cal1_f1-force_cal2_f1[31], label = '
    ↪ corrected␣force1', color = 'salmon')
plt.plot(sep_cal_b1, force_cal1_b1-force_cal2_b1[5], color = 'red')

plt.plot(sep_cal_f1, force_f1_clean-force_f1_clean[31], label = '
    ↪ forward', color = 'lightblue')
plt.scatter(sep_cal_f1, force_f1_clean-force_f1_clean[31], color = '
    ↪ lightblue' )
plt.plot(sep_cal_b1, force_b1_clean-force_b1_clean[0], label = '
    ↪ backward', color = 'blue')
plt.scatter(sep_cal_b1, force_b1_clean-force_b1_clean[0], color = '
    ↪ blue' )

plt.xlabel('Plate␣separation,␣s')
plt.ylabel('Force␣calculated,␣mN')
plt.legend()
```

```
plt.show()


#calculated force
    ↪ ----------------------------------------------------------------------
    ↪
fig5 = plt.subplots()
plt.plot(sep_cal_f1, force_cal1_f1-force_cal2_f1[31], label = '
    ↪ corrected␣force1', color = 'orange')
plt.plot(sep_cal_b1, force_cal1_b1-force_cal2_b1[5], color = '
    ↪ darkorange')


plt.plot(sep_cal_f1, force_f1_clean-force_f1_clean[31], label = '
    ↪ forward', color = 'lightblue')
plt.scatter(sep_cal_f1, force_f1_clean-force_f1_clean[31], color = '
    ↪ lightblue' )
plt.plot(sep_cal_b1, force_b1_clean-force_b1_clean[0], label = '
    ↪ backward', color = 'blue')
plt.scatter(sep_cal_b1, force_b1_clean-force_b1_clean[0], color = '
    ↪ blue' )
plt.xlabel('Plate␣separation,␣s')
plt.ylabel('Force␣calculated,␣mN')
plt.legend()
plt.show()


#calculated force
    ↪ ----------------------------------------------------------------------
    ↪
fig5 = plt.subplots()
plt.plot(sep_cal_f1, force_f1_clean-force_f1_clean[31], label = '
    ↪ forward', color = 'lightblue')
plt.scatter(sep_cal_f1, force_f1_clean-force_f1_clean[31], color = '
```

```
    ↪ lightblue' )
plt.plot(sep_cal_f1, force_cal_f1-force_cal_f1[31], color = '
    ↪ lightgreen', label = 'forward␣model')
plt.scatter(sep_cal_f1, force_cal_f1-force_cal_f1[31], color = '
    ↪ lightgreen')


plt.plot(sep_cal_b1, force_b1_clean-force_b1_clean[0], label = '
    ↪ backward', color = 'blue')
plt.scatter(sep_cal_b1, force_b1_clean-force_b1_clean[0], color = '
    ↪ blue' )
plt.plot(sep_cal_b1, force_cal_b1-force_cal_b1[0], color = 'green',
    ↪ label = 'backward␣model')
plt.scatter(sep_cal_b1, force_cal_b1-force_cal_b1[0], color = 'green
    ↪ ')


plt.xlabel('Plate␣separation,␣s')
plt.ylabel('Force␣calculated,␣mN')
#plt.legend()
plt.show()
```

A.3 Calculation of the Bond Number

The Bond number (Bo) is a ratio of gravitational to surface tension forces. A value less than one typically indicates that surface tension dominates over gravity. The Bond number is represented by the following equation:

$$Bo = \frac{gL^2(\rho_L - \rho_g)}{\sigma}, \tag{A.1}$$

where g is the acceleration due to gravity (taken here as 9.81ms$^-$1), L is the characteristic length (here taken as the bridge height[1]), ρ_L is the liquid density,

ρ_g is the gas density σ is the surface tension of the liquid. Bo is 0.175 for a CLB at minimum extension (1 mm), and 0.394 for a CLB at maximum extension (1.5 mm). Both Bo numbers are not small when compared to unity, so gravitational effects should be carefully considered in this setup.

A.4 Surface Evolver

Surface Evolver is a program for the modelling of liquid interfaces developed by Kenneth Brakke at the University of Susquehanna [205]. It considers different energies that the system experiences, such as surface tension and gravity, and minimises the total energy, subject to constraints added by the user. These constraints may be setting parameters such as the droplet or CLB volume, adding contact line pinning and/or setting contact angles and surface tensions. The software is freely available online, and is under continuous development and use by the research community. In this thesis, this software is used to model simple liquid droplets and CLB systems, with a view to future work (Chapter 7) focusing on gaining a greater understanding of the shape evolution of sessile drop and CLB systems.

A.4.1 Practical Modelling in Surface Evolver

Practically, the evolution of a surface in Surface Evolver is completed as follows: A mesh consisting of defined vertices, edges and faces is created in a standard notepad processor. The mesh is then evolved carefully and alternately triangulated, smoothed and vertex averaged. Once a mesh of relative stability has been found, the mesh evolves using more automated smoothing and vertex averaging processes. As the mesh evolves over a number of evolutions, the energy slowly reaches a point at which it is stable. Mathematically, when the mesh (here a CLB) is evolving, Surface Evolver is attempting to minimise the following energy equation [110];

$$E = \gamma_{lg} A_{lg} + \gamma_{ls} A_{ls} + \gamma_{gs} A_{gs} - \Delta P_{lg} V_d, \tag{A.2}$$

where γ_{lg} and A_{lg} are the surface tension and interfacial area of the liquid and the gas, γ_{ls} and A_{ls} are the surface tension and interfacial area of the liquid and the solid, γ_{gs} and A_{gs} are the surface tension and interfacial area of the gas and the solid, ΔP_{lg} is the pressure difference between the liquid and gas components and V_d is the volume of the droplet.

A.4.2 Modelling Droplets on Surfaces

Surface Evolver can be used to model droplets on surfaces with constant wettability, or surfaces with wettable strips or patches. Fig. A.5a-d shows the evolution of an initial mesh (Fig. A.5a) consisting of a series of interconnected triangles. It forms a simple cube, and is placed on a surface with a stipulated contact angle. When the droplet interacts with the surface, it adopts the contact angle specified, and evolves to the lowest energy configuration (see Eq. A.2) with respect to this constraint. Fig.A.5b-d show the droplet evolving with the different contact angle constraints (160 degrees, 20 degrees and 90 degrees respectively). Fig.A.5e-h shows similar evolutions, but for a droplet on a wettable strip. For a droplet on a hydrophilic band, the capillary forces in the wetting region tend to stretch the droplet, while the capillary forces in the hydrophobic part pinch the droplet. The surface tension of the droplet is also working to keep the droplet area as small as possible. This can lead to contact line pinning as the droplet interacts with the contact line boundary.

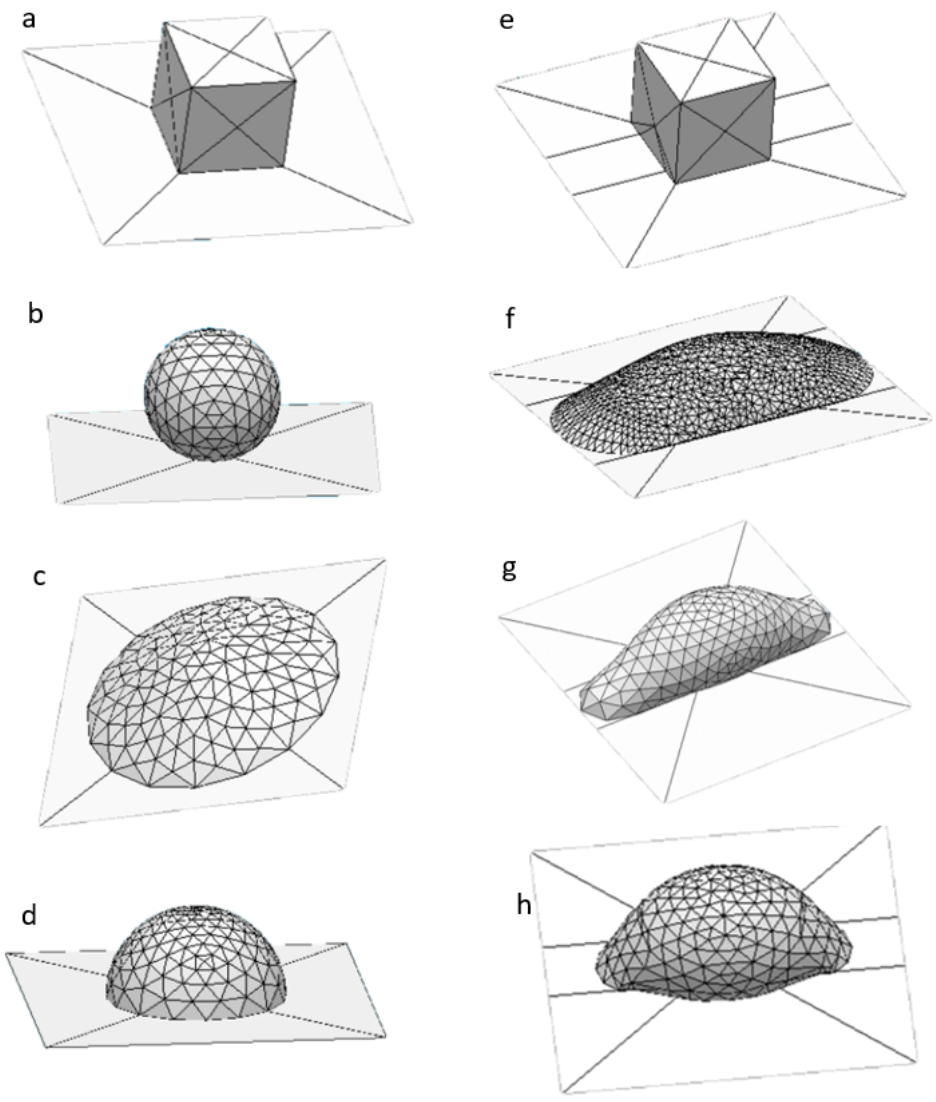

Figure A.5: The evolution of a droplet on a surface with different contact angles (a-d) and for surfaces with wettable strips (e-h). (a) The starting mesh is a cube placed on a surface. (b) The evolution of a droplet with contact angle 160 degrees, (c) 20 degrees, and (d) 90 degrees.For droplets placed on wettable strips, (e) the starting mesh is placed on the wettable strip. (f) The droplet is evolved with an interior angle of 30 degrees and exterior angle of 120 degrees, the droplet spreads along the strip without overflowing onto the other surface. The droplet volume also affects its behaviour on the strip. (g) For a moderate volume droplet with interior angle of 60 and an exterior angle of 120, the droplet remains in a bulged state. (h) For a large volume droplet, with exterior angle of 120 and an interior angle of 60 degrees, the droplet may spread over the wettable strip onto the other surface.

A.4.3 Modelling Capillary Liquid Bridges in Surface Evolver

Surface Evolver can also be used to model CLBs. Fig. A.6 is the typical geometry that will be considered in this thesis (CLBs formed between two uniform, parallel plates). From the initial mesh shown in Fig. A.6a, the bridge can be evolved with a constant contact angle, to obtain different bridge shapes (Fig. A.6b-d with angles of 160, 20 and 90 respectively). Stretching of the CLBs can be simulated by changing the position of the top plate. By adding constraints that either replicate pinning (constant radius) or sliding (constant contact angle), a picture of the CLB bridge behaviour can be created under different experimental conditions.

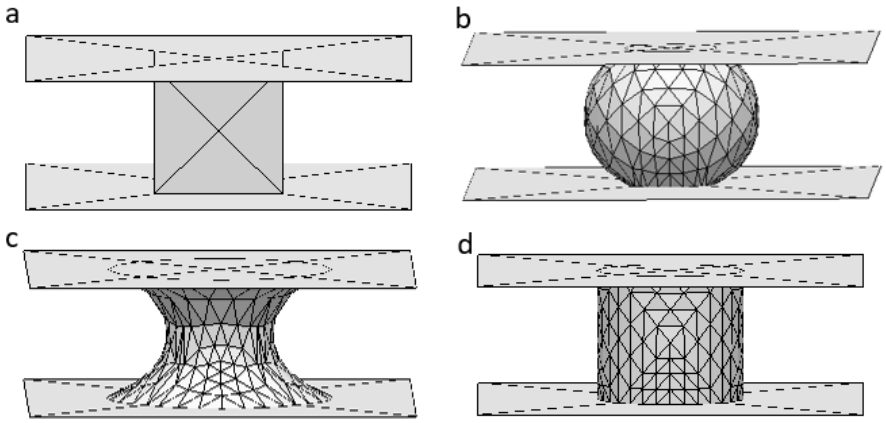

Figure A.6: The evolution of a CLB between parallel plates with different contact angles. (a) The starting mesh is a cube placed between two plates. (b) The CLB evolves with a contact angle of 160 degrees, (c) 20 degrees and (d) 90 degrees.

Bibliography

[1] Jaroslaw W. Drelich, Ludmila Boinovich, Emil Chibowski, Claudio Della Volpe, Lucyna Hołysz, Abraham Marmur, and Stefano Siboni. Contact angles: History of over 200 years of open questions. *Surface Innovations*, 8:3–27, 2020.

[2] Charles W. Extrand. Origins of Wetting. *Langmuir*, 32:7697–7706, 2016.

[3] Jacob J. Bikerman. Capillarity before Laplace :Clairaut, Segner, Monge, Young. *Archive for History of Exact Sciences*, 18:103–122, 1978.

[4] Benjamin Franklin, William Brownrigg, and Rev. Farish. XLIV. Of the stilling of waves by means of oil. Extracted from sundry letters between Benjamin Franklin, LL. D. F. R. S. William Brownrigg, M. D. F. R. S. and the Reverend Mr. Farish. *Philosophical Transactions of the Royal Society of London*, 64, 1774.

[5] Francis Hauksbee. An experiment made at Gresham-College, showing that the seemingly spontaneous ascention of water in small tubes open at both ends is the same in vacuo as in the open air. *Philosophical Transactions of the Royal Society of London*, 25:2223–2224, 1706.

[6] James Jurin. An account of some experiments shown before the Royal Society; With an enquiry into the cause of the ascent and suspension of water in capillary tubes. *Philosophical Transactions of the Royal Society of London*, 30:739–474, 1717.

[7] Tharwat Tadros. Definition of liquid-liquid interface. *Encyclopedia of Colloid and Interface Science*, pages 635–636, 2013.

[8] Tharwat Tadros. Definition of solid-liquid interface. *Encyclopedia of Colloid and Interface Science*, pages 636–636, 2013.

[9] Thomas Young. An essay on the cohesion of fluids. *Philosophical Transactions of the Royal Society of London*, 95:65–87, 1804.

[10] Pierre S. Laplace. Traité de méchanique céleste. Supplement to the tenth book in vol. IV. Imprim. Imperiale, Paris 18, 1805.

[11] John W. S. Rayleigh. On the tension of water surfaces, clean and contaminated, investigated by the method of ripples. *The London, Edinburgh, and Dublin Philosophical Magazine and Journal of Science*, 30:386–400, 1890.

[12] Agnes Pockels. Uber randwinkel und ausbreitung von flussigkeiten auf festen korpern. *Physikalische Zeitschrift*, 15:39–46, 1914.

[13] Henry L. Sulman. A contribution to the study of flotation. *Transactions of the Institution of Mining and Metallurgy*, 29:44–138, 1919.

[14] Robert N. Wenzel. Resistance of solid surfaces to wetting by water. *Industrial and Engineering Chemistry*, 28:988–994, 1936.

[15] A. B. D. Cassie and S. Baxter. Wettability of porous surfaces. *Transactions of the Faraday Society*, 40(5):546–551, 1944.

[16] Jiale Yong, Feng Chen, Qing Yang, Jinglan Huo, and Xun Hou. Superoleophobic surfaces. *Chemical Society Reviews*, 46:4168–4217, 2017.

[17] Zhenghui Qiu, Ri Qiu, Yamei Xiao, Jiyong Zheng, and Cunguo Lin. Slippery liquid-infused porous surface fabricated on CuZn: A barrier to abiotic seawater corrosion and microbiologically induced corrosion. *Applied Surface Science*, 457:468–476, 2018.

[18] Sam Peppou-Chapman, Jun Ki Hong, Anna Waterhouse, and Chiara Neto. Life and death of liquid-infused surfaces: A review on the choice, analysis

and fate of the infused liquid layer. *Chemical Society Reviews*, 49:3688–3715, 2020.

[19] Gaoqiang Shi, Yitian Wang, Soroosh Derakhshanfar, Kaige Xu, Wen Zhong, Gaoxing Luo, Tengfei Liu, Ying Wang, Jun Wu, and Malcolm Xing. Biomimicry of oil infused layer on 3D printed poly(dimethylsiloxane): Non-fouling, antibacterial and promoting infected wound healing. *Materials Science and Engineering C*, 100:915–927, 2019.

[20] Meiling Zhang, Qi Liu, Jingyuan Liu, Jing Yu, and Jun Wang. Self-healing liquid-infused surfaces with high transparency for optical devices. *Materials Research Society Communications*, 9:92–98, 2019.

[21] Junsheng Li, Erica Ueda, Dorothea Paulssen, and Pavel A. Levkin. Slippery lubricant-infused surfaces: Properties and emerging applications. *Advanced Functional Materials*, 29:1–13, 2019.

[22] Wei Wang, Qi Wang, Jia Zhou, and Antoine Riaud. Observation of contact angle hysteresis due to inhomogeneous electric fields. *Communications Physics*, 4:3–10, 2021.

[23] Charles W. Extrand. Model for contact angles and hysteresis on rough and ultraphobic surfaces. *Langmuir*, 18:7991–7999, 2002.

[24] Pierre G. De Gennes. Wetting: Statics and dynamics. *Reviews of Modern Physics*, 57:827–863, 1985.

[25] Emil Chibowski and Malgorzata Jurak. Comparison of contact angle hysteresis of different probe liquids on the same solid surface. *Colloid and Polymer Science*, 291:391–399, 2013.

[26] Rossen V. Sedev, Jordan G. Petrov, and August W. Neumann. Effect of swelling of a polymer surface on advancing and receding contact angles. *Journal of Colloid and Interface Science*, 180:36–42, 1996.

[27] Husseyin B. Eral, Dietrich J.C.M. 'T Mannetje, and Jung Min Oh. Contact angle hysteresis: A review of fundamentals and applications. *Colloid and Polymer Science*, 291:247–260, 2013.

[28] Metin Hatipogullari, Christophe Wylock, Marc Pradas, Serafim Kalliadasis, and Pierre Colinet. Contact angle hysteresis in a microchannel: Statics. *Physical Review Fluids*, 4:1–21, 2019.

[29] Dileep Mampallil and Huseyin B. Eral. A review on suppression and utilization of the coffee-ring effect. *Advances in Colloid and Interface Science*, 252:38–54, 2018.

[30] Shyamashis Das, Atreya Dey, Govardhan Reddy, and D. D. Sarma. Suppression of the coffee-ring effect and evaporation-driven disorder to order transition in colloidal droplets. *Journal of Physical Chemistry Letters*, 8:4704–4709, 2017.

[31] Ciro Semprebon, Glen McHale, and Halim Kusumaatmaja. Apparent contact angle and contact angle hysteresis on liquid infused surfaces. *Soft Matter*, 13:101–110, 2017.

[32] Daniel C. Pease. The significance of the contact angle in relation to the solid surface. *Journal of Physical Chemistry*, 49:107–110, 1945.

[33] Lichao Gao and Thomas J. McCarthy. How Wenzel and Cassie were wrong. *Langmuir*, 23:3762–3765, 2007.

[34] Charles W. Extrand. Contact angles and hysteresis on surfaces with chemically heterogeneous islands. *Langmuir*, 19:3793–3796, 2003.

[35] Nuno M. Oliveira, Ana I. Neto, Wenlong Song, and João F. Mano. Two-dimensional open microfluidic devices by tuning the wettability on patterned superhydrophobic polymeric surface. *Applied Physics Express*, 3:2–5, 2010.

[36] Xinxing Lin, Wei Ma, Lihui Chen, Liulian Huang, Hui Wu, and Atsushi Takahara. Influence of water evaporation/absorption on the stability of glycerol-water marbles. *Royal Society of Chemistry Advances*, 9:34465–34471, 2019.

[37] Tengfei Xiang, Min Zhang, Hisham-Rabia Sadig, Zecai Li, Manxin Zhang, Chundong Dong, Ling Yang, Wenming Chan, and Cheng Li. Slippery liquid-infused porous surface for corrosion protection with self-healing property. *Chemical Engineering Journal*, 345:147–155, 2018.

[38] Zhijun Song, Lotte Borgwardt, Niels Høiby, Hong Wu, Torben Sandberg Sørensen, and Arne Borgwardt. Prosthesis infections after orthopedic joint replacement: the possible role of bacterial biofilms. *Orthopedic Reviews*, 5:65–71, 2013.

[39] Alexander Besinis, Sanna D. Hadi, Huirong. Le, Christopher Tredwin, and Richard D. Handy. Antibacterial activity and biofilm inhibition by surface modified titanium alloy medical implants following application of silver, titanium dioxide and hydroxyapatite nanocoatings. *Nanotoxicology*, 11:327–338, 2017.

[40] Qinglang Ma, Hongfei Cheng, Anthony G. Fane, Rong Wang, and Hua Zhang. Recent development of advanced materials with special wettability for selective oil/water separation. *Small*, 12:2186–2202, 2016.

[41] Sumit Parvate, Prakhar Dixit, and Sujay Chattopadhyay. Superhydrophobic surfaces: Insights from theory and experiment. *Journal of Physical Chemistry B*, 124:1323–1360, 2020.

[42] Xin Zhou, Yeong Y. Lee, Karen S. L. Chong, and Chaobin He. Superhydrophobic and slippery liquid-infused porous surfaces formed by the self-assembly of a hybrid ABC triblock copolymer and their antifouling performance. *Journal of Materials Chemistry B*, 6:440–448, 2018.

[43] Katrina M. Wisdom, Jolanta A. Watson, Xiaopeng Qu, Fangjie Liu, Gregory S. Watson, and Chuan Hua Chen. Self-cleaning of superhydrophobic surfaces by self-propelled jumping condensate. *Proceedings of the National Academy of Sciences of the United States of America*, 110:7992–7997, 2013.

[44] Xiaodong Yu, Junling Zhao, Chengjiao Wu, Bin Li, Chenbo Sun, Shilin Huang, and Xuelin Tian. Highly durable antifogging coatings resistant to long-term airborne pollution and intensive UV irradiation. *Materials and Design*, 194:108956–108966, 2020.

[45] Adel M.A. Mohamed, Aboubakr M. Abdullah, and Nathalie A. Younan. Cor-

rosion behavior of superhydrophobic surfaces: A review. *Arabian Journal of Chemistry*, 8:749–765, 2015.

[46] Yehia E. Elmogahzy. Chapter 11 - finished fibrous assemblies. In *Engineering Textiles (Second Edition)*, The Textile Institute Book Series, pages 275–298. Woodhead Publishing, 2020.

[47] Jaroslaw Drelich and Emil Chibowski. Superhydrophilic and superwetting surfaces: Definition and mechanisms of control. *Langmuir*, 26:18621–18623, 2010.

[48] Kerstin Koch, Bharat Bhushan, and Wilhelm Barthlott. Multifunctional surface structures of plants: An inspiration for biomimetics. *Progress in Materials Science*, 54:137–178, 2009.

[49] Huaqiang He, Tian C. Zhang, Zhikai Li, Ying Liang, and Shaojun Yuan. Superhydrophilic fish-scale-like CuC2O4 nanosheets wrapped copper mesh with underwater super oil-repellent properties for effective separation of oil-in-water emulsions. *Colloids and Surfaces A: Physicochemical and Engineering Aspects*, 627:127133, 2021.

[50] Jaeho Choi, Wonhee Jo, Seung Yeol Lee, Yeon Sik Jung, Shin Hyun Kim, and Hee Tak Kim. Flexible and robust superomniphobic surfaces created by localized photofluidization of azopolymer pillars. *American Chemical Society: Nano*, 11:7821–7828, 2017.

[51] Donghui Wang, Hongyu Liu, Jinlong Yang, and Shuxue Zhou. Seawater-induced healable underwater superoleophobic antifouling coatings. *American Chemical Society: Applied Materials and Interfaces*, 11:1353–1362, 2019.

[52] Kapil Manoharan and Shantanu Bhattacharya. Superhydrophobic surfaces review: Functional application, fabrication techniques and limitations. *Journal of Micromanufacturing*, 2:59–78, 2019.

[53] Yasmin A. Mehanna, Emma Sadler, Rebekah L. Upton, Andrew G. Kempchinsky, Yao Lu, and Colin R. Crick. The challenges, achievements and

applications of submersible superhydrophobic materials. *Chemical Society Reviews*, 50:6569–6612, 2021.

[54] Konica Sharma, Amrita Hooda, Manjeet S. Goyat, Radheshyam Rai, and Ajay Mittal. A review on challenges, recent progress and applications of silica nanoparticles based superhydrophobic coatings. *Ceramics International*, 48:5922–5938, 2021.

[55] Tak Sing Wong, Sung Hoon Kang, Sindy K.Y. Tang, Elizabeth J. Smythe, Benjamin D. Hatton, Alison Grinthal, and Joanna Aizenberg. Bioinspired self-repairing slippery surfaces with pressure-stable omniphobicity. *Nature*, 477:443–447, 2011.

[56] David Quéré. Non-sticking drops. *Reports on Progress in Physics*, 68:2495–2532, 2005.

[57] Anaïs Gauthier, Sean Symon, Christophe Clanet, and David Quéré. Water impacting on superhydrophobic macrotextures. *Nature Communications*, 6:8001, 2015.

[58] Ingo Scholz, Matthias Bückins, Lars Dolge, Thomas Erlinghagen, Anges Weth, Florian Hischen, Joachim Mayer, Sandra Hoffmann, Markus Riederer, Michael Riedel, and Werner Baumgartner. Slippery surfaces of pitcher plants: Nepenthes wax crystals minimize insect attachment via microscopic surface roughness. *Journal of Experimental Biology*, 213:1115–1125, 2010.

[59] Sittavee Borwonjatuwich. Botanical Illustration. *Website*, https://www.pinterest.co.uk/lllllloyd/botanical-illustration/, accessed 2018.

[60] David Tesler, Philseok Kim, Stephan Kolle, Caitlin Howell, Ahanotu Onye, and Joanne Aizenberg. Extremely durable biofouling-resistant metallic surfaces based on electrodeposited nanoporous tungstite films on steel. *Nature Communications*, 6:8649, 2015.

[61] Ranit Mukherjee, Mohammad Habibi, Ziad Rashed, Berbert Otacilio, Xi-

angke Shi, and Jonathan Boreyko. Oil-impregnated hydrocarbon-based polymer films. *Scientific Reports*, 8:11698–11705, 2018.

[62] Philseok Kim, Tak-sing Wong, Jack Alvarenga, Michael J Kreder, Wilmer E Adorno-martinez, and Joanna Aizenberg. Liquid-infused nanostructured surfaces with extreme anti-ice and anti-frost performance. *American Chemical Society: Nano*, 6:6569–6577, 2012.

[63] Boor S. Lalia, Sushant Anand, Kripa Varanasi, and Raed Hashaikeh. Fog-harvesting potential of lubricant-impregnated electrospun nanomats. *Langmuir*, 29:13081–13088, 2018.

[64] Marcus Goudie, Jitendra Pant, and Hitesh Handa. Liquid-infused nitric oxide-releasing (LINORel) silicone for decreased fouling, thrombosis, and infection of medical devices. *Scientific Reports*, 7:13623–13630, 2017.

[65] Jiaqian Li, Huanxi Zheng, Zhengbao Yang, and Zuankai Wang. Breakdown in the directional transport of droplets on the peristome of pitcher plants. *Physics Communications*, 35:1–8, 2018.

[66] Alexander K Epstein, Tak-Sing Wong, Rebecca A Belisle, Emily-Marie Boggs, and Joanna Aizenberg. Liquid-infused structured surfaces with exceptional anti-biofouling performance. *Proceedings of the National Academy of Sciences of the United States of America*, 109:13182–13187, 2012.

[67] J. David Smith, Rajeev Dhiman, Sushant Anand, Ernesto Reza-Garduno, Robert E. Cohen, Gareth H. McKinley, and Kripa K. Varanasi. Droplet mobility on lubricant-impregnated surfaces. *Soft Matter*, 9:1772–1780, 2013.

[68] Martin Villegas, Yuxi Zhang, Noor Abu Jarad, Leyla Soleymani, and Tohid F. Didar. Liquid-infused surfaces: A review of theory, design, and applications. *American Chemical Society: Nano*, 13:8517–8536, 2019.

[69] Philseok Kim, Michael J. Kreder, Jack Alvarenga, and Joanna Aizenberg. Hierarchical or not? Effect of the length scale and hierarchy of the surface roughness on omniphobicity of lubricant-infused substrates. *Nano Letters*, 13(4):1793–1799, 2013.

[70] Nithi Atthi, Mantana Suwan, Nuchjarin Sangwong, Pattaraluck Pattamang, Witsaroot Sripumkhai, Rattanawan Meananeatra, Pawasuth Saengdee, Oraphan Thongsook, Norabadee Ranron, Krynnaras Pankong, Warinrampai Uahchinkul, Wutthinan Jeamsaksiri, and Sitthisuntorn Supothina. Fabrication of slippery liquid-infused porous surfaces for anti-fouling applications. *Japanese Journal of Applied Physics*, 60, 2021.

[71] Nguyen Van Minh, Dang Van Hieu, Pham Van Tuan, Nguyen Duc Dung, and Chu Manh Hoang. Characteristics of silicon nano-pillars fabricated by nanosphere lithography and metal assisted chemical etching. *Materials Science in Semiconductor Processing*, 142(December 2021):106483, 2022.

[72] Hoang Tuan Nguyen, Ha Thach, Emmanuel Roy, Khon Huynh, and Cecile Mong Tu Perrault. Low-cost, accessible fabrication methods for microfluidics research in low-resource settings. *Micromachines*, 9(9):1–10, 2018.

[73] Mahmut TAS, Halar Memon, Fang Xu, Ifty Ahmed, and Xianghui Hou. Electrospun nanofibre membrane based transparent slippery liquid-infused porous surfaces with icephobic properties. *Colloids and Surfaces A: Physicochemical and Engineering Aspects*, 585:1–18, 2020.

[74] Sarah J. Goodband, Steven Armstrong, Halim Kusumaatmaja, and Kislon Voïtchovsky. Effect of ageing on the structure and properties of model liquid-infused surfaces. *Langmuir*, 36:3461–3470, 2020.

[75] Yibo Ouyang, Jin Zhao, Ri Qiu, Shugang Hu, Ming Chen, and Peng Wang. Liquid-infused superhydrophobic dendritic silver matrix: A bio-inspired strategy to prohibit biofouling on titanium. *Surface and Coatings Technology*, 367(February):148–155, 2019.

[76] Amin Hosseini, Martin Villegas, Jie Yang, Maryam Badv, Jeffrey I. Weitz, Leyla Soleymani, and Tohid F. Didar. Conductive Electrochemically Active Lubricant-Infused Nanostructured Surfaces Attenuate Coagulation and Enable Friction-Less Droplet Manipulation. *Advanced Materials Interfaces*, 5(18), 2018.

[77] Daheng Wang, Zhiguang Guo, and Weimin Liu. Bioinspired edible lubricant-infused surface with liquid residue reduction properties. *American Association for the Advancement of Science: Research*, 5:1–12, 2019.

[78] Cong Liu, Yunlai Li, Chenguang Lu, Ying Liu, Shile Feng, and Yahua Liu. Robust slippery liquid-infused porous network surfaces for enhanced anti-icing/deicing performance. *American Chemical Society: Applied Materials and Interfaces*, 12:25471–25477, 2020.

[79] Ralf Blossey. Self-cleaning surfaces - virtual realities. *Nature Materials*, 2:301–306, 2003.

[80] Yong Han Yeong, Chenyu Wang, Kenneth J. Wynne, and Mool C. Gupta. Oil-infused superhydrophobic silicone material for low ice adhesion with long-term infusion stability. *American Chemical Society: Applied Materials and Interfaces*, 8:32050–32059, 2016.

[81] Jason S. Wexler, Abigail Grosskopf, Melissa Chow, Yuyang Fan, Ian Jacobi, and Howard A. Stone. Robust liquid-infused surfaces through patterned wettability. *Soft Matter*, 11:5023–5029, 2015.

[82] Jason S. Wexler, Ian Jacobi, and Howard A. Stone. Shear-driven failure of liquid-infused surfaces. *Physical Review Letters*, 114:168301–168306, 2015.

[83] Ying Liu, Jason S. Wexler, Clarissa Schönecker, and Howard A. Stone. Effect of viscosity ratio on the shear-driven failure of liquid-infused surfaces. *Physical Review Fluids*, 1:074003–074019, 2016.

[84] Vickramjeet Singh, Yu Jane Sheng, and Heng Kwong Tsao. Self-healing atypical liquid-infused surfaces: Superhydrophobicity and superoleophobicity in submerged conditions. *Journal of the Taiwan Institute of Chemical Engineers*, 97:96–104, 2019.

[85] Cameron S. Ware, Truis Smith-Palmer, Sam Peppou-Chapman, Liam R.J. Scarratt, Erin M. Humphries, Daniel Balzer, and Chiara Neto. Marine antifouling behavior of lubricant-infused nanowrinkled polymeric surfaces.

American Chemical Society: Applied Materials and Interfaces, 10:4173–4182, 2018.

[86] Youfa Zhang, Liqing Zhang, Zhen Xiao, Shanlin Wang, and Xinquan Yu. Fabrication of robust and repairable superhydrophobic coatings by an immersion method. *Chemical Engineering Journal*, 369:1–7, 2019.

[87] Caitlin Howell, Thy L. Vu, Christopher P. Johnson, Xu Hou, Onye Ahanotu, Jack Alvarenga, Daniel C. Leslie, Oktay Uzun, Anna Waterhouse, Philseok Kim, Michael Super, Michael Aizenberg, Donald E. Ingber, and Joanna Aizenberg. Stability of surface-immobilized lubricant interfaces under flow. *Chemistry of Materials*, 27:1792–1800, 2015.

[88] Huijie Wang, Xiaoxun Li, Kang Luan, and Xilin Bai. Capillary liquid bridge soft lithography for micro-patterning preparation based on SU-8 photoresist templates with special wettability. *Royal Society of Chemisty Advances*, 9:23986–23993, 2019.

[89] Mark D. Zoback and Arjun H. Kohli. Unconventional reservoir geomechanics: Shale gas, tight oil, and induced seismicity. *Cambridge University Press*, pages 1–484, 2019.

[90] Tingtao Zhou, Katerina Ioannidou, Franz J. Ulm, Martin Z. Bazant, and Roland J.M. Pellenq. Multiscale poromechanics of wet cement paste. *Proceedings of the National Academy of Sciences of the United States of America*, 166:10652–10657, 2019.

[91] Shiyao Bian, Cheng-Feng Tai, David Halpern, Yi Zheng, and James B. Grotberg. Experimental study of flow fields in an airway closure model. *Journal of Fluid Mechanics*, 647:391–402, 2010.

[92] Matthias Heil, Andrew L. Hazel, and Jaclyn A. Smith. The mechanics of airway closure. *Respiratory Physiology and Neurobiology*, 163:214–221, 2008.

[93] Daniel J. Hornbaker, Rita R. Albert, Istvan Albert, Albert L. Barabasi, and Peter Schiffer. What keeps sandcastles standing? *Nature*, 387:765–769, 1997.

[94] Meng Li, Liping Shi, and Xiaolei Wang. Physical mechanisms behind the wet adhesion: From amphibian toe-pad to biomimetics. *Colloids and Surfaces B: Biointerfaces*, 199:111531–111541, 2021.

[95] Walter Federle, Mathis Riehle, Adam S.G. Curtis, and Robert J. Full. An integrative study of insect adhesion: Mechanics and wet adhesion of pretarsal pads in ants. *Integrative and Comparative Biology*, 42:1100–1106, 2002.

[96] Manu Prakash, David Quéré, and John W.M. Bush. Surface tension transport of prey by feeding shorebirds: The capillary ratchet. *Science*, 320:931–934, 2008.

[97] Etienne Portuguez, Arnaud Alzina, Philippe Michaud, Djamila Hourlier, and Agnès Smith. Study of the contact and the evaporation kinetics of a thin water liquid bridge between two hydrophobic plates. *Advances in Materials Physics and Chemistry*, 7:99–112, 2017.

[98] Zhang Shi, Yi Zhang, Mingchao Liu, Dorian A.H. Hanaor, and Yixiang Gan. Dynamic contact angle hysteresis in liquid bridges. *Colloids and Surfaces A: Physicochemical and Engineering Aspects*, 555:365–371, 2018.

[99] Xukun He, Jiangtao Cheng, C. Patrick Collier, Bernadeta R. Srijanto, and Dayrl P. Briggs. Evaporation of squeezed water droplets between two parallel hydrophobic/superhydrophobic surfaces. *Journal of Colloid and Interface Science*, 576:127–138, 2020.

[100] Emerson J. De Souza, Martin Brinkmann, Camilla Mohrdieck, Alan Crosby, and Eduard Arzt. Capillary forces between chemically different substrates. *Langmuir*, 24:10161–10168, 2008.

[101] Xukun He and Jiangtao Cheng. Evaporation-triggered directional transport of asymmetrically confined droplets. *Journal of Colloid and Interface Science*, 604:550–561, 2021.

[102] Xiongheng Bian, Haibo Huang, and Liguo Chen. Motion of droplets into hydrophobic parallel plates. *Royal Society of Chemistry Advances*, 9:32278–32287, 2019.

[103] Emerson J. De Souza, Lixin Gao, J. McCarthy, Eduard Arzt, and Alan J. Crosby. Effect of contact angle hysteresis on the measurement of capillary forces. *Langmuir*, 24:1391–1396, 2008.

[104] Yongxin Wang, Stephen Michielsen, and Hoon Joo Lee. Symmetric and asymmetric capillary bridges between a rough surface and a parallel surface. *Langmuir*, 29:11028–11037, 2013.

[105] Geoffrey Mason and W. C. Clark. Liquid bridges between spheres. *Chemical Engineering Science*, 20:859–866, 1965.

[106] Yakov I. Rabinovich, Madhavan S. Esayanur, and Brij M. Moudgil. Capillary forces between two spheres with a fixed volume liquid bridge: Theory and experiment. *Langmuir*, 21:10992–10997, 2005.

[107] Paulo I.C. Teixeira and Miguel A.C. Teixeira. The shape of two-dimensional liquid bridges. *Journal of Physics Condensed Matter*, 32:034002–034009, 2020.

[108] Huang Chen, Alidad Amirfazli, and Tian Tang. Modeling liquid bridge between surfaces with contact angle hysteresis. *Langmuir*, 29:3310–3319, 2013.

[109] Muhammad S. Sadullah, Jack R. Panter, and Halim Kusumaatmaja. Factors controlling the pinning force of liquid droplets on liquid infused surfaces. *Soft Matter*, 16:8114–8121, 2020.

[110] Alvin Shek, Ciro Semprebon, Jack R. Panter, and Halim Kusumaatmaja. Capillary bridges on liquid-infused surfaces. *Langmuir*, 37:908–917, 2021.

[111] Plamen V. Petkov and Boryan Radoev. Investigation of single and binary of "sandwich" type convex liquid capillary bridges, stretched between two flat surfaces (Experimental approach). *Colloids and Interfaces*, 3:68–74, 2019.

[112] Halim Kusumaatmaja and Reinhard Lipowsky. Equilibrium morphologies and effective spring constants of capillary bridges. *Langmuir*, 26:18734–18741, 2010.

[113] Heiko K. Cammenga, Friedrick W. Schulze, and Wilheim Theuerl. Vapor pressure and evaporation coefficient of glycerol. *Journal of Chemical and Engineering Data*, 22:131–133, 1977.

[114] Logan Lecoq, Denis Flick, and Onrawee. Laguerre. Study of the water evaporation rate on stainless steel plate in controlled conditions. *International Journal of Thermal Sciences*, 111:450–462, 2017.

[115] Jie Qu, Luis Escobar, Jianzhi Li, Zhonghao Rao, and Ben Xu. Experimental study of evaporation and crystallization of brine droplets under different temperatures and humidity levels. *International Communications in Heat and Mass Transfer*, 110:104427–104432, 2020.

[116] Dan Daniel, Jaakko V.I. Timonen, Ruoping Li, Seneca J. Velling, and Joanna Aizenberg. Oleoplaning droplets on lubricated surfaces. *Nature Physics*, 13:1020–1025, 2017.

[117] Armelle Keiser, Ludovic Keiser, Christophe Clanet, and David Quéré. Drop friction on liquid-infused materials. *Soft Matter*, 13:6981–6987, 2017.

[118] Frank Schellenberger, Jing Xie, Noemí Encinas, Alexandre Hardy, Markus Klapper, Periklis Papadopoulos, Hans Jürgen Butt, and Doris Vollmer. Direct observation of drops on slippery lubricant-infused surfaces. *Soft Matter*, 11:7617–7626, 2015.

[119] Masahiro Kato, Akinori Tanaka, Masahiro Sasagawa, and Hiromitsu Adachi. Patent:WO2009113978A1, Durable automotive windshield coating and the use thereof, 2008.

[120] Bethany V. Orme, Glen McHale, Rodrigo Ledesma-Aguilar, and Gary G. Wells. Droplet retention and shedding on slippery substrates. *Langmuir*, 35:9146–9151, 2019.

[121] Renhua Deng, Lisong Yang, and Colin D. Bain. Combining inkjet printing with emulsion solvent evaporation to pattern polymeric particles. *American Chemical Society: Applied Materials and Interfaces*, 10:12317–12322, 2018.

[122] Alfred G. Emslie, Francis T. Bonner, and Leslie G. Peck. Flow of a viscous liquid on a rotating disk. *Journal of Applied Physics*, 29:858–862, 1958.

[123] Joseph D. Berry, Michael J. Neeson, Raymond R. Dagastine, Derek Y.C. Chan, and Rico F. Tabor. Measurement of surface and interfacial tension using pendant drop tensiometry. *Journal of Colloid and Interface Science*, 454:226–237, 2015.

[124] Adrian Daerr and Adrien Mogne. Measuring liquid surface tension through the pendent drop method: description of a measurement bench and an ImageJ Plugin. *Journal of Open Research Software*, 4:1–12, 2016.

[125] Blaise Pascal. Traitez de l'Equilibre des Liqueurs (Treatise on the Equilibrium of Fluids). pages 361–370, 1663.

[126] Madhu Ranjan Gunjan, Alok Kumar, and Rishi Raj. Cloaked droplets on lubricant-infused surfaces: Union of constant mean curvature interfaces dictated by thin-film tension. *Langmuir*, 37:6601–6612, 2021.

[127] Aurélien F. Stalder, Gerit Kulik, Daniel Sage, Laura Barbieri, and Patrik Hoffmann. A snake-based approach to accurate determination of both contact points and contact angles. *Colloids and Surfaces A: Physicochemical and Engineering Aspects*, 286:92–103, 2006.

[128] Aurélien F. Stalder, Tobias Melchior, Michael Müller, Daniel Sage, Thierry Blu, and Michael Unser. Low-bond axisymmetric drop shape analysis for surface tension and contact angle measurements of sessile drops. *Colloids and Surfaces A: Physicochemical and Engineering Aspects*, 364:72–81, 2010.

[129] Marco Brugnara. Measuring the Contact Angle using ImageJ with Contact Angle plug-in. *FIJI plugin*, 2006.

[130] José L. Pérez-Díaz, Marco A. Álvarez-Valenzuela, and Juan C. García-Prada. The effect of the partial pressure of water vapor on the surface tension of the liquid water-air interface. *Journal of Colloid and Interface Science*, 381:180–182, 2012.

[131] Etienne Portuguez, Arnaud Alzina, Philippe Michaud, Maksoud Oudjedi, and Agnès Smith. Evolution of a water pendant droplet: Effect of temperature and relative humidity. *Natural Science*, 9:1–20, 2017.

[132] Gerd Binnig, Calvin F. Quate, and Christoph Geber. Atomic Force Microscopy. *Physical Review Letters*, 56:930–934, 1986.

[133] Nader Jalili and Karthik Laxminarayana. A review of atomic force microscopy imaging systems: application to molecular metrology and biological sciences. *Mechatronics*, 14:907–945, 2004.

[134] Shaoyang Liu and Yifen Wang. Chapter 6: A review of the application of atomic force microscopy (afm) in food science and technology. volume 62 of *Advances in Food and Nutrition Research*, pages 201–240. Academic Press, 2011.

[135] Andrea Alessandrini and Paolo Facci. AFM: A versatile tool in biophysics. *Measurement Science and Technology*, 16:65–92, 2005.

[136] Taku Yamazaki, Mizuki Tenjimbayashi, Kengo Manabe, Takeo Moriya, Hiroki Nakamura, Takuto Nakamura, Takeshi Matsubayashi, Yosuke Tsuge, and Seimei Shiratori. Antifreeze liquid-infused surface with high transparency, low ice adhesion strength, and antifrosting properties fabricated through a spray layer-by-layer method. *Industrial and Engineering Chemistry Research*, 58:2225–2234, 2019.

[137] Matt K. Fu, Isnardo Arenas, Stefano Leonardi, and Marcus Hultmark. Liquid-infused surfaces as a passive method of turbulent drag reduction. *Journal of Fluid Mechanics*, 824:688–700, 2017.

[138] Xianming Dai, Nan Sun, Steven O. Nielsen, Birgitt Boschitsch Stogin, Jing Wang, Shikuan Yang, and Tak Sing Wong. Hydrophilic directional slippery rough surfaces for water harvesting. *Science Advances*, 4(3):1–11, 2018.

[139] Xi Yao, Yuhang Hu, Alison Grinthal, Tak Sing Wong, L. Mahadevan, and Joanna Aizenberg. Adaptive fluid-infused porous films with tunable transparency and wettability. *Nature Materials*, 12:529–534, 2013.

[140] José. Bico, Charles Tordeux, and David Quéré. Rough wetting. *Europhysics Letters*, 55:214–220, 2001.

[141] Sushant Anand, Konrad Rykaczewski, Srinivas B. Subramanyam, Daniel Beysens, and Kripa K. Varanasi. How droplets nucleate and grow on liquids and liquid impregnated surfaces. *Soft Matter*, 11:69–80, 2015.

[142] Wendong Wang, Jaakko V.I. Timonen, Andreas Carlson, Dirk Michael Drotlef, Cathy T. Zhang, Stefan Kolle, Alison Grinthal, Tak Sing Wong, Benjamin Hatton, Sung Hoon Kang, Stephen Kennedy, Joshua Chi, Robert Thomas Blough, Metin Sitti, L. Mahadevan, and Joanna Aizenberg. Multifunctional ferrofluid-infused surfaces with reconfigurable multiscale topography. *Nature*, 559:77–82, 2018.

[143] Dequan Wu, Dawei Zhang, Yuwei Ye, Lingwei Ma, Badar Minhas, Bei Liu, Herman A. Terryn, Johannes M.C. Mol, and Xiaogang Li. Durable lubricant-infused anodic aluminum oxide surfaces with high-aspect-ratio nanochannels. *Chemical Engineering Journal*, 368:138–147, 2019.

[144] Muhammad S. Sadullah, Ciro Semprebon, and Halim Kusumaatmaja. Drop dynamics on liquid-infused surfaces: The role of the lubricant ridge. *Langmuir*, 34:8112–8118, 2018.

[145] Zuzana Brabcova, Glen McHale, Gary G. Wells, Carl V. Brown, and Michael I. Newton. Electric field induced reversible spreading of droplets into films on lubricant impregnated surfaces. *Applied Physics Letters*, 110:121603, 2017.

[146] Ethan J. Miller, William Trewby, Amir F. Payam, Luca Piantanida, Clodomiro Cafolla, and Kislon Voïtchovsky. Sub-nanometer resolution imaging with amplitude-modulation atomic force microscopy in liquid. *Journal of Visualized Experiments*, 2016:1–10, 2016.

[147] Maria Ricci, Roy A. Quinlan, and Kislon Voïtchovsky. Sub-nanometre mapping of the aquaporin-water interface using multifrequency atomic force microscopy. *Soft Matter*, 13:187–195, 2017.

[148] Xin Xu, John Melcher, Sudipta Basak, Ron Reifenberger, and Arvind Raman. Compositional contrast of biological materials in liquids using the momentary excitation of higher eigenmodes in dynamic atomic force microscopy. *Physical Review Letters*, 102:13–16, 2009.

[149] Kislon Voïtchovsky. Anharmonicity, solvation forces, and resolution in atomic force microscopy at the solid-liquid interface. *Physical Review E - Statistical, Nonlinear, and Soft Matter Physics*, 88:1–6, 2013.

[150] Huawei Chen, Pengfei Zhang, Liwen Zhang, Hongliang Liu, Ying Jiang, Deyuan Zhang, Zhiwu Han, and Lei Jiang. Continuous directional water transport on the peristome surface of Nepenthes alata. *Nature*, 532:85–89, 2016.

[151] Pengfei Zhang, Liwen Zhang, Huawei Chen, Zhichao Dong, and Deyuan Zhang. Surfaces inspired by the nepenthes peristome for unidirectional liquid transport. *Advanced Materials*, 29:1–7, 2017.

[152] Pengfei Zhang, Huawei Chen, L. Li, Hongliang Liu, Guang Liu, Liwen Zhang, Deyuan Zhang, and Lei Jiang. Bioinspired smart peristome surface for temperature-controlled unidirectional water spreading. *American Chemical Society: Applied Materials and Interfaces*, 9:5645–5652, 2017.

[153] Shan Zhou, Cunlong Yu, Chuxin Li, Zhichao Dong, and Lei Jiang. Programmable unidirectional liquid transport on peristome-mimetic surfaces under liquid environments. *Journal of Materials Chemistry A*, 7:18244–18248, 2019.

[154] Glen McHale, Bethany V. Orme, Gary G. Wells, and Rodrigo Ledesma-Aguilar. Apparent contact angles on lubricant-impregnated surfaces/SLIPS: From superhydrophobicity to electrowetting. *Langmuir*, 35:4197–4204, 2019.

[155] Jose L. Perez-Diaz, Marco A. Alvarez-Valenzuela, Ignacio. Valiente-Blanco, Sergio Jimenez-Lopez, Marta. Palacios-Cuesta, Olga García, Efren Diez-Jimenez, Juan Sanchez-García-Casarrubios, and Christian Cristache. On the influence of relative humidity on the contact angle of a water droplet

on a silicon wafer. *American Society of Mechanical Engineers: International Mechanical Engineering Congress and Exposition, Proceedings*, 7:1–3, 2013.

[156] Leo H. Holfhuisen. Waves in Oceanic and Coastal Waters (first edition). *Campbridge University Press*, 2007.

[157] Annette. Muetze and Jennifer G. Vining. Ocean wave energy conversion - A survey. *Conference Record - IAS Annual Meeting (IEEE Industry Applications Society)*, 3:1410–1417, 2006.

[158] Romain Guigon, Jean J. Chaillout, Thomas Jager, and Ghislain Despesse. Harvesting raindrop energy: Theory. *Smart Materials and Structures*, 17:015038–015046, 2008.

[159] Jui H. Wang, Shui Y. Lien, Jeng R. Ho, Teng K. Shih, Chia Fu Chen, Chien C. Chen, and Wha Tzong Whang. Optical diffusers based on silicone emulsions. *Optical Materials*, 32:374–377, 2009.

[160] Krishnamurthy Sainath and Pallab Ghosh. Stabilization of silicone oil-in-water emulsions by ionic surfactant and electrolytes: The role of adsorption and electric charge at the interface. *Industrial and Engineering Chemistry Research*, 52:15808–15816, 2013.

[161] Musuvathi S. Bobji, Vijay S. Kumar, Ashish Asthana, and Raghuraman N. Govardhan. Underwater sustainability of the "Cassie" state of wetting. *Langmuir*, 25:12120–12126, 2009.

[162] Mike Wei, Robert S. Bowman, John L. Wilson, and Norman R. Morrow. Wetting properties and stability of silane-treated glass exposed to water, air, and oil. *Journal of Colloid And Interface Science*, 157:154–159, 1993.

[163] Anand V. Ganesh, Hemant K. Raut, Sreekumaran A. Nair, and Seeram Ramakrishna. A review on self-cleaning coatings. *Journal of Materials Chemistry*, 21:16304–16322, 2011.

[164] Bo. N J Persson. Wet adhesion with application to tree frog adhesive toe pads and tires. *Journal of Physics: Condensed Matter*, 19:376110, 2007.

[165] Mahmoud Tamer. Hyaluronan and synovial joint: Function, distribution and healing. *Interdisciplinary Toxicology*, 6:111–125, 2013.

[166] Marina Makrygianni, Elena Margariti, Kostas Andritsos, Dimitrios Reppas, Filimon. Zacharatos, Nikolaos Oikonomidis, Christos Spandonidis, and Ioanna Zergioti. High speed soldering using laser printing for the assembly of electronic components. *Journal of Laser Micro Nanoengineering*, 15:204–208, 2020.

[167] Gert Schouten. Wave soldering of SMDs—A smart approach from science to practice. *Circuit World*, 14:41–44, 1988.

[168] Jinho Kim, Brandon Guenthart, John D. O'Neill, N. Valerio Dorrello, Matthew Bacchetta, and Gordana Vunjak-Novakovic. Controlled delivery and minimally invasive imaging of stem cells in the lung. *Scientific Reports*, 7:1–13, 2017.

[169] Gerson E. Valenzuela. Computer simulation of the effect of wetting conditions on the solvation force and pull-off force of water confined between two flat substrates. *Journal of Physical Chemistry C*, 123:1252–1259, 2019.

[170] Enrique Sahagún, Pedro García-Mochales, Gómez. M. Sacha, and Juan J. Sáenz. Energy dissipation due to capillary interactions: Hydrophobicity maps in force microscopy. *Physical Review Letters*, 98:1–4, 2007.

[171] Akio Fukunishi and Yasushige Mori. Adhesion force between particles and substrate in a humid atmosphere studied by atomic force microscopy. *Advanced Powder Technology*, 17:567–580, 2006.

[172] Mahdi Farshchi-Tabrizi, Michael Kappl, Yajun Cheng, Jochen Gutmann, and Hans Jürgen Butt. On the adhesion between fine particles and nanocontacts: An atomic force microscope study. *Langmuir*, 22:2171–2184, 2006.

[173] Christopher D. Willett, Michael J. Adams, Simon A. Johnson, and Jonathan P.K. Seville. Capillary bridges between two spherical bodies. *Langmuir*, 16:9396–9405, 2000.

[174] Fei Xiao, Jiaqiang Jing, Shibo Kuang, Lu Yang, and Aibing Yu. Capillary forces on wet particles with a liquid bridge transition from convex to concave. *Powder Technology*, 363:59–73, 2020.

[175] David J. Broesch and Joelle Frechette. From concave to convex: Capillary bridges in slit pore geometry. *Langmuir*, 28:15548–15554, 2012.

[176] Etienne Reyssat. Drops and bubbles in wedges. *Journal of Fluid Mechanics*, 748:641–662, 2014.

[177] Ying Chih Liao, Elias I. Franses, and Osman A. Basaran. Deformation and breakup of a stretching liquid bridge covered with an insoluble surfactant monolayer. *Physics of Fluids*, 18:1–21, 2006.

[178] Ying Chih Liao, Hariprasad J. Subramani, Elias I. Franses, and Osman A. Basaran. Effects of soluble surfactants on the deformation and breakup of stretching liquid bridges. *Langmuir*, 20:9926–9930, 2004.

[179] Dominick N Mazzone, Gabriel I Tardos, and Robert Pfeffer. The effect of gravity on the shape and strength of a liquid bridge between two spheres. *Journal of Colloid and Interface Science*, 113:544–556, 1986.

[180] Dongliang Tian, Yanlin Song, and Lei Jiang. Patterning of controllable surface wettability for printing techniques. *Chemical Society Reviews*, 42:5184–5209, 2013.

[181] Zhanlong Wang and Ya Pu Zhao. Wetting and electrowetting on corrugated substrates. *Physics of Fluids*, 29:067101–067111, 2017.

[182] Ville Liimatainen, Maja Vuckovac, Ville Jokinen, Veikko Sariola, Matti J. Hokkanen, Quan Zhou, and Robin H.A. Ras. Mapping microscale wetting variations on biological and synthetic water-repellent surfaces. *Nature Communications*, 8:1–7, 2017.

[183] Muhammad S. Sadullah, Gaby Launay, Jayne Parle, Rodrigo Ledesma-Aguilar, Yonas Gizaw, Glen McHale, Gary George Wells, and Halim

Kusumaatmaja. Bidirectional motion of droplets on gradient liquid infused surfaces. *Communications Physics*, 3:1–7, 2020.

[184] Steven Armstrong, Glen McHale, Rodrigo Ledesma-Aguilar, and Gary G. Wells. Pinning-Free Evaporation of Sessile Droplets of Water from Solid Surfaces. *Langmuir*, 35:2989–2996, 2019.

[185] Mantredo Do Carmo. Differential Geometry of Curves and Surfaces. *Dover publications (Second Edition)*, 1976.

[186] Thomas W. Bartel and Simone L. Yaniv. Creep and creep recovery response of load cells tested according to U.S. and international evaluation procedures. *Journal of Research of the National Institute of Standards and Technology*, 102(3):349–362, 1997.

[187] Olivier Pitois, Pascal Moucheront, and Xavier Chateau. Liquid bridge between two moving spheres: An experimental study of viscosity effects. *Journal of Colloid and Interface Science*, 231:26–31, 2000.

[188] Hien Nho Gia Nguyen, Olivier Millet, Chao Fa Zhao, and Gérard Gagneux. Theoretical and experimental study of capillary bridges between two parallel planes. *European Journal of Environmental and Civil Engineering*, 26, 2020.

[189] Peter S. Swain and Reinhard Lipowsky. Wetting between structured surfaces: Liquid bridges and induced forces. *Europhysics Letters*, 49:203–209, 2000.

[190] Dan Daniel, Chee Leng Lay, Anqi Sng, Coryl Jing Jun Lee, Darren Chi Jin Neo, Xing Yi Ling, and Nikodem Tomczak. Mapping micrometer-scale wetting properties of superhydrophobic surfaces. *Proceedings of the National Academy of Sciences*, 116:25008–25012, 2019.

[191] David L. Malotky and Manoj K. Chaudhury. Investigation of capillary forces using atomic force microscopy. *Langmuir*, 17:7823–7829, 2001.

[192] Victor Barcons, Albert Verdaguer, Josep Font, Matteo Chiesa, and Sergio Santos. Nanoscale capillary interactions in dynamic atomic force microscopy. *Journal of Physical Chemistry C*, 116:7757–7766, 2012.

[193] Shengfeng Cheng and Mark O. Robbins. Capillary adhesion at the nanometer scale. *Physical Review E - Statistical, Nonlinear, and Soft Matter Physics*, 89:1–16, 2014.

[194] Chao Zhang, Zhen Liu, and Yi Dong. Effects of adsorptive water on the rupture of nanoscale liquid bridges. *Applied Clay Science*, 146:487–494, 2017.

[195] Joost W. van Honschoten, Niels R. Tas, and Miko. Elwenspoek. The profile of a capillary liquid bridge between solid surfaces. *American Journal of Physics*, 78:277–286, 2010.

[196] Aurélie Lafuma and David Quéré. Slippery pre-suffused surfaces. *Europhysics Letters*, 96:1–4, 2011.

[197] Saurabh Nath. Thesis: Drops on liquid-infused solids (English). *Université Paris sciences et lettres*, 2021.

[198] Caitlin Howell, Alison Grinthal, Steffi Sunny, Michael Aizenberg, and Joanna Aizenberg. Designing Liquid-Infused Surfaces for Medical Applications: A Review. *Advanced Materials*, 30:1–26, 2018.

[199] Junsheng Li, Tanja Kleintschek, Annika Rieder, Yin Cheng, Tilo Baumbach, Ursula Obst, Thomas Schwartz, and Pavel A. Levkin. Hydrophobic liquid-infused porous polymer surfaces for antibacterial applications. *American Chemical Society: Applied Materials and Interfaces*, 5:6704–6711, 2013.

[200] Sarah J. Goodband, Halim Kusumaatmaja, and Kislon Voïtchovsky. Development of a setup to characterize capillary liquid bridges between liquid infused surfaces. *American Institute of Physics Advances*, 12:1–12, 2022.

[201] Koichi Takamura, Herbert Fischer, and Norman R. Morrow. Physical properties of aqueous glycerol solutions. *Journal of Petroleum Science and Engineering*, 98:50–60, 2012.

[202] Ahmet Alperen Günay, Soumyadip Sett, Qiaoyu Ge, Tie Jun Zhang, and Nenad Miljkovic. Cloaking dynamics on lubricant-infused surfaces. *Advanced Materials Interfaces*, 7:1–13, 2020.

[203] Prashant Bahadur, Ken G. Pepper, Kumud Chaurasia, Preeti S. Yadav, and Rafael Tadmor. Interfacial tension and spreading coefficient for thin films, and lateral drop adhesion. *American Institute of Chemical Engineers Annual Meeting, Conference Proceedings*, 1:3185–3190, 2008.

[204] Ciro Semprebon, Muhammad Subkhi Sadullah, Glen McHale, and Halim Kusumaatmaja. Apparent contact angle of drops on liquid infused surfaces: geometric interpretation. *Soft Matter*, 17:9553–9559, 2021.

[205] Kenneth Brakke. The Surface Evolver. *Susquehanna University*, 2010.

[206] Lisa Henke, Noemi Nagy, and Ulrich J. Krull. An AFM determination of the effects on surface roughness caused by cleaning of fused silica and glass substrates in the process of optical biosensor preparation. *Biosensors and Bioelectronics*, 17:547–555, 2002.

[207] Ran Zhang, Wei Liao, Yunpeng Wang, Yao Wang, D. Ian Wilson, Stuart M. Clarke, and Zhongqiang Yang. The growth and shrinkage of water droplets at the oil-solid interface. *Journal of Colloid and Interface Science*, 584:738–748, 2021.

[208] Zhen Li, Karam N. Al-Milaji, Hong Zhao, and Da Ren Chen. Ink bridge control in the electrohydrodynamic printing with a coaxial nozzle. *Journal of Manufacturing Processes*, 60:418–425, 2020.

[209] Xing Yi Ling, In Yee Phang, Julius G. Vancso, Jurriaan Huskens, and David N. Reinhoudt. Stable and transparent superhydrophobic nanoparticle films. *Langmuir*, 25:3260–3263, 2009.

[210] Federico Veronesi, Guia Guarini, Alessandro Corozzi, and Mariarosa Raimondo. Evaluation of the durability of slippery, liquid-infused porous surfaces in different aggressive environments: Influence of the chemical-physical properties of lubricants. *Coatings*, 11:1170–1183, 2021.

[211] Jonathan B. Boreyko, Georgios Polizos, Panos G. Datskos, Stephen A. Sarles, and Patrick C. Collier. Air-stable droplet interface bilayers on oil-infused

surfaces. *Proceedings of the National Academy of Sciences of the United States of America*, 111:7588–7593, 2014.

[212] Brian J. Lowry and Paul H. Steen. Stability of slender liquid bridges subjected to axial flows. *Journal of Fluid Mechanics*, 330:189–213, 1997.

[213] Wei Chen, Alexander Y. Fadeev, Meng Che Hsieh, Didem Öner, Jeffrey Youngblood, and Thomas J. McCarthy. Ultrahydrophobic and ultralyophobic surfaces: some comments and examples. *Langmuir*, 15:3395–3399, 1999.

[214] Shasha Qiao, Shen Li, Qunyang Li, Bo Li, Kesong Liu, and Xi Qiao Feng. Friction of droplets sliding on microstructured superhydrophobic surfaces. *Langmuir*, 33:13480–13489, 2017.

[215] Lakshminarayanan Mahadevan and Yves Pomeau. Rolling droplets. *Physics of Fluids*, 11:2449–2453, 1999.